



TU Clausthal

**Deformation behaviour of a concrete gravity dam  
based on monitoring data and numerical simulation**

**Doctoral Thesis  
(Dissertation)**

to be awarded the degree  
Doctor of Engineering (Dr.-Ing.)

submitted by  
M. Sc. Yuan Li  
from Shanxi, China

approved by the Faculty of Energy and Economic Sciences  
Clausthal University of Technology

Date of oral Examination  
10 December 2020

Dean  
Prof. Dr. Bernd Lehmann

Chairperson of the Board of Examiners  
Prof. Dr. Hans-Jürgen Gursky

Supervising tutor  
Prof. Dr.-Ing. Norbert Meyer

Reviewer  
Prof. Dr. Roland Strauß

## Acknowledgements

It has been a great privilege for me to spend several years working in the Institute of Geotechnical Engineering and Mine Surveying at Clausthal University of Technology.

Foremost, I would like to express my sincere thanks to Univ.-Prof. Dr.-Ing. Norbert Meyer, my supervisor, for his encouragement and instructive guidance for the development of my dissertation. Especially I would like to express my profound gratitude to Dr.-Ing. Ansgar Emersleben for his support and numerous constructive advices.

My further thanks go to all colleagues in Institute of Geotechnical Engineering and Mine Surveying for providing me a pleasant working environment. Especially I would like to thank Dipl.-Ing. Daniel Gröger and Dr.-Ing. Chuantao Chen for the support and lots of technical discussions. Also, I am indebted to the team of Dam management in Sachsen-Anhalt for providing the necessary monitoring data.

I would like to extend my gratitude to the China Scholarship Council (CSC) and Department of Geotechnical Engineering at Clausthal University of Technology for the financial supporting for my stay in Germany.

I express my deep grateful to my parents for their understanding and heartfelt support during these years.

Clausthal-Zellerfeld, September 2020

Yuan Li



## Abstract

Deformation behaviour is a key index for evaluating the health state of concrete dam structures in long-term service. Under regular loading conditions, dam's deformation behaviour can be preliminary depicted using monitoring data. Physically well-founded numerical simulation of the dam's deformation behaviour provides an efficient approach to comprehend the effects of different external loads. In this work, an advanced numerical model based on monitoring data and thermal-structural coupled analysis is developed for a concrete gravity dam, the Rappbode Dam, to gain insight into the current deformation behaviour of the dam under usual and unusual load conditions.

Firstly, a graphical visualisation of the monitoring data, including air temperature, water temperature, water level in the reservoir, uplift water pressure at the dam base, temperature interior the dam body and horizontal displacements, is presented to illustrate ambient loading conditions and structural responses of deformation behaviour. Secondly, based on mesh accuracy analysis which considers the different element types and mesh densities, a functional finite element model of the dam-foundation system is generated with appropriate mesh, enabling the thermal analysis of time-varying temperature distributions and structural analysis of deformation behaviour. Thirdly, based on the thermal analysis, a transient heat transfer model is calibrated to describe the thermal transfer process from the ambient environment to the dam and to present the time-varying temperature distribution within the dam body. The initial condition in the transient thermal analysis is investigated to acquire a rational primary temperature distribution in the dam. The thermal properties of the dam's concrete are back analysed based on the concrete temperature from thermometers. The time-dependent air temperature and water temperatures are considered to specify boundary conditions. Lastly, in structural analysis, by investigating the displacement response under the loads of temperature distribution within the dam body, the hydrostatic pressure, uplift pressure and self-weight, mechanical material parameters are back analysed based on the measurements. Hence, material parameters of the dam's concrete are updated to the present operational phase, therewith an advanced numerical model of the dam is developed. In terms of recorded usual loading conditions, computed results are aligned with measured results of displacements.

With the aid of the advanced numerical model of the dam, the thermal effect due to time-varying temperature distribution, structural effect due to water-level variation and simultaneous effect are investigated under usual and unusual loading conditions. The results show that thermal displacements at different points are in phase with each other despite the phase shift in temperatures from each other. Hydrostatic pressure is more significant than uplift water pressure in determining the structural displacement. The thermal effect dominates the

displacement at the dam crown, while the effect due to water level begins to dominate with the decrease of elevation. The results from an example of an unusual load case indicate enlarged ranges of displacement variations and warn of areas with possible cracks in the dam.

## Kurzfassung

Das Verformungsverhalten ist ein Schlüsselindex bei der Bewertung des Zustands einer Staumauer im Langzeiteinsatz. Unter regelmäßigen Belastungsbedingungen kann es anhand von Überwachungsdaten dargestellt werden. Physikalisch fundierte numerische Simulationen des Verformungsverhaltens der Staumauer bieten einen effizienten Ansatz, um die Auswirkungen verschiedener externer Belastungen zu erfassen. In dieser Arbeit wird ein fortschrittliches numerisches Modell auf der Grundlage von Überwachungsdaten und thermisch-strukturell gekoppelten Analysen für eine Staumauer, die Rappbodetalsperre, entwickelt, um einen Einblick in das aktuelle Verformungsverhalten der Staumauer unter regulären und ungewöhnlichen Lasteinwirkungen zu gewinnen.

Zunächst werden Überwachungsdaten wie die Lufttemperatur, die Wassertemperatur, der Wasserspiegel im Speicher, der Sohlwasserdruck, die Betontemperatur innerhalb der Staumauer und die horizontalen Verschiebungen grafisch dargestellt, um die Eigenschaften der externen Lasteinwirkungen sowie die strukturellen Reaktionen des Verformungsverhaltens zu veranschaulichen. Anschließend werden geeignete Netze für das funktionale Finite-Elemente-Modell der Rappbodetalsperre erzeugt, dessen Genauigkeit durch die Untersuchung verschiedener Elementtypen und Netzfeinheiten gewährleistet wird. Das funktionale Finite-Elemente-Modell ermöglicht eine transiente thermische und eine strukturelle Analyse. Die transiente thermische Analyse der Temperatur erlaubt es, die Randbedingungen als variierende Umgebungstemperatur mit der Zeit zu spezifizieren und die Temperaturverteilung innerhalb der Staumauer für jeden Zeitpunkt zu berechnen. Die Spezifizierung der Anfangsbedingungen in der transienten thermischen Analyse wird untersucht, um eine rationale primäre Temperaturverteilung in der Staumauer zu erhalten. Abschließend werden die Eigenschaften des Staumauerbetons anhand der Beton-Temperaturmessungen innerhalb der Staumauer und Verschiebungen analysiert, indem das Verschiebungsverhalten unter den Belastungen der Temperaturverteilung innerhalb des Staukörpers, des hydrostatischen Drucks, des Auftriebsdrucks und des Eigengewichts untersucht wird. Dementsprechend wird ein fortschrittliches numerisches Modell der Staumauer entwickelt, deren Materialparameter des Staumauerbetons auf die gegenwärtige Betriebsphase aktualisiert und angepasst sind. Im Hinblick auf die üblichen Belastungsbedingungen werden gute Übereinstimmungen zwischen den berechneten und gemessenen Ergebnissen der Verschiebungen nachgewiesen.

Mittels des fortgeschrittenen numerischen Modells der Staumauer werden die thermische, die strukturelle und die gesamte Verschiebung unter gewöhnlichen und ungewöhnlichen Belastungsbedingungen untersucht. Durch die Ergebnisse wird deutlich, dass trotz der

Phasenverschiebung der Temperaturen voneinander die thermischen Verschiebungen an verschiedenen Stellen in der Staumauer in Phase zueinander liegen. Der hydrostatische Druck ist für die Bestimmung der strukturellen Verschiebung von größerer Bedeutung als der Sohlwasserdruck. Der thermische Effekt dominiert die Verschiebung an der Staumauerkrone, und mit der Abnahme der Höhe beginnt der Effekt des Wasserspiegels zu dominieren. Die Ergebnisse eines Beispiels für einen ungewöhnlichen Belastungszustand weisen auf erweiterte Verschiebungen hin und warnen vor möglichen Rissen in der Mauerkörper.



## Contents

<b>1. Introduction .....</b>	<b>1</b>
1.1 Aim of the thesis.....	2
1.2 Structure of the thesis .....	3
<b>2. State of the art.....</b>	<b>5</b>
2.1 Classification of dams .....	5
2.2 Health monitoring of concrete dams .....	8
2.3 Numerical modelling of dams .....	10
2.3.1 Theoretical and planar modelling .....	10
2.3.2 Spatial and three-dimensional modelling.....	12
2.3.3 Numerical modelling with parameters calibration.....	13
<b>3. Monitoring of deformation behaviour of Rappbode Dam.....</b>	<b>16</b>
3.1 General information of the investigated dam .....	16
3.2 Monitoring in the investigated dam .....	19
3.2.1 Monitoring of horizontal deformations of the Rappbode Dam .....	19
3.2.2 Monitoring of concrete temperature of the Rappbode Dam .....	21
3.2.3 Monitoring of uplift pressure at base of the Rappbode dam.....	22
3.3 Analysis of recorded ambient conditions at the site .....	22
3.3.1 Water level in the reservoir.....	22
3.3.2 Uplift pressure at the base of the dam.....	23
3.3.3 Ambient temperature at dam crown.....	27
3.3.4 Ambient temperature at water side of the dam .....	27
3.4 Analysis of measured responses of the dam .....	30
3.4.1 Temperature within the dam body .....	31
3.4.2 Horizontal displacement in upstream-downstream direction.....	34
3.4.3 Horizontal displacement in longitudinal direction .....	39
3.5 Conclusions .....	42

---

<b>4. Functional FE model of Rappbode Dam .....</b>	<b>44</b>
4.1 Thermal analysis and structural analysis in FE modelling.....	44
4.1.1 Basis of thermal /structural analysis in ANSYS.....	44
4.1.2 Specification of external loads in deformation analysis.....	45
4.1.3 Transient thermal analysis .....	47
4.2 Geometry model and material behaviours of dam-foundation system .....	50
4.2.1 Geometry model.....	50
4.2.2 Material behaviour.....	51
4.3 Accuracy analysis of mesh elements for the dam body .....	53
4.3.1 Comparison of two different element types.....	53
4.3.2 Analysis of mesh density under the hydrostatic pressure .....	55
4.3.3 Analysis of mesh density under thermal load .....	57
4.3.4 FE model of Rappbode Dam with appropriate mesh .....	60
<b>5. Back analyses of the material parameters of Rappbode Dam .....</b>	<b>62</b>
5.1 Determination of initial temperature distribution.....	62
5.1.1 Influence of different initial uniform temperatures specified .....	63
5.1.2 Specification of appropriate initial temperature field .....	67
5.2 Calibration of transient heat transfer model .....	68
5.2.1 Back analysis of effective thermal conductivity .....	68
5.2.2 Adjustment of the boundary temperature conditions.....	71
5.3 Back analysis of parameters in structural analysis .....	74
5.3.1 Back analysis of effective coefficient of thermal expansion .....	75
5.3.2 Back analysis of effective elastic modulus for dam body .....	76
5.4 Conclusions .....	79
<b>6. Deformation behaviour based on numerical simulation .....</b>	<b>80</b>
6.1 Thermal displacements under time-varying temperature distribution .....	80
6.1.1 Thermal response under usual temperature situations .....	80
6.1.2 Simulation of unusual temperature situations .....	88

---

6.2	Structural displacements due to water level variation .....	94
6.2.1	Response under usual water level variations .....	94
6.2.2	Response under unusual water level variations.....	97
6.3	Simultaneous displacements due to water level and temperature variation .....	98
6.3.1	Simultaneous displacements based on ANM .....	98
6.3.2	Relationship between structural/thermal and simultaneous displacements....	106
6.3.3	An example of unusual load case.....	109
6.4	Conclusions .....	113
<b>7.</b>	<b>Conclusions and recommendations .....</b>	<b>115</b>
7.1	Conclusions .....	115
7.2	Recommendations .....	116
<b>8.</b>	<b>Literature .....</b>	<b>118</b>
<b>A.</b>	<b>Additional ambient temperature at water side from monitoring data.....</b>	<b>125</b>
<b>B.</b>	<b>Approximation of air-concrete contact surface .....</b>	<b>126</b>
<b>C.</b>	<b>Definition of elevation of the water temperature layers.....</b>	<b>129</b>
<b>D.</b>	<b>Information about the locations in mesh density analysis .....</b>	<b>130</b>
<b>E.</b>	<b>Information about elevations and blocks .....</b>	<b>131</b>
<b>F.</b>	<b>Tensile strength of concrete material for Rappbode Dam .....</b>	<b>132</b>
<b>G.</b>	<b>Additional information about comparisons between computed and measured displacements.....</b>	<b>134</b>
	<b>List of abbreviations and symbols.....</b>	<b>137</b>
	<b>List of Figures.....</b>	<b>140</b>
	<b>List of Tables .....</b>	<b>144</b>



## 1. Introduction

More than 58,000 dams in 96 countries worldwide provide different benefits for the surrounding area (ICOLD, 2019), such as supplying water for irrigation or drinking, generating hydroelectricity and providing flood control. However, dams face certain risks, and in the worst case of dam failure, rapid and uncontrolled water flow could cause flash flood, mud-rock flow etc., resulting in fatalities and economic losses (Luino et al., 2012; Stansell, 2014). Appropriate surveillance on dams should be conducted to detect abnormal performance as early as possible and minimise disaster.

Health monitoring belongs to a topic of great importance in dam surveillance. Data acquired from the monitoring system can be analysed and interpreted to evaluate dam performance based on expected behaviour to determine whether maintenance is necessary. Deformation behaviour of a dam is commonly used to depict the health status of a dam and refers to the displacement distribution, namely displacement at different locations, as well as these displacements' variation over time.

The need for effective analysis and interpretation of relationship between the external loads and deformation responses was emphasized in the general Report of International Commission on Large Dams (ICOLD) (Dibiagio, 2000). Designed to withstand loads by its own weight, a concrete gravity dam is usually a massive concrete structure whose surface is exposed to air or water with time-varying temperatures. The massive concrete and time-varying ambient temperature result in a complicated thermal distribution response within the dam body, which is the key factor to determining thermal displacements. The water in the reservoir causes hydrostatic pressure at the upstream face, while seepage causes uplift pressure at the wide dam base of a concrete gravity dam, which are the two factors in terms of structural displacements due to water level. Besides, the dam configuration is often complex, and the underlying bedrock influences the deformation behaviour. It is thus worthwhile to investigate the deformation behaviour of a concrete gravity dam under the variation of ambient temperature and water level.

Monitoring data of displacement measurements obtained from the monitoring system of a concrete gravity dam can preliminarily depict the dam deformation behaviour under regular loading conditions. To sufficiently evaluate the dam deformation responses under known loading and thermal conditions, numerical models are recommended to analyse transient thermal phenomena and the complex deformation behaviour of concrete gravity dams (Graham, 1999; Rich, 2014). A numerical model of a dam can be established theoretically already at the design phase of a structure to predict its thermal and structural behaviour (Lombardi, 2004). However, a dam's performance or material properties may decrease over

time due to, for example, age-related deterioration, the seepage dissolution process, saltwater intrusion, the UV rays and so on. To overcome this problem, the numerical model can be refined and modified after some years by calibrating parameters in the thermal process and deformation variations based on the monitoring data. This results in an advanced numerical model (ANM) to interpret the dam's current behaviour.

## 1.1 Aim of the thesis

Based on monitoring data and numerical simulation, the aim of this work is to interpret the deformation behaviour of a concrete gravity dam, the Rappbode Dam, in operational phase under ambient environmental conditions. External loads, including hydrostatic pressure, uplift pressure and ambient temperature, should be considered to determine the deformation behaviour, and transient thermal analysis should be conducted to investigate the time-dependent temperature distribution in the dam body. The material properties of this concrete gravity dam should be back analysed based on the monitoring data in transient thermal analysis and structural analysis. Hence, the concrete gravity dam's deformation behaviour and health state can be depicted under combination of above-mentioned external loads in usual and unusual load cases.

This research entails the following tasks:

- *Structural deformation simulation* — to investigate the dam's structural displacements' distribution due to hydrostatic pressure at the upstream face and uplift pressure at the dam base; and to analyse the effect of the underlying bedrock and valley at lateral on the structural displacement.
- *Thermal deformation simulation* — to simulate the time-varying thermal distribution within the dam body while considering boundary ambient temperature conditions, including time-varying air, water and ground temperature; and to investigate the thermal displacement distribution and time-varying thermal displacement in the dam structure.
- *Monitoring data analysis* — to understand the seasonal deformation behaviour of the dam, the concrete temperature response in the dam at several elevations across the section's thickness; and to obtain the characteristics of seasonal variability of the air temperature, water temperature, uplift pressure and water level at the Rappbode Dam.
- *Development of an ANM* — to generate a functional finite element (FE) model of the dam foundation system, enabling the simulation of the transient thermal process and structural analysis of the deformation; and to back analyse the material parameters based on the monitoring data, in the thermal-structural coupled analysis.

- *Deformation analysis based on the ANM*— to comprehend the deformation behaviour for combinations of water levels and ambient temperatures under usual and unusual loading conditions; to determine which load plays a greater role in displacement distribution; and to present an evaluation of the dam's health state.

## 1.2 Structure of the thesis

The thesis is subdivided into seven chapters:

Chapter 1 presents an overview of the topic, aim and structure of this work.

Chapter 2 presents a literature review, which summarises the interpretation methods for analysing the monitoring data and describes the classification and health monitoring of dams. To present research in this area, numerical simulations utilised on different concrete dams to simulate the displacement and thermal distributions as well as stresses are summarised.

Chapter 3 introduces the Rappbode Dam and its monitoring system. This chapter focuses on analysing the monitoring data and understanding the time-varying deformation behaviour, displacement distribution, time-varying concrete temperature, temperature distribution in the transverse section of this massive concrete dam, time-varying ambient air temperature, time-varying water temperature in different layers, time-varying water level and uplift pressure.

Chapters 4 and 5 describe the development of an ANM to simulate the time-dependent temperature distribution and deformation behaviour of the Rappbode Dam. Chapter 4 explains thermal and structural analysis in ANSYS and the creation of a functional, three-dimensional FE model of the dam foundation system. The FE model's mesh generation is investigated based on different element types and sizes to satisfy the accuracy of the computation in both thermal and structural analysis. The functional FE model enables simulating transient thermal phenomena, including thermal and structural displacement. To determine the current dam performance, Chapter 5 presents the calibration of the heat transfer and structural deformation models, where material properties, such as thermal conductivity, the coefficient of thermal expansion and elastic modulus, are back analysed based on the monitoring data in the thermal-structural coupled analysis. This enables creating the ANM of the dam.

Chapter 6 presents the ANM-based investigation of the dam deformation. Structural deformation due to variations in water level and thermal deformation, including thermal displacement distribution and time-varying thermal displacement are computed under recorded usual loading conditions and also unexperienced unusual loading conditions. In investigating the simultaneous displacement distribution, the ANM is verified by comparing the computed and measured displacements' distribution in the dam under usual loading conditions. The relationships between single structural displacement or single thermal

displacement and simultaneous displacement are investigated to determine the decisive factor of the dam deformation behaviour. In unusual loading condition example, displacement responses and stresses are investigated, and the health state of the dam is predicted while considering the combination of unusual variations in water level and ambient temperature.

Chapter 7 summarises the work presented in the previous chapters. Conclusions are drawn, achievements and outcomes are summarised and an outlook for future research is provided.



## 2. State of the art

This chapter firstly introduces dam types, classification and main characteristics and then focuses on concrete dams. Secondly, the health monitoring system's items and data acquisition approaches are summarised and the interpreting methods for the acquired data are compared. Thirdly, to comprehend this area's modelling techniques, research regarding numerical modelling to simulate the response of displacements, thermal distributions and stresses due to external loads in different concrete dams are described and summarised.

### 2.1 Classification of dams

A dam is a structure serving to reserve flowing water or underground streams, and it can also provide human uses (DIN 19700-11, 2004). The structures are basically divided into masonry dams (mostly old structures) or concrete, reinforced concrete dams and embankment dams consisting of earth or rock (Rißler, 1998). Dams simultaneously perform load-bearing and sealing functions, and embankment dams usually require a specially arranged sealing zone, with most having an impermeable material core or upstream face to prevent seepage water through the dam (Murty, 2015).

The Rappbode Dam is a concrete gravity dam equipped with an advanced monitoring system, and the dam's structural and environmental characteristics are detailed in Chapter 3. The construction of concrete dams in Germany began in 1922 with the Schwarzenbach Dam. Germany currently has 75 gravity dams, 34 of which are concrete and mostly found in the Harz Mountains, Thuringian Forest, Black Forest and the Bohemian Forest (Rißler, 1998).

Concrete dam classification varies regarding different criteria. For example, Figure 2.1 shows that dams are divided into two classes regarding geometric size (DIN 19700-11, 2004), where class 1 comprises large dams and class 2 comprises medium-sized and small dams. Large dam criteria require the dam height from the lowest foundation point to the crown to be greater than 15 m or a total reservoir storage capacity exceeding 1,000,000 m<sup>3</sup>. Dams that fail to satisfy the requirements for class 1 are classified to class 2. However, depending on their overall importance and hazard potential, dams can be assigned to dam class 1 or 2 independently of the above specifications.

Regarding their structural shape, concrete dams can be categorised into three types: gravity dams, arch dams and buttress dams (Rißler, 1998). A gravity dam holds the water in the reservoir with its own gravity, has a cross-section that is usually triangular with an extension in the crown area and it can be built on sites with wide or narrow valleys with sound bedrock (Rißler, 1998). Due to the massive concrete required, gravity concrete dams are expensive yet

versatile and possess substantial overflow capacity (Golze, 1977). Buttress dams use less material than gravity dams due to the clear spaces between the buttresses, and they are similarly suited to both narrow and wide valleys. Arch dams however are thinner, suitable for narrow valleys with steep sides and require stable rock for their foundations to resist the arch forces. Some examples of large concrete dams with different shapes are shown in Figure 2.2, including the Hoover Dam, Roselend Dam and Three Gorges Dam.

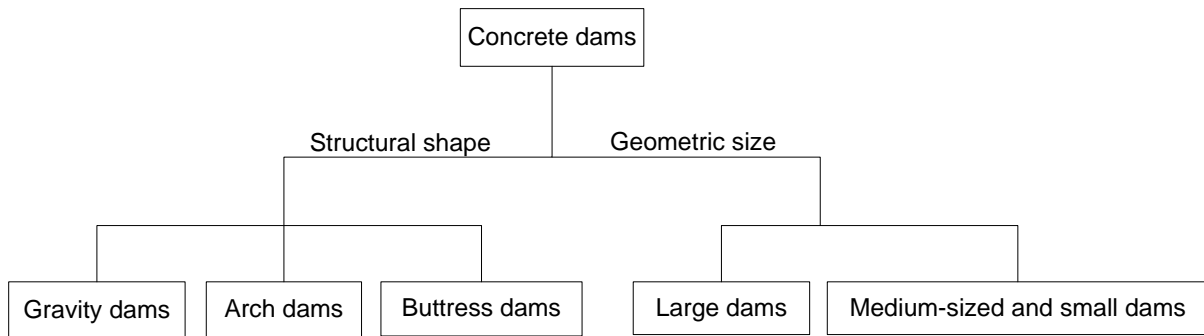


Figure 2.1: Diagram of the classification of dams

The Hoover Dam is a concrete arch-gravity dam which represents a compromise between the arch and gravity dams that combines their strengths. It was built in the Black Canyon of the Colorado River and impounds to Lake Mead with a height of 221.4 m, a longitudinal length of 379 m, a width of 200 m at the bottom and 14 m at the top (Stevens, 1988). With a total capacity of 35.2 km<sup>3</sup>, the Lake Mead is the largest reservoir in the United States by volume (Holdren et al., 1998). The Roselend Dam is a buttress arch dam, shown in Figure 2.2 (b), located 5 km east of Beaufort in south-eastern France with a maximum height of 150 m and longitudinal length of 804 m (Roselend-Staudamm, 2007). Figure 2.2 (c) shows the Three Gorges Dam, which is a concrete gravity dam with a longitudinal length of 2,335 m, maximum height of 175 m and total storage capacity of 39.3 km<sup>3</sup> (Huang & Wu, 2018). Stretching cross the Yangtze River between Hubei and Chongqing in China, the dam serves as a large power station with a 22,500 MW capacity since 2012 (Cleveland & Morris, 2014).

The self-weight of a gravity dam and width of its base prevent it from being overturned due to the load of impound water in the reservoir (Kennard et al., 1995). Hence, the gravity dam has the greatest volume of concrete among these different types. A concrete gravity dam normally regards plain concrete material with little steel at the exposed face area, making it vulnerable to tensile stresses. The large section size of the concrete structure and its frequent exposure to air or water complicate the dam's temperature distribution due to the ambient temperature changes and hydration heat of the concrete. Targeted research is needed to comprehend the displacement distribution aroused from the temperature distribution, together with the hydrostatic pressure at upstream and the uplift pressure at the wide base of these concrete structures.



(a): Hoover Dam in U.S.A (Photo by Steve Hanley,2018)



(b): Roselend Dam in France (Photo by Adrien Mortini, 2008)



(c): Three Gorges Dam in China (Photo by Xinhua Reporter, 2005)

Figure 2.2: Examples of dams of different types

## 2.2 Health monitoring of concrete dams

Health monitoring is effective in ensuring long-term safety and is important for concrete dams in high service years. Monitoring data from dams' health monitoring systems provide information about dams' time-varying ambient environmental conditions and the responses of temperature distribution, displacement etc.

Monitoring data from the monitoring system can be manually or automatedly obtained (Hoppe et al., 2015), with the former representing the traditional data collection method at most dams. An automated monitoring system can reduce manpower for data reading which occurs remotely in real time and avoids faulty readings due to human error. However, personnel spend less time at the dam resulting in a lack of regular visual observations, and automated systems also entail higher costs for initial implementation and maintenance by socialised staff (ICOLD, 2003). Performing cross checks of both automated and manual readings allows calibrating the measurement instruments.

The health monitoring of concrete dams can be divided into static and dynamic monitoring (Bukenya et al., 2014). The static behaviour of dams can be monitored by sensors and instruments with high accuracy to measure air temperature, water temperature, ground temperature, reservoir water level, uplift pressures, horizontal displacements, vertical displacements, the opening and closing of joints and cracks as well as stresses, strains and so on (Bukenya et al., 2014; Bianchi & Bremmen, 2014). Dynamic monitoring, regards structural responses in a brief time range, usually in the form of accelerations or velocities due to vibrations, and then modal properties, including natural frequencies, damping ratios and mode shapes, can be extracted from accelerations through modal analysis (Zhang et al., 2004; Cantieni et al., 1998)

The dynamic behaviour of dams can be obtained by using forced vibration or ambient vibration tests. Ambient vibration tests obtain the vibrations due to environmental forces such as wind, water waves and ground motions, while dams are excited by controlled force in forced vibration tests (Buffi et al., 2017; Daniell et al., 1999). Dynamic monitoring is not always suitable for strong structures with little vibration, where it is expensive to conduct experiments and difficult to analyse monitoring data (Brincker et al., 2007; Bukenya et al., 2012). In such cases, more accurate deformation results can be obtained via static monitoring. Therefore, dynamic monitoring research exceeds the scope of this thesis and is not reviewed.

Static monitoring measurements involve structural responses (e.g., temperature in the dam, displacements, stresses, strains etc.) and ambient environmental conditions (air temperature, water temperature, water level) are captured in the time range (De Sortis et al., 2007; Perner & Oberhuber, 2010). The data collected from different instruments are important in the health

monitoring of concrete dams and require analysis and management to interpret the dam behaviour. The analysis of monitoring data can be depicted using behaviour models to create functional relationships between ambient environmental conditions (cause) and structural responses (effect). Ambient environmental condition variables primarily include hydrostatic pressure and thermal variations (ICOLD, 2003), whose responses include displacement, temperatures in the dam, effective stress etc. Behaviour models can be classified as statistical, deterministic or hybrid based on their approaches to analysing the dam responses (Lombardi, 2004; Bukenya et al., 2014). The traditional statistical model uses measurements to present the pure mathematical correlations between the given response and ambient conditions based on the previous measurements (Nedushan, 2002). In contrast, the deterministic model considers the structural characteristics and physical parameters to compute the response based on structural analyses, which enables predicting behaviour under loading conditions that has not experienced yet (Lombardi, 1999). Hybrid models represent a mix of the above and are appropriate for situations where some cause data exists to obtain effect component whereas some other cause data does not exist, then requires a statistical estimation of corresponding effect (ICOLD, 2003; Lombardi, 1999).

Statistical models use regression analysis to establish mathematical relationships between observed effects and corresponding causes (Beaujoint, 1967). For example, if the recorded effect is structural deformations, then the causes are external loads. The current dam behaviour determined using the statistical model is compared with the measured values of the structure's previous years (Wang, 2010). The statistical model's accuracy depends on the quantity and reliability of the available recorded data (Bossoney, 1994).

Statistical models are widely used since they are simple to formulate and implement. Significant research and different techniques are utilised in statistical analysis, including hydrostatic season time model (Chouinard, Larivière, Côté & Zhao, 2006), multiple linear regression (Nedushan, 2002), singular spectrum analysis with auto regressive model (Loh et al., 2011), multiple layer perceptron model (Demirkaya & Balcilar, 2012), neural network (Mata et al., 2013) etc., which advance the statistical model interpretation of dam monitoring data.

However, the structural characteristics and physical material parameters of the dam are not considered in statistical models, which prevents explaining the dam mechanical operational behaviour. In addition, when measurement data lack the response from ultimate loads of water level and temperature or lack sufficient time-series length, statistic models established from these data would poorly reflect the actual dam behaviour. It is also not possible to verify the single effect of a cause from the regression function, and finally, due to the space and time limitations of monitoring data and the influence of random factors, the statistical model is not

ideal for epitaxial forecasting and does not provide a reliable approach to extrapolate the results for loading conditions not yet experienced by the dam.

A deterministic model relies on the logical and physical formalisation of the law that the dam is considered to obey. This procedure requires measurements concerning water level in the reservoir and temperature (ICOLD, 2003). A deterministic model presents the structure as solid, known geometrical shape possessing well-known physical properties and subjected to external loads. A simplified theoretical model can provide solutions for some structures with simple geometry, while this is not always possible or results in inaccuracy for most complex structures. The numerical finite element method (FEM) enables relating the responses of the dam with ambient environmental causes.

Hence, in order to achieve a sufficiently reliable evaluation of the dam status under known loading and thermal conditions, deterministic models are recommended. Unlike statistical evaluation procedures, deterministic models enable the physically well-founded analyses of transient thermal phenomena and complex deformation response of a concrete dam under combinations of external loads.

## 2.3 Numerical modelling of dams

Since geographic conditions, ambient conditions and material properties for each dam are different, dam deformation behaviour varies regarding the influence of external loads, including hydrostatic pressure, temperature, self-weight, uplift water pressure, silt etc. This section describes the numerical modelling of thermal and structural responses for different dams. Numerical simulation is used for the temperature and hydrostatic pressure simulation in concrete dams to determine the responses of time-varying temperature distribution and displacement distribution. Served as a behaviour model to analyse the monitoring data, the predicted responses of displacement or temperature from the numerical model are compared with the monitoring data. In the absence of monitoring data, a numerical model for a dam structure can serve as a benchmark model to indicate the response of the dam and to evaluate the other interpretation models. The modelling is conducted based on two-dimension planar or three-dimension special models, with or without calibrations based on the monitored measurements. Some of their applications are reviewed in the following section.

### 2.3.1 Theoretical and planar modelling

Boberg and Holm (2012) analysed a concrete gravity dam, Baozhusi Dam, which reopened after becoming upgraded via FE modelling. Their analysis was to evaluate the safety of the dam according to standards adopted in China by providing results through the planar FE modelling of a critical section of Baozhusi Dam. Both the operating and unusual load cases

were modelled and investigating the tension in the dam heel showed that in a static state, the dam is capable of withstanding its applied loads. Regarding the high stress values from the model, the author meant that it is not necessary to be alarmed even though high stresses were observed, because the stress concentrations occurred in small areas and only result in localised tension cracks.

Bettzieche (1998) utilised measuring data to calibrate an FE model, whereby the material constants taken from the literature were used as starting values and changed until an acceptable result was obtained. The related material parameters in the flow and heat transfer FE models were thereby calibrated. The FE flow model mapped the seepage and determined the water pressure forces in the interior of the dam wall, while the FE heat flow model quantified the seasonal temperature influence and resulting structural stresses.

By conducting a transient thermal analysis and stresses analysis based on FEM, Léger et al. (1993a & 1993b) developed a methodology to obtain the temperature and stress distributions in typical concrete gravity dams located in northern Canada. They analysed variations of environmental conditions including air, reservoir and foundation temperatures as well as solar radiation from the sun. Based on planar FE models and parameter studies they investigated the influence of (i) geometrical, thermal and mechanical properties, (ii) air temperature and reservoir and temperature variations as well as solar radiation on the structural response of displacement and stress. Some main conclusions were as follows: (i) in order to obtain a convergence of cyclical temperature inside the dam rapidly under the boundary condition of repeated seasonal temperature variation in thermal analysis, the initial temperature must be specified close to the mean temperature through the whole dam in a one-year period; (ii) the height of the dam affects the stiffness and structural response; (iii) the maximum crown displacement occurs at the time point with the lowest mean temperature of the upper third section of the dam.

Tatin et al. (2015) developed a physical-static model called Hydrostatic Season Time Grad (HST-Grad) to assess a concrete dam's deformation behaviour due to temperature variation in comparison with HST (Hydrostatic, Season, Time) and HSTT (Thermal HST) models. As a heuristic case, a planar FE model based on plane-stress assumption was generated to validate the proposed HST-Grad model. In this model, in absence of temperature values at the investigated dam site, the air temperature was modelled by interpolating values from several meteorology stations in surrounding regions, while the water temperature was determined using a theoretical model. Three simulations were conducted with different boundary load combinations: the first applies the air temperature for all exposed surface; the second applies air temperature at the air-exposed surface and water temperature in the normal water-level height; while the third considers not only the air and water temperatures but also water

temperature variation according to the retention lake's varied water level. The displacement values gained from these simulations were used as benchmarks to assess the above-mentioned HST, HSTT and HST-Grad models.

### 2.3.2 Spatial and three-dimensional modelling

In the FE analyses of Three Gorges Dam (Liu et al., 2003a & 2003b), numerical modelling was conducted along with stability analysis for the single most critical powerhouse-dam section. Then, displacements were simulated via three-dimension numerical modelling regarding the left- and right-side adjacent powerhouse-dam sections to investigate constraint influence. The results showed that the horizontal and vertical displacements at the dam heel, toe and top from the planar model are larger than those from the three-dimension model. These difference results from the difference in boundary conditions: the planar model was based on the assumption of plane strain and the constraint conditions at the sides of this critical section were unset; regarding the three-dimension modelling, the constraint effects were considered by extending the model with the left and right sides' adjacent sections, which contribute to the relative smaller deformations compared to the values derived from planar modelling.

De Sortis et al. (2007) compared a pure statistical method with a structural identification technique for interpreting the displacement response of buttress dams in Italy. For the structural identification technique, physical parameters were estimated based on FE models of one section of the dam structure, for which the linear elastic material was adopted, and the elastic modulus was assumed as a uniform value throughout the whole structure to acquire the structural responses. The results showed that both procedures could lead to comparable errors regarding crown displacements in the upstream-downstream direction, however the results from the FE model-based structural identification procedure deliver better accuracy for determining the deformation behaviour of the buttress dam.

Li et al. (2015) computed and evaluated the seepage and stress fields of a roller-compacted concrete (RCC) dam under construction based on FE models with four design schemes of upstream impervious layers. Comparing the results of stresses and water head distribution for two dam sections, a discharge section and a retaining discharge section showed that the stress control criteria could be satisfied under all four schemes. The maximum compressive stress could be detected for the zone near the dam toe, while the maximum tensile stress was observed for the zone around the dam heel.

Maken et al. (2013) presented FE modelling procedures to determine the thermo-mechanical behaviour of a concrete dam. Thermo-mechanical analysis was conducted on a benchmark beam model to investigate the influence of temperature-dependent material parameters. Different material models included (1) different values of linear elastic moduli of concrete for



different zones, (2) uniform elastic modulus of concrete considering nonlinear behaviour, and (3) uniform elastic modulus of concrete considering nonlinear behaviour and steel reinforcement on the half downstream. The results showed that results from the three different material assumptions do not significantly affect the structural response.

Sheibany et al. (2006) conducted three-dimensional FE modelling to present the thermal stresses of a concrete arch dam in Iran. In their thermal analysis, the air temperature, water temperature in the reservoir as well as solar radiation were specified as boundary conditions, and the convergent rate of temperature at different locations in the dam was characterised. The results showed that the temperatures determined using the FE model are aligned with the monitoring records at Karaj Dam and that the water temperature plays a significant role in determining the annual temperature distribution due to the relative thinness of the arch dam in the transverse section. The mechanical analysis examined the thermal stresses at every midmonth in one typical year period, and it was observed that probable cracks developed in the downstream surface in a narrow region which experiences the highest temperature. July and August represent the most critical period in one-year cycle for Karaj Dam concerning the magnitude of tensile stresses, because the stronger solar radiation results in higher temperatures in the downstream surface and most excessive temperature gradient in the transverse section.

### 2.3.3 Numerical modelling with parameters calibration

Zhou et al. (2011) analysed the time series of settlement or vertical displacement of a concrete-face rockfill dam (CFRD) via data monitoring and numerical simulation. The dam investigated in this work is newly constructed, and the monitoring data cover the operational as well as construction and initial impounding periods. The vertical displacement was firstly investigated, and the behaviour was characterised based on in-situ measurements at the crown and inside the dam body. Based on hybrid generic algorithms (HGAs) and FE model, relevant material parameters were then back analysed by calibrating the vertical displacement response according to the monitoring data. The settlement values obtained by the calibrated model were aligned with the measurements, while the deformation moduli values obtained through back analysis were smaller than those from the laboratory test. Finally, the FE model was utilised to predict the future behaviour of vertical displacement, and the results show that after the construction period, the settlement tended to diminish, demonstrating that the dam was stable and that the future vertical displacement should be minimal.

Fahland (2004) used FEM to describe the deformation behaviour of a combined arch and gravity dam, Oker Dam, in operational condition. Among all external loads, hydrostatic pressure and temperature are the two main factors that should be taken into consideration in the analysis of dam deformation behaviour; and temperature induces delayed displacement

due to the delayed thermal response inside the dam, while the water pressure load induces immediate displacements on the dam. Through measurement and FE-simulation, the thermal and mechanical material properties were verified, and the load cases based on the recorded ambient conditions were simulated. The results show that comparable values were obtained by the FE model and other instruments including the inclinometer, pendulum wire and inclination. The developed simulation tool supports the comprehension of each deformation effect and the interpretation of measurement and monitoring.

Colombo et al. (2016) presented a methodology to validate simulated structural responses with corresponding monitoring data. In the transient thermal analysis, the initial condition was imposed on each node interior the dam with average temperature values, which was also assumed as the reference temperature for the thermal stress and strains, while the boundary conditions were based on the annual cycle of temperature variation. In the structural analysis, the temperature and hydrostatic load served as input loads to obtain displacement responses. To reproduce the structural displacement response, the stiffness values for various parts of the dam body differed based on the geo-mechanical investigations and laboratory tests, while the material property of the rock foundation was specified as homogeneous elastic. Finally, to calibrate the FE models, comparisons were conducted for a buttress concrete gravity dam and an arch concrete gravity dam between the measured temperature from thermometers and numerical results as well as between the measured upstream-downstream displacements and numerical results. The proposed approach was able to reproduce the dam deformation behaviour under seasonal varied thermal and hydrostatic loads.

Mirzabozorg et al. (2014) reported a static evaluation procedure of a double arch concrete dam. The established FE model was firstly calibrated by utilising the in-situ measurements in thermal and structural analyses. In the thermal analysis, the meteorological data recorded by a weather station near the dam site were used to define the boundary air and water temperatures. In the structural analysis, different loads were considered including temperature, hydrostatic pressure on the upstream face, self-weight of the dam and silt load at the dam heel. In the transient thermal analysis, the model was calibrated by comparing the computed temperature with thermometer measurements in different blocks of the dam; in the mechanical analysis, the numerical model was calibrated utilising the pendulum's recorded data at several timepoints, presenting different combinations of maximum, moderate or minimum water levels in the reservoir and warm or moderate ambient environmental temperatures. Then, different load combinations including usual and unusual cases were specified in the static safety evaluation of the dam; the obtained values of stresses at the upstream and downstream faces based on the calibrated numerical model were evaluated as acceptable considering the allowable tensile and compressive stresses, demonstrating that the dam was safe under the considered load combinations.

Table 2.1 summarises the main characteristics of the model used in the above numerical analysis conducted for different types of dams for health monitoring.

Table 2.1: Some typical dams and conducted numerical analysis

Literature	Dam name (country) opening year	Type	Measurement data	Load	Investigated items from FE model	FE model
Boberg et al. (2012)	Baozhusi (China) 2000	Concrete gravity dam Height 132 m Length 525 m	-	Self-weight, hydrostatic pressure, uplift, temperature	Displacement, stresses, Sliding stability	2-D Linear elastic model
Betzische (1998)	Fuerwigge (German) 1904	Quarry stone gravity Height 29 m Length 166 m	pore-water pressure, temperature	Hydrostatic pressure, temperature	Temperature, seepage, stability	2-D Linear elastic model
Léger et al. (1993a& 1993b)	Typical dam section corresponding to highest dam in Quebec (Canada)	Concrete gravity dam	-	Hydrostatic pressure, temperature	Temperature, Displacement, stresses	2-D linear elastic model
Tatin et al. (2015)	-	A concrete gravity dam	-	Hydrostatic pressure, temperature	Displacement	2-D linear elastic model
Liu et al., (2003a & 2003b)	Three-Gorges (China) 2008	Concrete gravity dam	-	Self-weight, Hydrostatic pressure	Displacement, Stability of dam foundation	2-D and 3-D linear solid isoparametric elements for rock and concrete of some critical dam sections
De Sortis et al. (2007)	Ancipa (Italy) 1953	Buttress dam	Displacement, temperature	Temperature, hydrostatic pressure	Temperature, displacement	3-D linear elastic model
Li et al. (2015)	Huangdeng (China) 2016	Roller-compacted concrete gravity dam Height 203 m Length 464 m	-	Gravity, Hydrostatic pressure, uplift, silt, wave, temperature	Stress, seepage field	3-D plastic concrete model of two typical dam sections
Maken et al. (2013)	Daniel Johnson (Canada) 1970	Largest Multiple arch dam Height 214 m Length 1315 m	Displacement, crack opening	Hydrostatic pressure, temperature	Temperature, Stress, thermal displacement, crack	3-D linear elastic/ nonlinear smeared crack models
Sheibany et al. (2006)	Karaj (Iran) 1961	Concrete double curvature arch dam Height 168 m Length 384 m	Water level, air/ concrete temperature	Hydrostatic pressure, temperature, self-weight	Temperature, stress	3-D elastic model
Zhou et al. (2011)	Shuibuya (China) 2008	Concrete-face rockfill dam Height 233 m Length 675 m	settlement	Hydrostatic pressure	Settlement	2-D nonlinear model
Fahland (2004)	Oker (German) 1956	Arch- gravity Concrete dam	Air/water/ concrete temperature, Inclination, displacements	Hydrostatic pressure, temperature	Displacement	3-D Linear elastic concrete model
Colombo et al. (2016)	-	a buttress gravity dam Height 80 m & an arch-gravity dam Height 75 m	Water level, concrete temperature	Hydrostatic pressure, temperature	Temperature, displacement	3-D elastic model
Mirzabozo et al. (2014)	Karun III (Iran) 2005	double curvature arch dam Height 205 m	Air temperature, water temperature, concrete temperature, displacement	Hydrostatic pressure, temperature, self-weight	Temperature, displacement, first principal stress, third principal stress, crown opening	3-D linear elastic model

### 3. Monitoring of deformation behaviour of Rappbode Dam

The Rappbode Dam is a concrete gravity dam built in the 1950s in the former German Democratic Republic. Detailed visualisations of its in-situ monitoring data can present preliminary understanding of the dam's time-varying ambient loading conditions and deformation behaviour. In this chapter, information concerning the construction history and a schematic plan of the investigated dam are firstly introduced. Then, the monitoring system is described, including pendulum plumb wire for displacement, the embodied thermometers within the dam and the manometer for uplift pressure. Thirdly, the recorded ambient variables are presented graphically, including the water level in the reservoir, uplift pressure at the dam base, ambient temperature at the dam crown and upstream side. Finally, the responses of temperature and displacement distribution in the dam are analysed based on the monitoring data.

#### 3.1 General information of the investigated dam

The Rappbode Dam is a concrete gravity dam 8 km northeast from Hasselfelde in the district of Harz in Saxony-Anhalt, Germany and is shown in Figure 3.1. The dam's construction began in 1938 and was later interrupted due to World War II, until 1959 when the dam finally commenced operation. Its full storage was issued on the 30<sup>th</sup> of October 1963, and some remediation for the dam body was conducted between 1995 and 2009 (Wouters, 2010). Figure 3.2 provides a view of the Rappbode Dam and shows that state road L96 runs along the dam crown, which makes the dam site approachable.

Together with other dams (the Königshütte Dam, Hassel Auxiliary Dam, Rappbode Auxiliary Dam, Wendefurth Dam and Mandelholz Dam) and retention basins, the Rappbode Dam forms the Rappbode dam system for flood protection in the eastern Harz mountains, a central German upland (Schmidt, 1992). The reservoir at the Rappbode Dam provides drinking water for nearby towns in the eastern Harz region, and the water in the reservoir behind the dam is used to generate hydroelectricity. With a maximum height of 106 m and reservoir volume of 109.8 Mio m<sup>3</sup>, the Rappbode Dam is the highest dam in Germany and forms the largest water reservoir in the Harz region. The dam crown has an elevation of 426.4 m above sea level (a.s.l.), and the reservoir area is about 3.9 km<sup>2</sup>. It extends in the southwest-northeast direction, is about 9 km in length and is usually only a few hundred meters wide, as shown in Figure 3.2. The characteristics of Rappbode dam are summarised in Table 3.1 (Wouters, 2010).



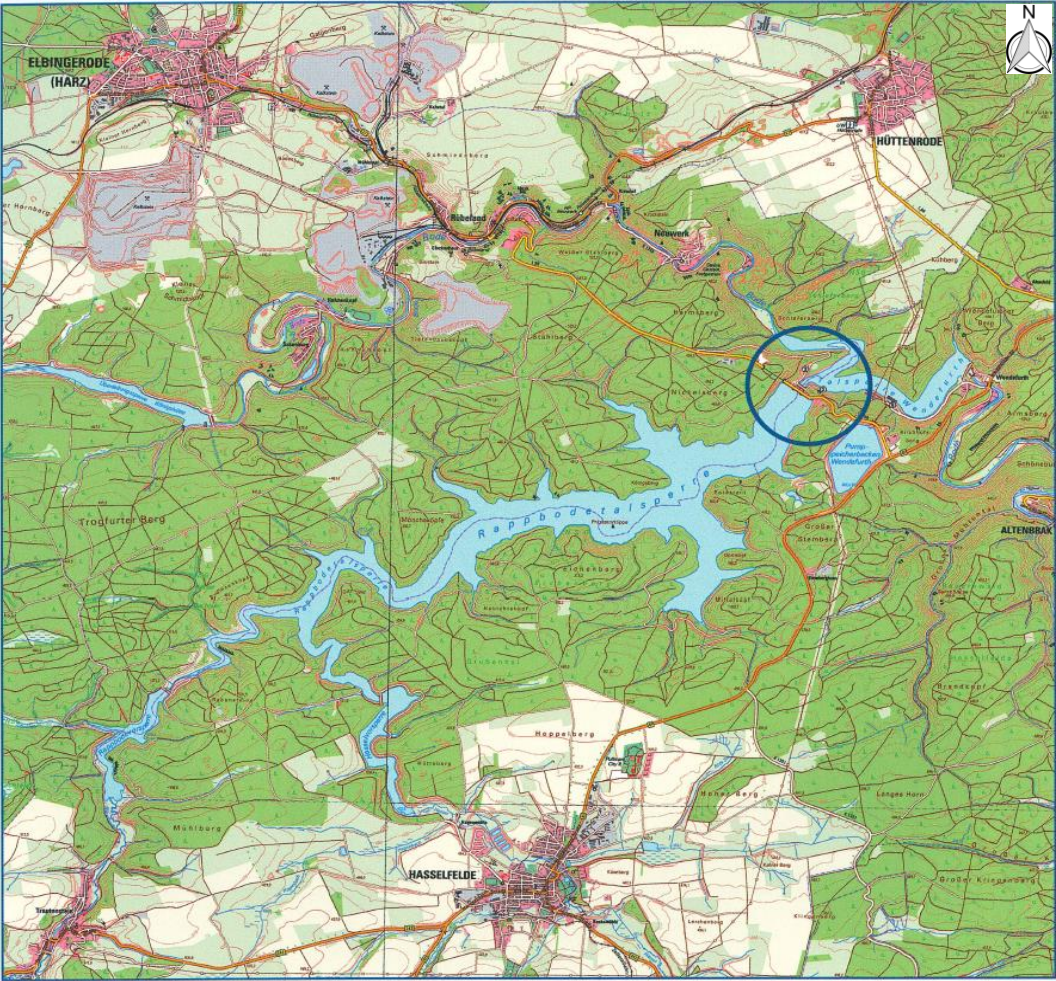


Figure 3.1: Location of Rappbode Dam (Wouters, 2010)



Figure 3.2: An overview of Rappbode Dam (Photo by Regional Association Harzer Urania e.V.)

Table 3.1: Main characteristics of Rappbode dam (Wouters, 2010)

Dam	
Type of dam	Gravity dam
Height	106.00 m
Length	415 m
Width at crown	12.5 m
Maximum bottom width	approx. 81 m
Concrete volume	approx. 860,000 m <sup>3</sup>
Tilt downstream	1:0.73
Tilt upstream	1:0.02
Reservoir	
Dammed stream	Rappbode, Hassel
Highest storage level	423.60 m a.s.l.
Total capacity	113.06 Mio. m <sup>3</sup>
Operational capacity in summer	105.11 Mio. m <sup>3</sup>
Operational capacity in winter	95 Mio. m <sup>3</sup>
Biggest water depth	89
Area of the reservoir	395.30 ha

The dam was constructed as a gravity dam made of plain concrete. Shown in Figure 3.3, the dam is comprised of 30 blocks, each with a maximum width of 16 m. The blocks were numbered during the dam construction from 1 to 29 from left to right valley from an upstream view (Wouters, 2010). The spillway exists at blocks 13, 14, 15 and 16 and consists of a crown overflow with a width of 64 m. There are 6 galleries in the dam and 25 vertical shafts at the upstream side in the dam, which allow visually inspecting the dam from inside, draining seepage water in the dam, installing measuring equipment and so on (Rißler, 1998).

Regarding the foundation of the dam, fractures and cracks were found at the natural bedrock. To reinforce the foundation during the initial construction period, small pieces found at the site were carefully removed, concrete was injected, and the foundation surface was thereby sealed. To protect the foundation from seepage and strengthen the foundation, a double-row grout curtain was injected into the initial construction to a depth of 60 m under the dam heel and 35 m under the dam toe (Wouters, 2010).

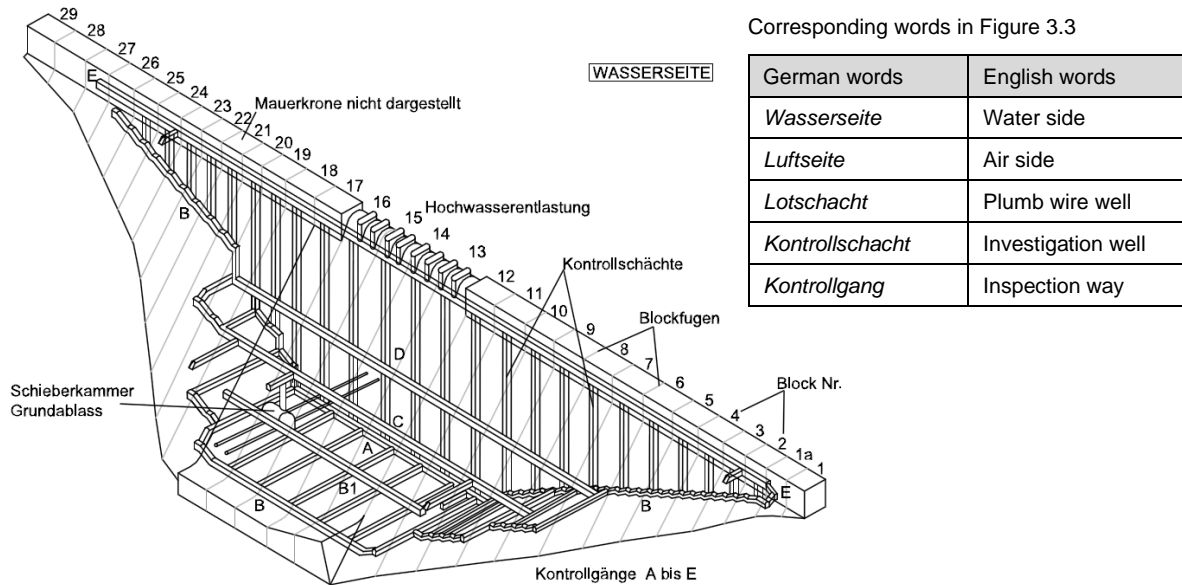


Figure 3.3: The isometry of the dam with No. of the blocks and the inspection way system (Wouters, 2010)

## 3.2 Monitoring in the investigated dam

The monitoring system and measurement data were provided by the Dam Management Company of Saxony-Anhalt (German: Talsperrenbetrieb Sachsen-Anhalt). The measure locations for displacements, concrete temperatures and uplift pressures are described in this section. Because the monitoring system was installed in 2003 rather than during the construction phase, the monitoring phases are narrowed to the operational phase of the dam.

### 3.2.1 Monitoring of horizontal deformations of the Rappbode Dam

Horizontal deformations can be measured by pendulum plumb wire and floating plumb wire. In the case of the Rappbode dam, the pendulum instruments were installed in nine vertical shafts at the joint of two adjacent blocks to measure the horizontal displacements of nine blocks. Shown in Figure 3.4, the horizontal displacements are measured at blocks 7, 9, 11, 13, 14, 17, 18, 20 and 23. The suspensions of the plumb wires were installed at different elevations, including C (dam crown), B (top inspection gallery), A (dam middle) and D (dam bottom). The reading consoles for each pendulum plumb wire were located at the bottom of the corresponding shaft. The measurements from these pendulums represent the movements at the suspensions of C, B, A and D relative to the corresponding console location of each pendulum, and all measurements are read at the console. The elevations of suspension locations and reading consoles are listed in Table 3.2 and Table 3.3. One floating plumb wire was installed at the bottom of block 13, which allows detecting movements resulting from displacements and inclinations of the dam of the point at the reading console compared to the

fixed anchor point 35 m deep in the rock. The data were recorded monthly for every measuring point since 30<sup>th</sup> September 2003.

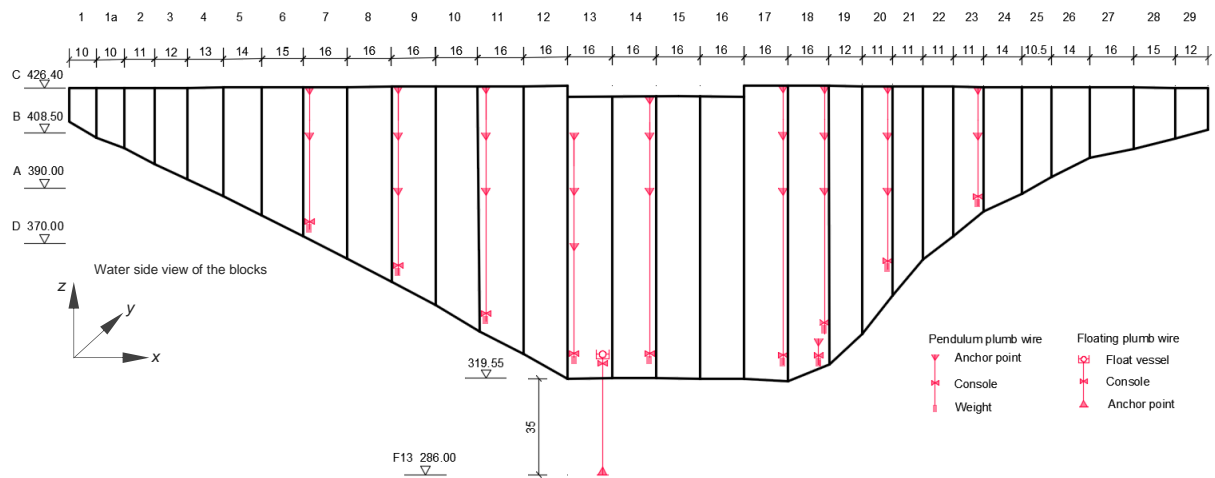


Figure 3.4: Upstream view of installed pendulums and floating pendulum locations

Table 3.2: Locations of suspensions and console of pendulum in the Rappbode Dam

Block joint	Block	Suspension C crown (m a.s.l.)	Suspension B (m a.s.l.)	Suspension A middle (m a.s.l.)	Suspension D bottom (m a.s.l.)	Reading points Console position (m a.s.l.)
6/7	7	426.40	408.50	-	-	378.05
8/9	9	426.40	408.50	390.00	-	362.65
10/11	11	426.40)	408.50	390.00	-	345.95
12/13	13	-	408.50	390.00	370.00	327.60
14/15	14	426.40	408.50	390.00	-	327.60
17/18	17	426.40	408.50	390.00	-	327.60
18/19	18	426.40	408.50	390.00	-	341.35
20/21	20	426.40	408.50	390.00	-	363.90
23/24	23	426.40	408.50	-	-	387.55

Table 3.3: The location of the floating pendulum

block joint	block	Plumb anchor (m a.s.l.)	Reading console (m a.s.l.)
13/14	13	approx. 286	327.60



As shown in Figure 3.4, the coordinator system in this thesis is defined as follows: for x direction (longitudinal direction), the positive direction is from left valley to right valley from an upstream view of the dam; for y direction, the positive direction is from upstream to downstream face; while for z direction, the direction is from bottom to top. The horizontal movements are recorded by the pendulum in x and y directions.

### 3.2.2 Monitoring of concrete temperature of the Rappbode Dam

The temperature variations in the dam can be monitored by thermometers embodied in its body. In the case of the Rappbode Dam, the reading of concrete temperature data occurred using 21 thermometers (shown in Figure 3.5) installed at several elevations and across the thickness of the concrete section of block 18 (shown in Figure 3.3).

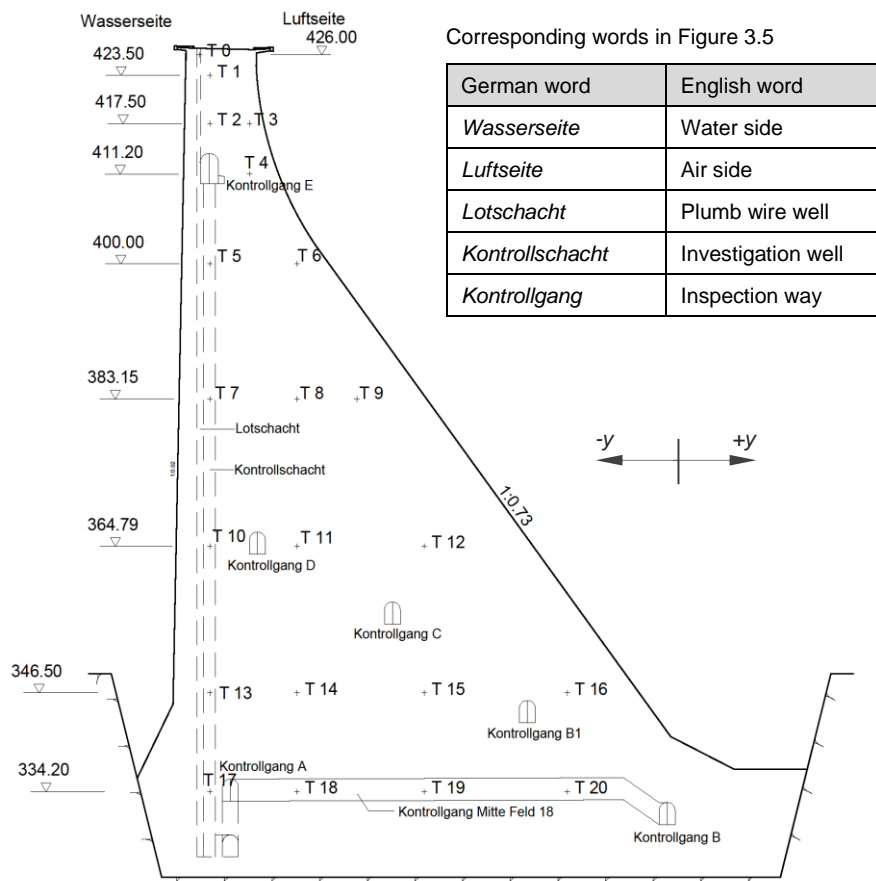


Figure 3.5: Cross section view of embodied thermometers locations for T0-T20 in block 18

An overview of locations T0 - T21 is shown in Figure 3.5, where T stands for thermometer. These thermometers' power supply boxes are located in inspection galleries near each concrete temperature measure position. The concrete temperature values recorded in block 18 present the temperature distribution inside the dam, which are used to calibrate the temperature distribution within the dam body in the transient thermal analysis, which is detailed in Chapter 5.

### 3.2.3 Monitoring of uplift pressure at base of the Rappbode dam

Uplift pressure is water pressure at the base of the dam and would lift the structure upwards. Due to their wider base, the uplift pressure at the base of concrete gravity dams could be particularly problematic regarding anti-overturning stability (Golze, 1977; Ratnayaka et al., 2009). The uplift pressure varies from the dam heel to dam toe at the wide base and it is desirable to distribute measurement points along the dam base in the upstream-downstream direction. Figure 3.6 shows a top view of the measuring points at the base of Rappbode Dam, which includes 493 points spread from blocks 3 to 27 (shown in Figure 3.3) in the distance range of 37-387 m from the left side of the dam from an upstream view. The measured locations are not in a single horizontal plane since the base of the dam is not in one plane, i.e., the base for the lateral blocks of the dam is higher in elevation than the central blocks. The water pressures at the base of the dam are then measured monthly by manometer since July 2003.

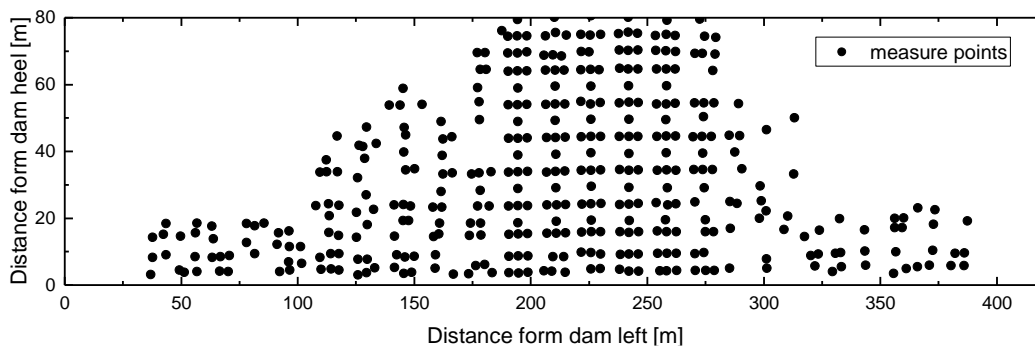


Figure 3.6: Top view of measuring points for uplift pressure at base of the dam

## 3.3 Analysis of recorded ambient conditions at the site

As mentioned in Section 2.2, the measured items include ambient environmental conditions and structural responses. In the case of the Rappbode Dam, the ambient conditions include the water level in the reservoir, air temperature, water temperature and water pressure at the base of the dam. The horizontal displacements and concrete temperature in the dam body are considered regarding structural responses. Graphical visualisations of ambient conditions are presented in this section by displaying the ranges and time series of the recorded items.

### 3.3.1 Water level in the reservoir

Water levels were measured almost monthly, and analysis is focused on time-varying characteristics, the range and median of the recorded water level values and the detection of any abnormalities. Monitoring data are analysed concerning the period from 30<sup>th</sup> September 2003 to 2013.

The time series and boxplot of water level in Figure 3.7 show that the minimum water level during this time period is 397.5 m a.s.l. (corresponding to a 62.9 m depth of water in the reservoir), whereas the maximum value is 422.7 m a.s.l. (corresponding to a 88.1 m depth of water in the reservoir), and the difference between the maximum and minimum values is around 25 m. The mid value of all recorded data is 416.0 m a.s.l., and 80% of the values vary from 407.2 to 420.4 m a.s.l. while 50% of the values vary from 411.4 to 419.2 m a.s.l. (i.e., 80% of the values fluctuate in the scope of 13.2 m and 50% of the values fluctuate in the scope of 7.8 m).

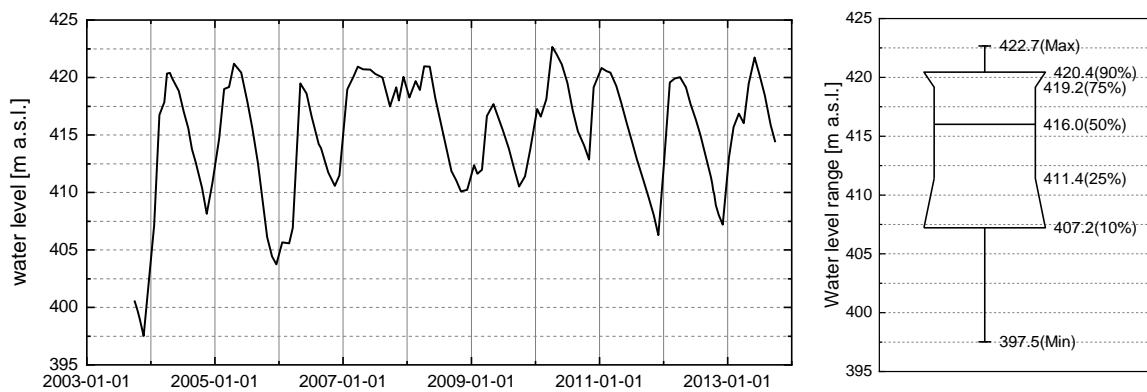


Figure 3.7: Time series (left) and boxplot (right) of water level in the reservoir

When compared with the dam height of 106 m, the water level varies in a narrow range. In terms of the annual fluctuation trend of water level, the lowest water level normally occurred at the end of the year before the water level gradually increased until May or June and reached its peak. An exception occurred in the second half of 2007 and the first half of 2008, when the water level stayed in a relative steady state and varied in a small range of 417.49 m and 420.96 m. A weather review (2007) reported that in the 2007, precipitation was well above the average of 789 litres with a Germany-wide area average of 928 litres per square meter, and most rain occurred in the Harz mountains litres, where there was more than 2714 litres of precipitation per square meter (“Wetterrückblick,” 2007). This could primarily cause the abnormality in water level variation at the end of 2007 and beginning of 2008.

### 3.3.2 Uplift pressure at the base of the dam

To show the uplift pressure distribution, Figure 3.8 displays the measured pressure at the bases of different blocks on two different dates. The blocks have different heights and thicknesses at the base, and the average elevation of the measurement points and thickness of each block base are listed in Table 3.4, showing that the distance from dam heel to dam toe decreases with the increase of the elevation at the base. The uplift pressure values are available in the corresponding thickness ranges. The two dates presented in Figure 3.8 are

29<sup>th</sup> February 2008 and 8<sup>th</sup> August 2011, representing wintertime and summertime respectively.

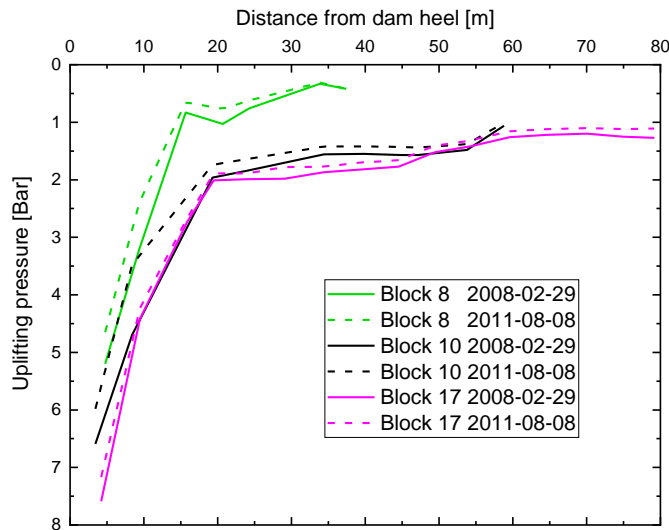


Figure 3.8: Uplift pressure profile under three different blocks on two different dates

Table 3.4: Elevation of some blocks at the base

Nr. of blocks	Average elevation of measure points at this block (m a.s.l.)	Thickness of the block at base (m)
17	322.0	81
10	342.8	60
8	359.6	39

To explain the uplift pressure distribution in Figure 3.8, the theoretical uplift pressure distribution at the base of a concrete gravity dam (Figure 3.9) must be firstly introduced. The body of a gravity concrete dam is normally assumed to be leak-proof (Riβler, 1998). Due to the foundation permeability, the flow of water below a concrete dam from the upstream side to the downstream side, induces uplift pressure at the base of the dam. Figure 3.9 depicts that the location under the dam heel shows the greatest uplift pressure with a value of  $\eta\gamma_w h$ . When there is no gallery at the bottom in the dam (Figure 3.9 (a)), a linear tendency can be found at the base from upstream to downstream. However, when a gallery exists at the bottom of the dam (Figure 3.9 (b)), it has a relieving effect on the uplift pressure distribution and acts as a drainage gallery for the dam and foundation to drain into, thereby positively impacting the uplift pressure distribution (Riβler, 1998).

As shown in Figure 3.8, the maximum pressure at the base of each block on 29<sup>th</sup> February 2008 is around 0.5 Bar greater than that on 8<sup>th</sup> August 2011. Because the recorded reservoir levels on these two dates are 418.37 m a.s.l. and 412.58 m a.s.l. respectively with a difference

of 5.79 m, the difference of the maximum pressure is aligned with the theoretical value. The dramatic decline in each curve of uplift pressure distribution is due to the drainage galleries interior dam body.

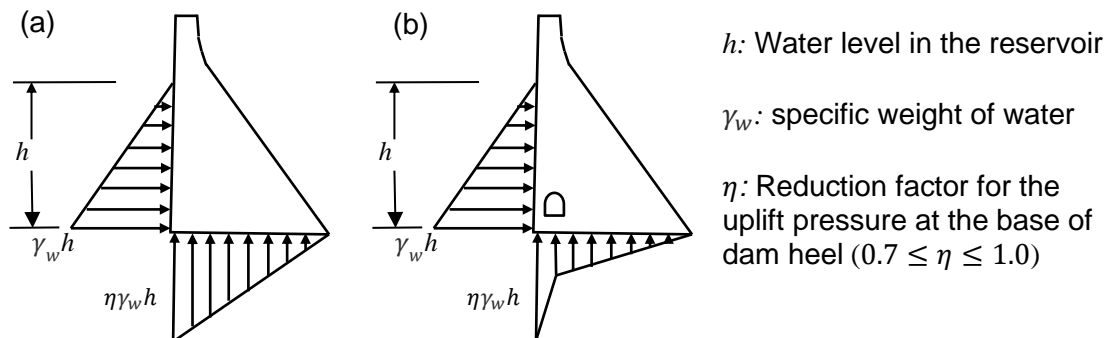


Figure 3.9: Schematic of uplift pressure at the dam base with and without a drainage system (Riðler, 1998)

The time series of uplift pressure and water level are plotted in Figure 3.10 to determine the relationship between water level and uplift pressure. The investigation includes certain points spread through the thickness of the dam at different blocks. These points are grouped with a, b, c and d, with the number before the group name representing the block number and location. Diagrams of top views of these locations at the dam base are displayed in Figure 3.10, and the elevation for each location is listed in brackets. The water level variation in the window is presented with a dotted line. Figure 3.10 shows that the fluctuations of the uplift pressures are aligned with the fluctuation of water level, i.e., when the water level decreases/increases, the uplift pressure at these points decrease/increase.

Among these investigated points, 14-a presents the greatest value with the lowest elevation of 321.47 m a.s.l., and its uplift pressure varies between 5.56 Bar and 8.14 Bar. The uplift pressures at 10-a and 19-a fluctuate between 4.59 Bar and 7.00 Bar and 4.86 Bar and 7.24 Bar respectively. For the side-located points 3-a with an elevation of 397.10 m a.s.l. and 27-a, with an elevation of 397.10 m a.s.l., the uplift pressures are much smaller, varying between 0.10 Bar and 2.08 Bar and 0 and 1.13 Bar respectively.

When comparing the elevation of a point and the corresponding uplift pressure at positions of group a close to the dam heel, it can be seen that, the higher the elevation of a point, the lower the corresponding uplift pressure. The uplift pressures at positions of groups b, c and d show similar characteristics, but their fluctuation ranges are smaller than those of group a at the same block. The synchronous change in water level and uplift pressure demonstrates that the water level changes in the reservoir result in immediate uplift pressure changes at the base for this concrete gravity dam.

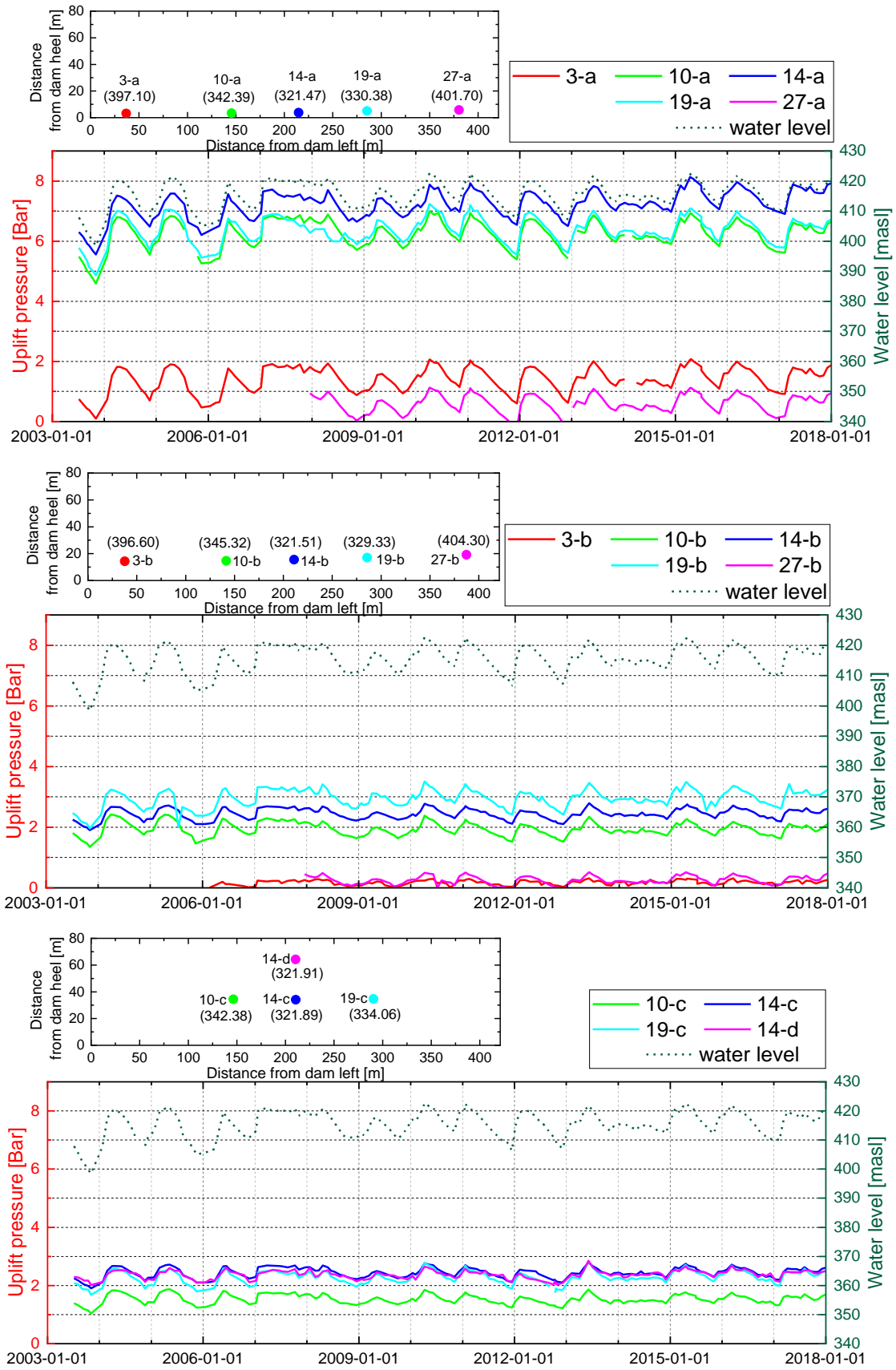


Figure 3.10: Comparison of water level and uplift pressure

### 3.3.3 Ambient temperature at dam crown

The ambient air temperature of Rappbode Dam is measured at the crown of block 28 (shown in Figure 3.3). The values were recorded at 7 am. Before 2008, the ambient temperature was recorded every second day, and then from the beginning of 2008, the measurement was performed each day.

The air temperatures from 2003 to 2016 are displayed in Figure 3.11, which depicts an annual sinusoidal vibration cycle. Based on the recorded air temperature, the temperatures slowly rise from spring to summer and fall again in the winter. Annual cycles are observed with the maximum and minimum occurring around January and July. The highest air temperature appeared on 11<sup>th</sup> July 2010 with a value of 27.5 °C, and the coldest day was 05<sup>th</sup> Feb. 2012 with a value of -17.5 °C. The box plot of these recorded temperatures presents that 80% of these values are in the range from -1.7 °C to 16.9 °C, and 50% are from 2.4 °C to 12.8 °C, with a median of 7.5 °C.

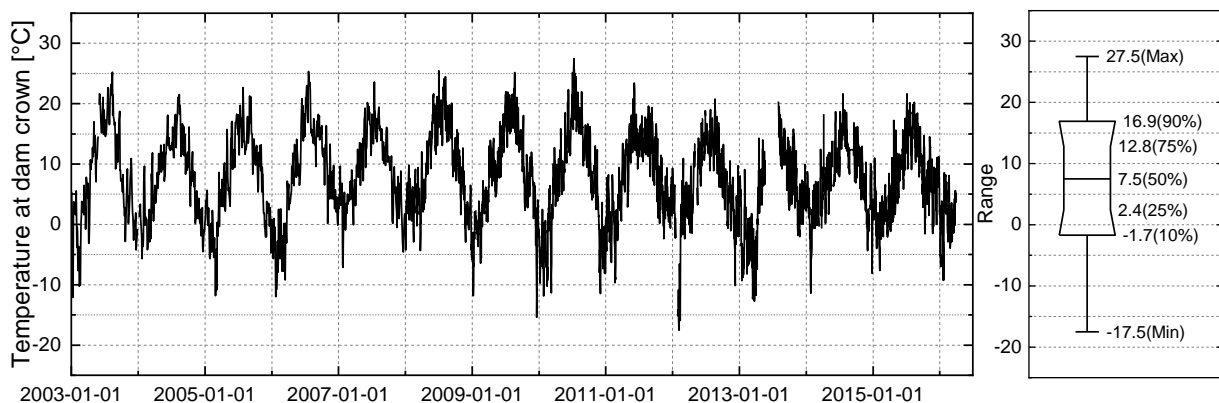


Figure 3.11: Time series and box plot of ambient air temperature at the dam crown

### 3.3.4 Ambient temperature at water side of the dam

The ambient temperature at the dam's water side was vertically measured at the position parallel to the upstream face of the dam, with a distance of 1.5 m away from the upstream face and at elevations from 350 m a.s.l. to 425 m a.s.l. for every 10 cm. This means that the upstream ambient temperature can regard water temperature when this location is under the water level or air temperature when the location is above the water level. The temperatures at the water side have been recorded monthly since 2009.

The temperature distributions for certain days are displayed in Figure 3.12 to reveal the characteristics of water-side temperature distribution along elevation. The water levels at identical dates are marked with a blue dot on each curve, which depicts that the temperatures remain the same along the height below the elevation of 385 m a.s.l. and above the water surface. However, the reasons for the same temperatures at these two zones differ, because

the water temperature receives little to no influence by the ambient air temperature for the zone below the elevation of 385 m a.s.l. but for the temperature above water level, it presents actually the ambient air temperature. For the water temperature under the water surface, the temperature at a certain depth has almost the same values as the ambient air temperature before presenting a steep decrease until reaching around 5 °C. On different dates, however, there are some differences for this certain depth. For example, the data on 2011-11-07 (black line) and 2011-05-06 (red line) illustrates that the air temperatures (temperature above the water surface) are almost the same, while the temperatures beneath the water surface show a deeper range with accordance to air temperature on the black line than the red line. For different season, even the ambient air temperature is identical, the water temperature distribution beneath the water surface is not identical.

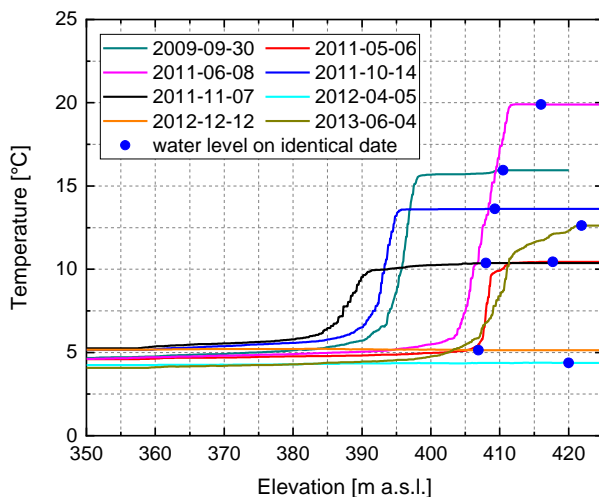


Figure 3.12: Ambient temperature distribution at water side and water level on identical date

To investigate the variation of temperature distribution by season, Figure 3.13 depicts the water side temperature distribution in 2012 with a coloured contour plot, with corresponding water level values marked with a dotted line. The water level acts as a separating line, above which the temperature presents the air temperature and below which the water temperature. The ambient temperature at the water side changed between a homogeneous distribution in cold seasons and a layered distribution in warm seasons. The warmer ambient temperatures at the water side were measured during the months of July and August for the upper part of the dam with a maximum value of 20.9 °C. The lower temperatures were measured during the months of January, February or December, which were between 2.6 and 4.9 °C. For the ½ upper area of upstream face, the ambient temperature presents a seasonal difference, while the temperature changes slightly throughout a one-year period for the ½ lower area in the reservoir. Comparing the colour contour with the water level shows that above the water level, the temperatures stay the same for each date since they present the air temperature; however, below the water surface lies a transition zone wherein the temperature decreases while the



depth increases. The contour graphics of ambient temperature at the water side for other recorded years are listed in Appendix A and the same characteristics concerning the ambient temperature at water side are obtained.

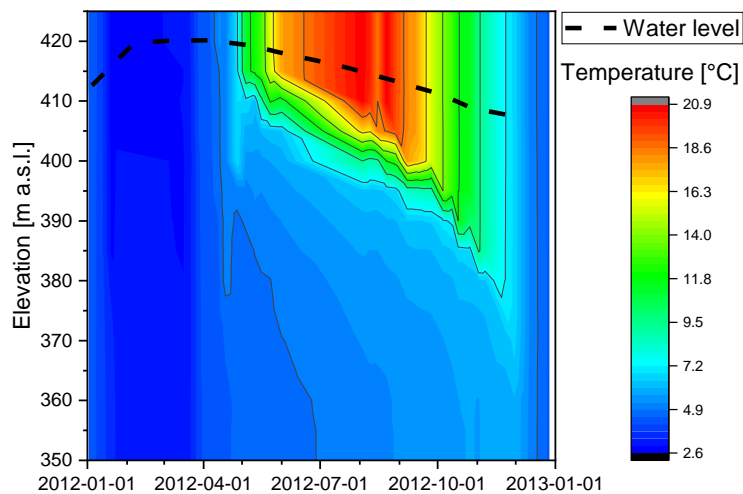


Figure 3.13: Ambient temperature profile at water side and water level in 2012

In order to check the water side ambient temperature changes over time, the time series of water temperature for elevations between 350 to 385 m a.s.l. and elevations between 385 to 425 m a.s.l. with a distance of 5 m are displayed in Figure 3.14 and Figure 3.15 respectively. Chapter 3.3.1 described that the water level was never below 385 m a.s.l., and thus in Figure 3.14, all temperatures represent water temperature values in the reservoir. The lowest temperatures occur at the beginning of a year, while the temperature rises and a slight difference for different elevations can be observed during the summer months. In October or November, the peak value of water temperature is reached for each year, and the tendency of the water temperature change for the eight different elevations is similar. In Figure 3.15, analogous histories for different years are shown for different water layers, and the temperature differences for different elevations are more obvious than those in Figure 3.14. Since the highest water level in the reservoir is 423.6 m a.s.l., the temperature at 425 m a.s.l. always presents the ambient air temperature. The temperatures at elevations between 415 and 425 m a.s.l. show similar time series and neglectable temperature differences. For the elevations from 390 m a.s.l. 415 m a.s.l., the lower water layer warms slower than the adjacent upper water layer, and thus they do not simultaneously reach the peak value. When becoming cold, the upper water layer begins to cool earlier until reaching the same temperature of the lower adjacent water layer, at which point they begin to cool together.

Based on these analyses, the ambient temperature at water side surface should be described as water temperature layers rather than as a single value. The  $\frac{1}{2}$  lower part of the upstream face can be one layer, while the upper part of the upstream face should include additional layers. To simulate heat transfer using a numerical model, different values at different layers

on the boundary should be specified as the ambient temperature boundary conditions at the water side.

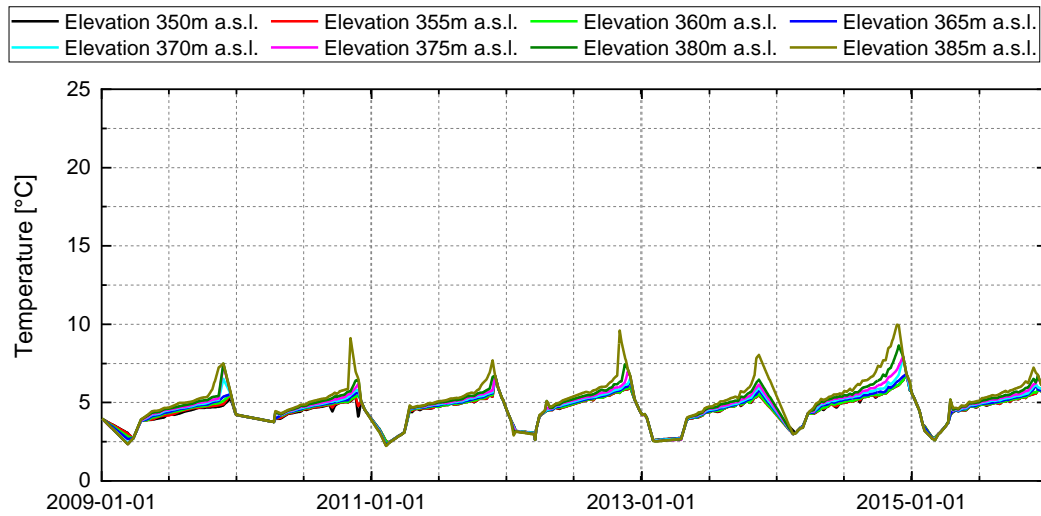


Figure 3.14: Time series of ambient temperature values for lower part of upstream face

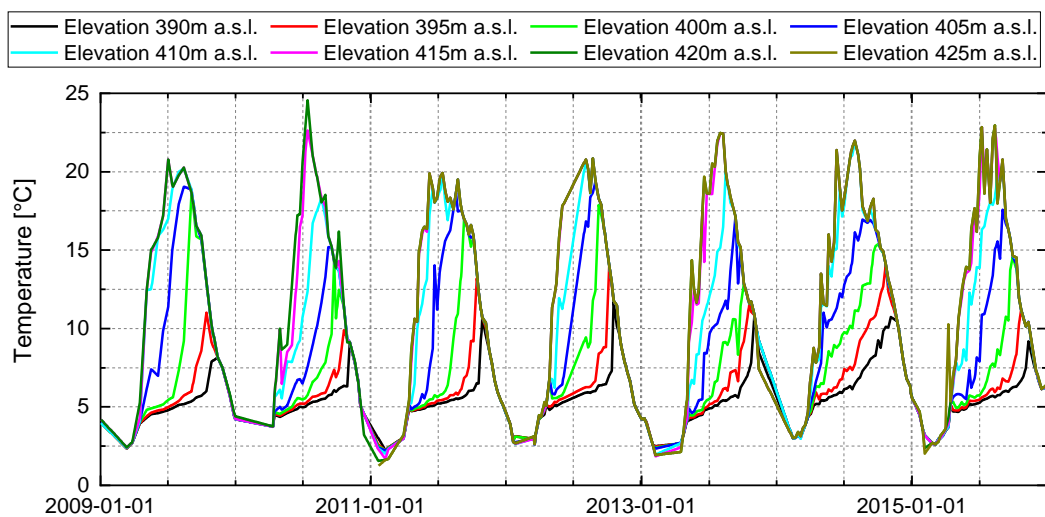


Figure 3.15: Time series of ambient temperature values for upper part of upstream face

### 3.4 Analysis of measured responses of the dam

The measured responses of temperature distribution in the dam body and displacements at measure points are analysed in this section. The monitoring of Rappbode Dam began from September 2003 following renovation. Hence, the recorded temperatures present the temperature values after the recorded date, and the influence of heat of hydration of cement on the temperature distribution during the construction processing was not included. Regarding the displacements, the deformation before the recorded data is unknown, and the variations of the recorded responses are consequently foregrounded.

### 3.4.1 Temperature within the dam body

As described in Section 3.2.2, the temperatures inside the dam are measured at 21 points (shown in Figure 3.5) in block 18 (shown in Figure 3.3). This section displays the temperature measurements with time series of the measurements, the ranges of the measurements at each measure point and the detection of the phase shift for different measurement points with different distances to the exposed downstream face.

#### *Time series of the temperatures in the dam*

The time series of temperature readings at 21 measuring points in block 18 is depicted in Figure 3.16. The dataset includes about 120 values from July 2003 to October 2013, which is about one value per month.

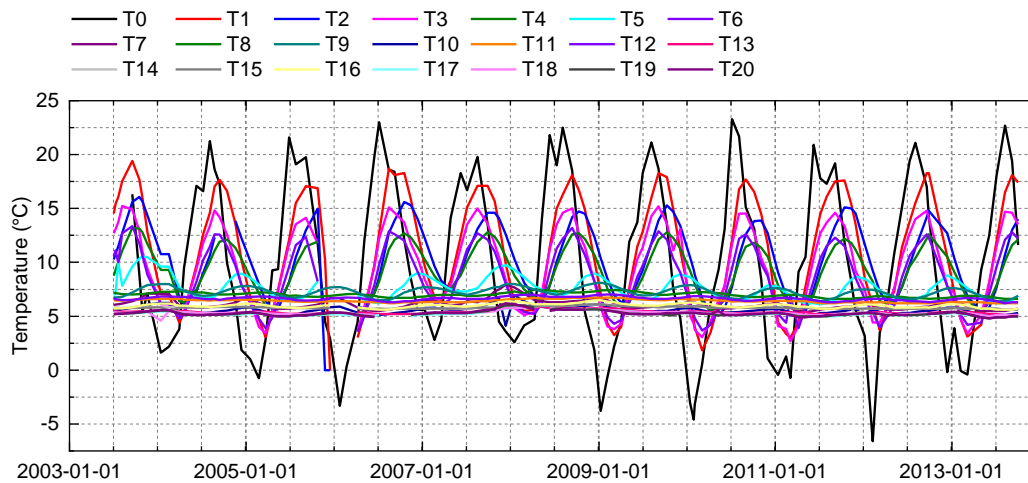


Figure 3.16: Time series of temperatures at T0-T20

The temperature values present annual variation cycles for all measuring points, which can be divided into two groups: T0, T1..., T6, which present greater variation with larger amplitudes throughout a year; and T7, T8..., T20, which present almost constant temperatures throughout a year. As shown in Figure 3.5, the measurement points T0-T6 are in the upper thinner part of the dam, which belongs to a temperature-prone zone, while T7-T20 are located in the lower thicker part of the dam. For the time series of T1-T6, there are different peak values for different points, and they occur in different phases, i.e., different phase delays are detected for different locations. Hence, there are no fixed global phase shift of the temperature inside the dam.

Figure 3.17 shows a comparison of temperatures at T0, air temperature and water-side temperature at an elevation of 425 m a.s.l. (wt425), to cross-check the ambient temperatures. The temperature sensor T0 is positioned about 0.3 m deep inside the concrete from the top surface of the dam, and its temperature changes analogous with the ambient temperature. The water-side temperature at 425 m a.s.l. presents the air temperature since this location is always

above the water. Except for the difference from recording frequency of the data, the three datasets of temperature values are comparable and show the same tendency.

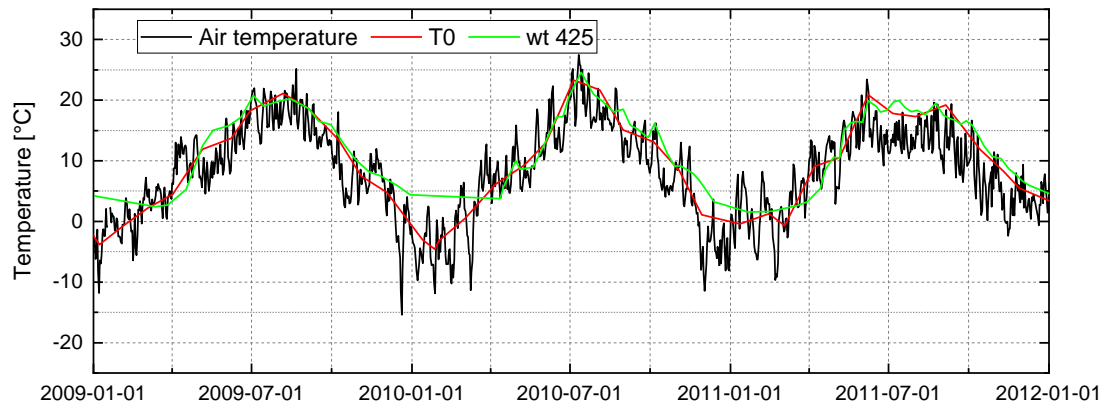


Figure 3.17: Time series of air temperature, T0 and water temperature at height of 420 m

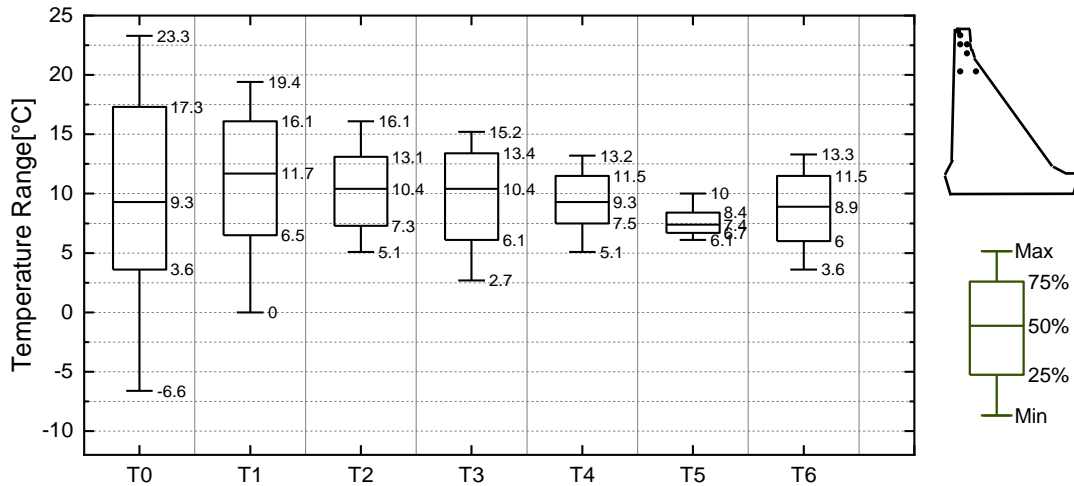
### *Temperature ranges*

To investigate temperature changes, the ranges of concrete temperatures for these 21 measure points are displayed in Figure 3.18 using a boxplot. The location of the measure points is shown in Figure 3.5.

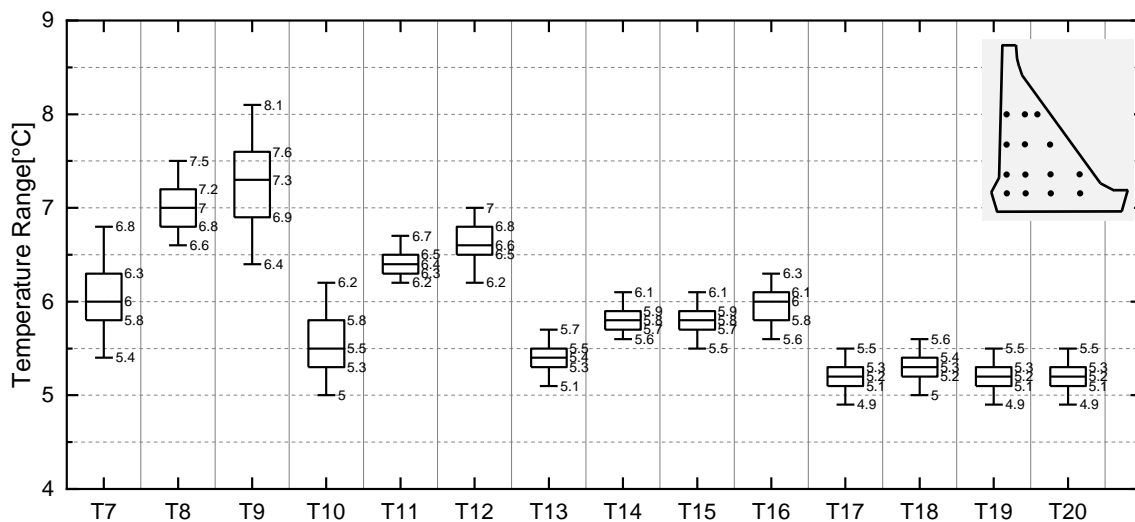
For all locations except T0, the temperature values were never below 0 °C. As shown in Figure 3.18 (a), the temperature variation at T0 is most noticeable among the measuring points T0-T6, varying from -6.6 to 23.3 °C with a median of 9.3 °C and 50% of the values ranging between 3.6 °C to 17.3°C--which includes not only the lowest but also the highest temperatures among all recorded concrete temperatures. T0 is the most vulnerable to external temperature influences among all 21 measured locations. Second place in terms of temperature variation range is occupied by T1 with a value of 19.4 °C, but T1 has the greatest value in terms of median. T2 and T3 are located at the same elevation, and their temperature variations are comparable with the same medians. T4 and T6 are located at different elevations in the vicinity of the exposed downstream face, the temperature variation range at T4 is slightly smaller than T6's, but the median at T4 is greater than that at T6. The temperature at T5 varies between 6.1 °C and 10 °C, which is narrowest among these 7 upper measuring points. As shown in Figure 3.5, T5 is located in vicinity of upstream face, where the corresponding external water temperature fluctuates less than the external air temperature. The thermometers situated near the surface are highly influenced by the local external temperature.

As shown in Figure 3.18 (b), the ranges of temperature variation are smaller than those in Figure 3.18 (a). The temperature at T9 varies between 6.4 °C and 8.1 °C, presenting the greatest range as well as greatest median among T7-T20. For locations T11-T20, the temperature varies less than 1 °C, while for T17-T20 located in the same row with the lowest

elevation, the temperatures vary in approximately the same range and present the same median.



(a): Boxplot of concrete temperatures for locations T0-T6



(b): Boxplot of concrete temperatures for locations T7-T20

Figure 3.18: Ranges of the recorded temperature values for T0-T20

*Phase shift of temperature at different measurement points*

To investigate the phase shift of temperature variation at different locations, points T0, T3, T6, T9 and T12 located in vicinity of the downstream face are selected. The time series of temperatures for these locations is depicted in Figure 3.19, and the perpendicular distance from each of the thermometer locations to the downstream face is listed in Table 3.5.

From T0 to T12, the depth of the points from the surface increases from 0.4 m to 11.1 m. Together with Figure 3.19, it is demonstrated that the concrete temperature variations show decay concerning amplitude with the increase of a location's distance from the exposed downstream face. Different locations have different phase delays, where the farther the

location from the exposed downstream face, the greater the time delay to reach the peak temperature.

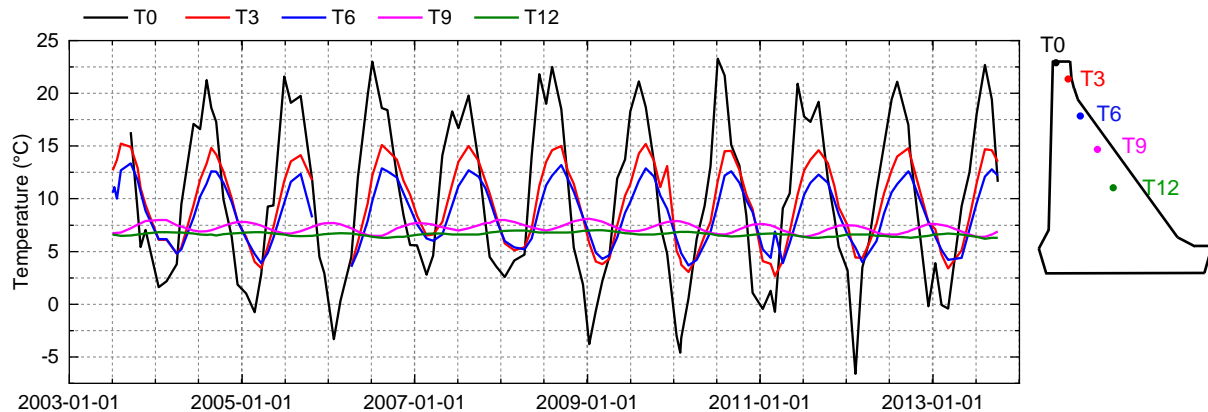


Figure 3.19: Time series of temperature at T0, T3, T6, T9 and T12

Table 3.5: Perpendicular distance to dam downstream face from T0, T3, T6, T9 and T12

Points	Perpendicular distance to dam downstream face /m
T0	0.4
T3	1.8
T6	3.3
T9	7.2
T12	11.1

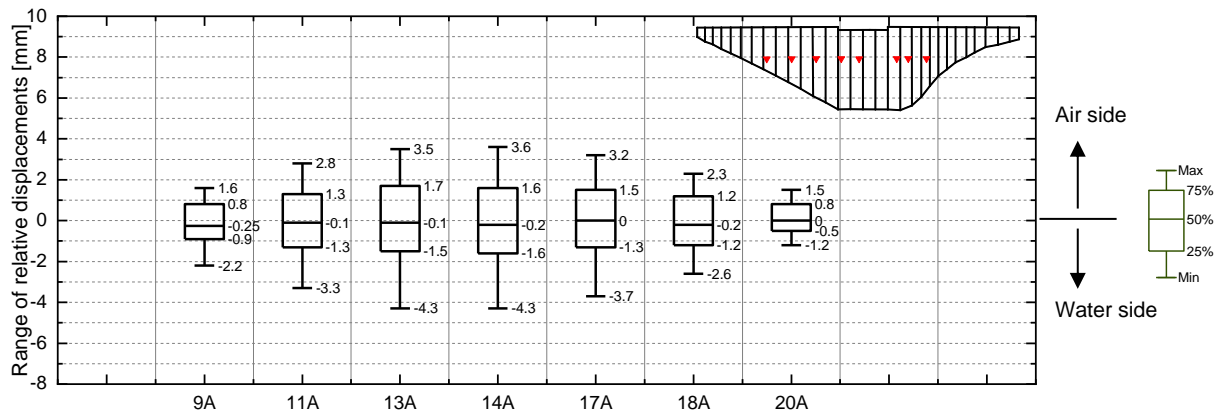
### 3.4.2 Horizontal displacement in upstream-downstream direction

Due to the structural configuration and thrust from water in the reservoir, the deformation in the upstream-downstream direction of a concrete gravity dam is the main concern in its deformation behaviour analysis. Based on the measurements, this section investigates the displacements in the upstream-downstream direction, including the range of displacements at each measurement point, the visualisation of the relative displacements and the displacements at dam base. In addition, to comprehend the deformation behaviour of the dam, the time series of displacements at comparable measuring points are compared.

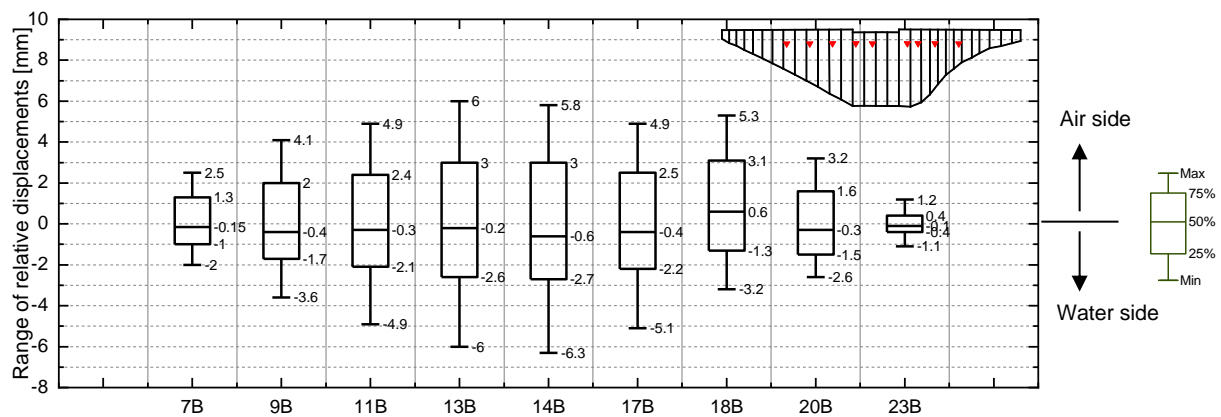
#### *Ranges of the measured relative displacement*

To investigate the variations of displacement with time, the corresponding mean value of the recorded values is removed from the recorded values for every measurement point. The variation ranges of relative displacements in the upstream-downstream direction are presented with a box plot in Figure 3.20, and the location of suspensions A, B and C are shown in Figure 3.4. In Figure 3.20, the horizontal axis labels represent the number of blocks and suspension

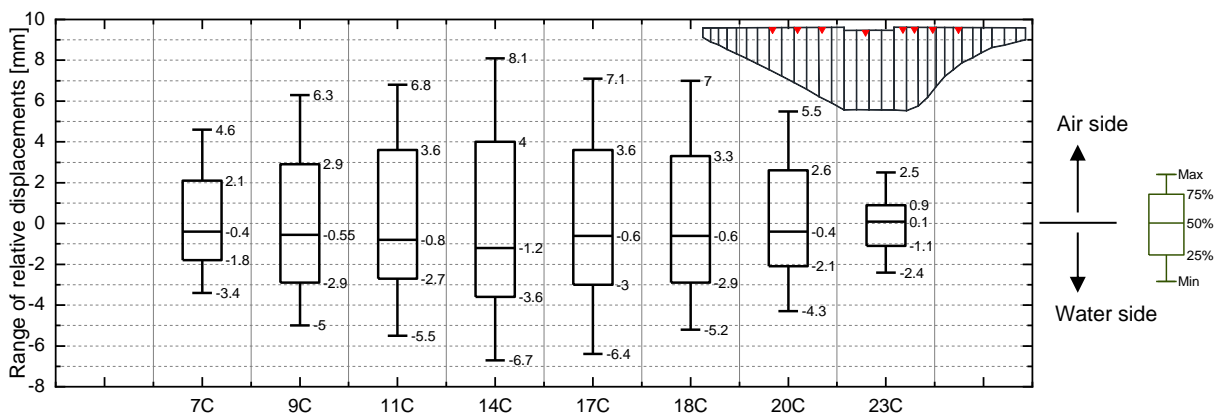
locations, and the box plot data include about 120 values from September of 2003 until September of 2013 for each measurement point.



(a): Range of relative displacements of suspension A at elevation 390 m a.s.l.



(b): Range of relative displacements of suspension B at elevation 408.5 m a.s.l.



(c): Range of relative displacements of suspension C at elevation 426.4 m a.s.l.

Figure 3.20: Ranges of measured relative displacements to mean value in upstream-downstream direction

As shown in Figure 3.20 (a), the relative displacement range at suspension A differs from block to block, where the central block has a relative larger range than the lateral block for the measure points at the same suspension elevation, i.e., the further a block from the centre of the dam, the narrower the range of relative displacements detected at this block in the

upstream-downstream direction. However, the ranges of relative displacements for symmetrically located blocks present symmetrical characteristics; for example, the ranges of relative displacements at 9A, 11A and 13A are comparable with those of 20A, 17A and 18A respectively. The largest range at suspension A occurs at central block 14 with a value of 7.9 mm and the smallest range at block 20 with a value of 2.7 mm. Since the mean value is removed from each dataset of displacement, the median of each relative displacements at suspension A is quasi 0.

When comparing the three figures in Figure 3.20, analogous characteristics in Figure 3.20 (b) and Figure 3.20 (c) can be seen with that in Figure 3.20 (a). With increased elevation, the variation ranges also increase for identical blocks. The measurement points at suspension C are more significant than the lower locations regarding the variation ranges of relative displacements in the upstream-downstream direction.

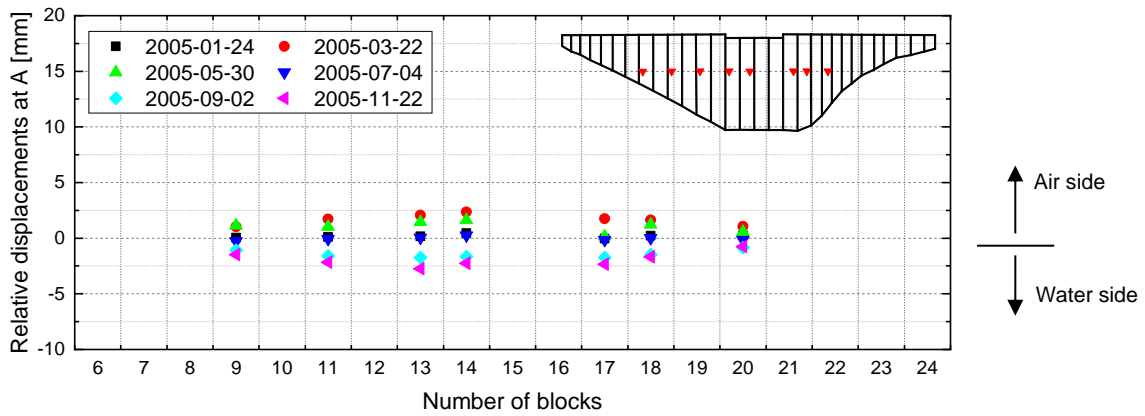
Among all the measurement points in different blocks, 14C is the most significant location concerning the variation range of displacements in the upstream-downstream direction, which shows the largest range of 14.8 mm with a median of -1.2 mm, with 50% of the relative displacements ranging between -3.6 mm and 4.0 mm. Compared to the range values for 9C, 20C and 14B, the value for 14B (12.1 mm) exceeds that of 9C (11.3 mm) and 20C (9.8 mm). The lower located measurement point in the central block can thus include a greater range of relative displacements than a higher measurement point in a lateral block.

#### *Visualisation of relative displacements by time*

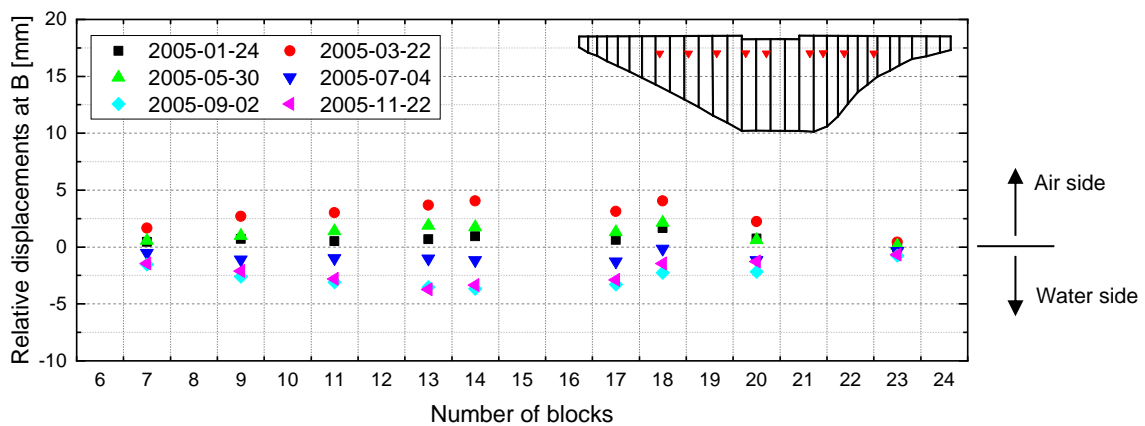
To view the relative displacement of the dam over time, the datasets in 2005 for every second month are displayed in Figure 3.21. Each symbol represents one relative displacement value of the corresponding horizontal block at a certain elevation. In each figure, the symbols with the same colour represent the relative displacements on an identical date, forming a bending line of the dam from a top view. The positive direction of displacements presents the direction to the air side.

Overall, the dam deformation states and displacements vary throughout the year. In Figure 3.21 (a), the red symbols (representing deformation in March), green symbols (representing deformation in May) and dark blue symbols (representing deformation in July) show that from March to July, the dam part at the elevation of suspension A deforms from downstream to upstream. The same tendency is observed for the dam part at the elevation of suspensions B or C. Only the amplitude of deformations range gradually increases with the increase of elevation, and suspension C in Figure 3.21 (c) presents the greatest deformation in this time period.

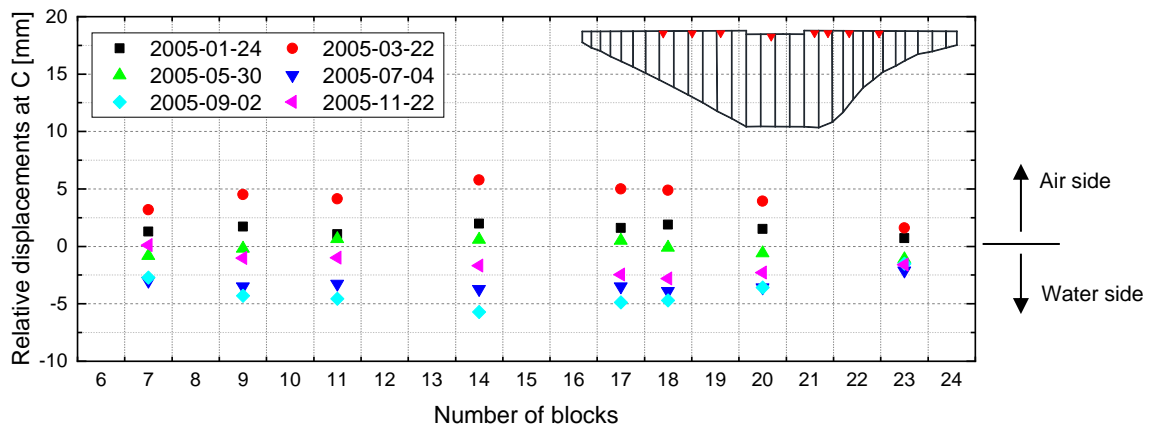




(a): Relative displacements at measure points of suspension A at elevation 390 m a.s.l.



(b): Relative displacements at measure points of suspension B at elevation 408.5 m a.s.l.



(c): Relative displacements for measure points of suspension C at elevation 390 m a.s.l.

Figure 3.21: Visual view of relative displacements in upstream-downstream direction by time in 2005

When comparing the blue symbols (representing deformation in September) and pink symbols (representing deformation in November) in Figure 3.21, it shows that at suspension A in November, the dam is further in the water side than in September; at suspension B, the dam has slightly returned to the air side in November compared to September; and at suspension C in September, the dam is further in the water side compared to November, which differs from the deformation at suspension A. This demonstrates that for different dam elevations, the

variations of deformation are not in phase. It means for the same time point, the dam crown reaches the furthest position towards the air or water sides, while the lower part of the dam may still not reach the farthest position.

#### *Comparison of measured relative displacements at comparable locations*

The time series of relative displacement at measuring points of 14C, 14B and 14A are displayed in Figure 3.22. Firstly, an annual cyclical variation for each location can be characterised. Secondly, the higher point in the dam processes a greater amplitude and peak value in the variation curve. Thirdly, the largest positive displacements for measurement point 14C in each year exist around the 1<sup>st</sup> of March while the largest negative ones occur around the 1<sup>st</sup> of September. Fourthly, phase shifts can be detected for different points, and the variation of relative displacements for lower points lag behind higher points.

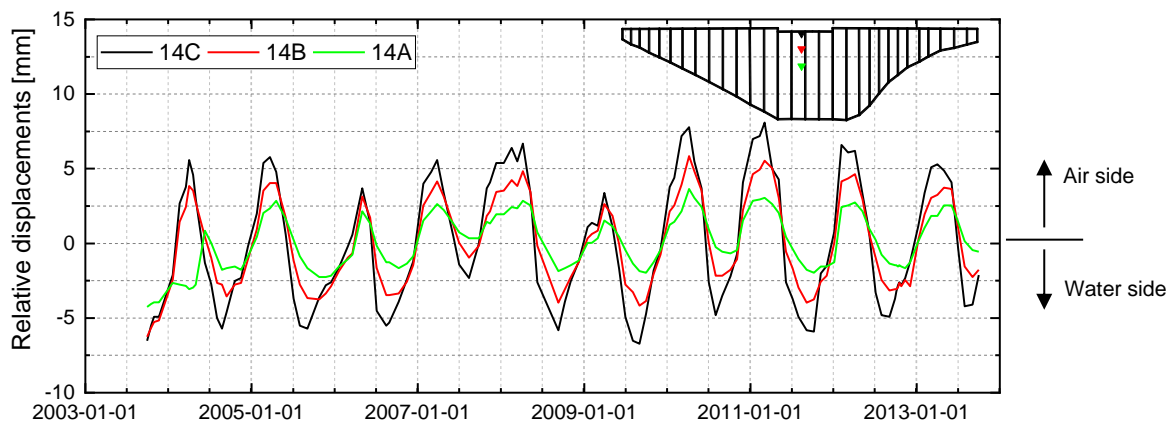


Figure 3.22: Time series of displacements in upstream-downstream direction at several comparable locations

#### *Measured displacements at dam base*

Figure 3.23 shows the time series and a box plot of relative displacements in the upstream-downstream direction at the dam base. Measured using a floating plumb wire at the bottom of block 13, the values present displacements relative to the position 35 m deep in the bedrock.

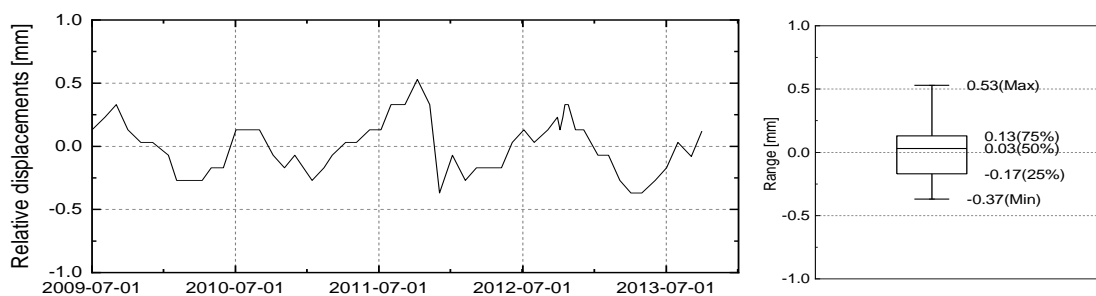


Figure 3.23: Time series of relative displacement at bottom of block 13 from floating plumb wire in upstream-downstream direction

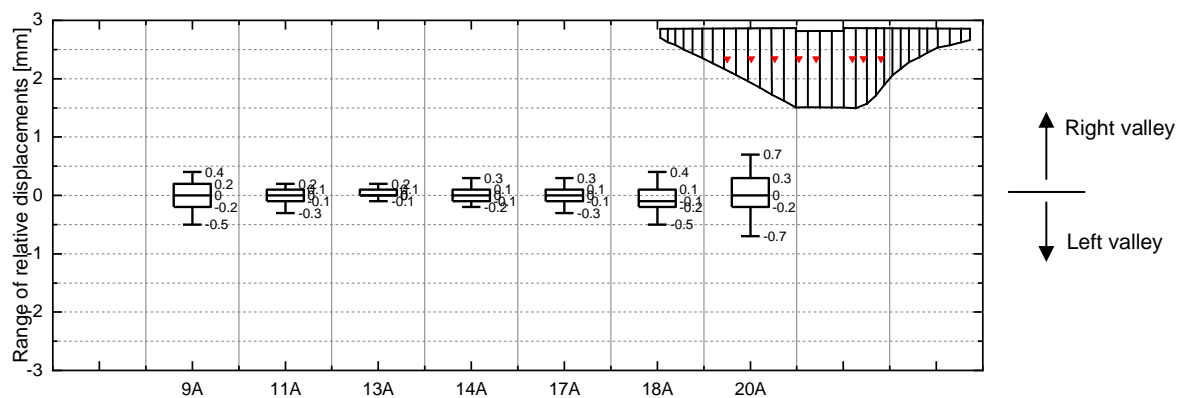
The values fall in a narrow range from -0.37 mm to 0.53 mm, 50% of which stay between -0.17 mm and 0.13 mm. This tiny variation means that the dam base at central blocks is quasi fixed in the upstream-downstream direction under the ambient environmental conditions.

### 3.4.3 Horizontal displacement in longitudinal direction

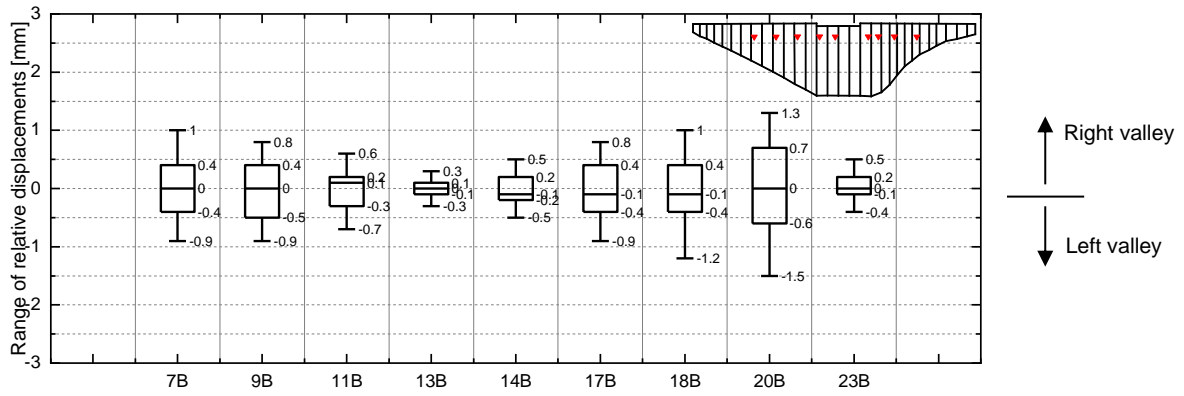
#### *Ranges of the relative displacement*

The ranges of recorded relative displacements at suspensions C, B and A in the longitudinal direction along the dam axis are displayed in Figure 3.24. The positive direction of the longitudinal direction along the dam axis is to the right valley at the dam site from the upstream view. As shown in Figure 3.24, like the upstream-downstream direction, the amplitude of the displacement variation at the measured locations of suspension C generally exceeds that of B and A for the same block. When comparing the amplitude of variations at the same height, the range tends to be larger at lateral rather than central blocks (except for block 23) due to the displacement accumulation in longitudinal direction from the centre block.

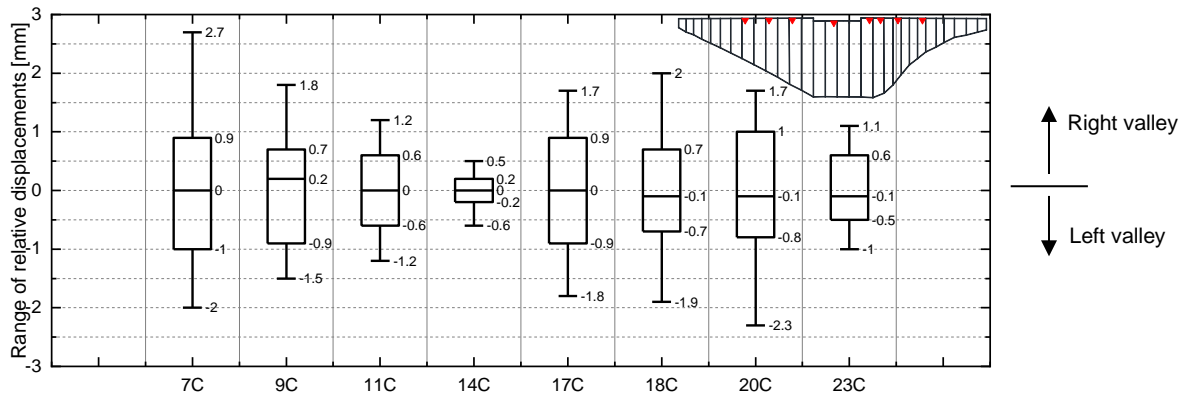
Figure 3.24 shows that the largest range of relative lateral displacements is 1.4 mm at 20A among the measurement points at suspension A. For those at suspension B, the greatest range of relative displacements is measurement point 20B with a value of 2.8 mm; and for the measuring points at suspension C, the greatest variation exists at 7C with a value of 4.7 mm. Regarding the variation of relative displacements in the upstream-downstream direction, the most significant point is 14C with a value of 14.8 mm, but its variation of relative displacements in the longitudinal direction accounts for only 1.1 mm, which is much smaller than the value in the upstream-downstream direction. Moreover, the largest variation 4.7 mm in the longitudinal direction is much smaller than the displacement variation in the upstream-downstream direction at the identical point 7C, which reaches the value of 8.0 mm. The upstream-downstream direction is thus more significant compared to the longitudinal direction regarding the ranges of relative displacements.



(a): Range of measured relative displacements of suspension A at elevation 390 m a.s.l.



(b): Range of measured relative displacements of suspension B at elevation 408.5 m a.s.l.



(c): Range of measured relative displacements of suspension C at elevation 426.4 m a.s.l.

Figure 3.24: Ranges of measured relative displacements to mean value in longitudinal direction

*Comparison of displacements in several comparable locations*

In purpose of illustrating the displacements in the longitudinal direction at quasi-symmetrical positions of the dam, the relative displacements at blocks 9 and 20 are compared in Figure 3.25 at three elevations.

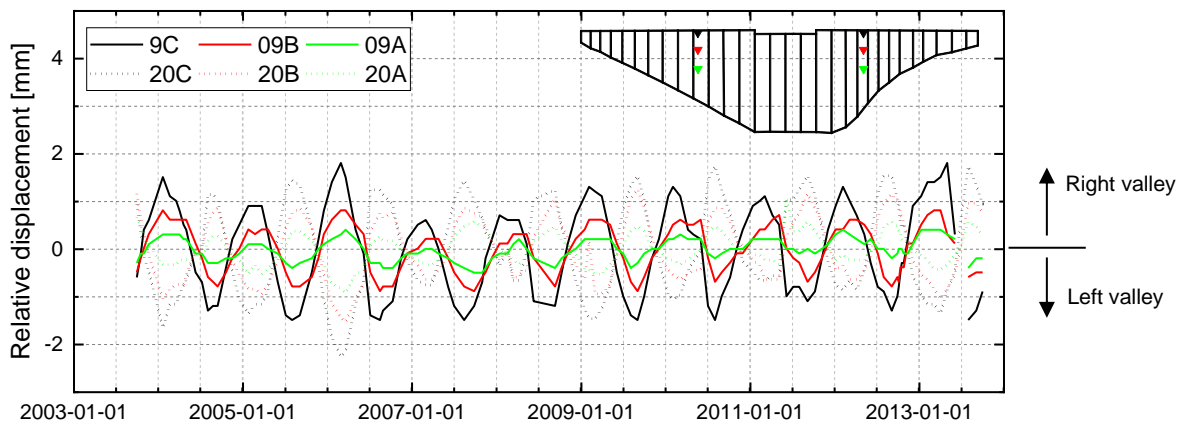


Figure 3.25: Time series of relative displacements at blocks 9 and 20 in longitudinal direction

For each displacement history, annually cyclical variations can be observed. The displacements at blocks 9 and 20 at the same elevation have almost the same large amplitude yet different directions. This means that from the water-side view for the left- and right-located blocks at quasi-symmetrical positions, the tendencies of displacements change are consistent towards or away from the centre block at the same time. When comparing the relative displacements at the same block at elevations C, B and A, the amplitudes of relative displacement decrease with decreasing elevation and the lower point has slight phase lag compared to the higher point. When comparing different elevations at the same block, the results in the longitudinal direction are similar with the movements in the upstream-downstream direction.

#### *Comparison of measured displacements, water level and air temperature*

As presented in Section 3.3, the water levels and air temperatures at the site in past years present an annual cycle, and the displacements in response demonstrate also annual characteristics. To investigate the relationship between the external loads and displacement responses, Figure 3.26 shows the time series of water level, air temperature and relative displacements at point 11C for comparison.

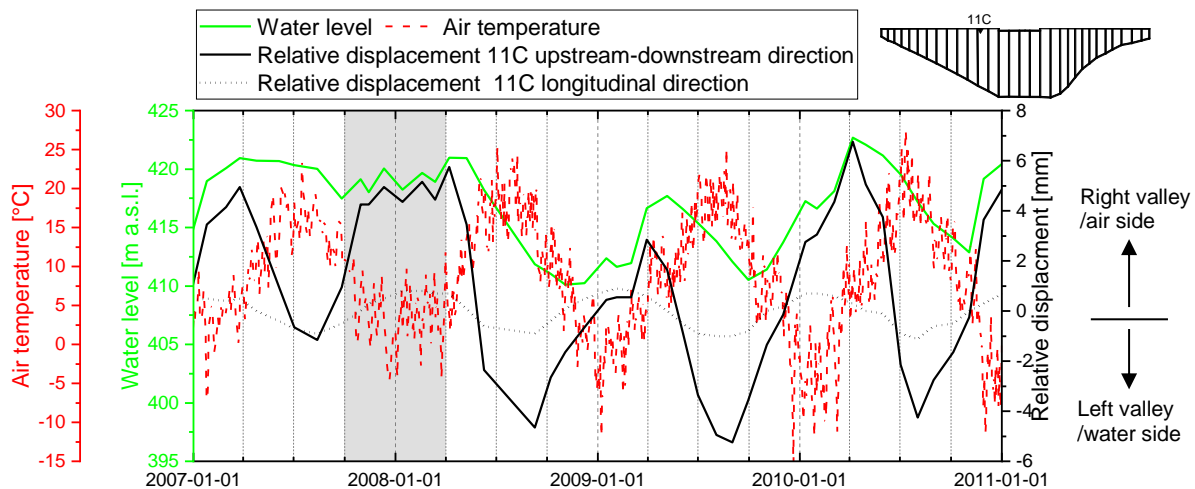


Figure 3.26: Comparison of air temperature, water level and relative displacement

Figure 3.26 presents annual variation in certain ranges, and here the values of the range are not in focus but rather the variation's tendency. Despite difference in variation of ambient temperature and water level in different years, the relative displacement in longitudinal direction present unchanged variation. Regarding the upstream-downstream direction, the relative displacement at 11C shows corresponding consequence with an abnormality of water level during the period from September 2007 to March 2008. However, it is difficult to describe the single or simultaneous effects on dam displacement due to changes in water level and ambient temperature. Therefore, the relationship between external loads and corresponding displacements cannot be achieved via graphical visualisation of the monitoring data. In the

following chapters, further investigation based on numerical simulation is conducted to interpret the relationship between dam displacements and the variation of water level / ambient temperature.

Considering that, firstly, the characteristics presented by the displacement distribution in longitudinal direction can be represented by those in the upstream-downstream direction. Secondly, the amplitude variation of horizontal displacement in longitudinal direction is slight and presents unchanged variation under different combinations of ambient temperature and water level. Thirdly, according to some studies (Venturelli, 1992; Boberg & Holm, 2012; Tatin et al., 2015; Chopra & Chakrabarti, 1972; Andersson & Hagberg, 2018; Varagilal, 2018), straight concrete gravity dams are usually modelled using a planar model to investigate the vertical displacement (settlement) and horizontal displacement in the upstream-downstream direction via numerical simulation. Hence, the displacements for different blocks and elevations are primarily analysed in the upstream-downstream direction to further model the deformation behaviour of the studied concrete gravity dam.

### 3.5 Conclusions

This chapter describes the monitoring of Rappbode Dam, including the monitoring system and monitoring data. To achieve a view of the deformation behaviour of Rappbode Dam and its ambient environmental conditions, graphical visualisation of the monitoring data on the dam site is presented, including the external loads (air temperature, water temperature, water level and uplift pressure) and responses (concrete temperature and displacements). The yearly cyclic loads and structural responses are thereby observed.

The air temperature varies throughout the year, and the water temperature presents seasonal cyclic characteristics. At one time point, the water body in the lower half of the reservoir presents the same temperature as the upper part of the water is influenced by the ambient air temperature. The uplift pressure at the dam base remains directly proportional to the reservoir's water level. The responses of concrete temperature vary slightly in the lower, thicker part of the dam, while a yearly cyclic variation is observed in the upper part. The phase shift of temperature variation for one location inside the dam relative to the air temperature increases with the depth of this location from the concrete face exposed to air.

The displacements in the upstream-downstream direction at measuring points illustrate a cyclic variation with different amplitudes at different elevations and blocks. The points located at higher elevation and in central blocks present greater ranges of displacement variation in the upstream-downstream direction throughout one year. There is a phase shift between the displacement variations at different elevations at the same block. The displacements at the dam base present a range of less than 1 mm in the upstream-downstream direction over the

---

years. The deformation in the upstream-downstream direction of a concrete gravity dam is more significant than the longitudinal deformation concerning the variation amplitudes. Phase shifts are obtained when comparing the time series between displacements, water level and air temperature. The relationship between water level/temperature and displacement cannot be detected via graphical visualisation of the monitoring data, which requires interpretation in the numerical simulation.

## 4. Functional FE model of Rappbode Dam

In the numerical simulation of this dam's deformation response, a functional FE model is required to present the structural geometry characteristics, conduct transient thermal and structural analyses and deliver convergent results. This chapter firstly presents the basis to assess the deformation of a dam via structural analysis and time-varying temperature distribution in thermal analysis in numerical modelling. Then, the geometry model of this dam is described in ANSYS along with the material behaviour assumptions. Thirdly, taking the simulation of hydrostatic pressure and transient thermal phenomena into consideration, results of temperature and displacement are investigated to determine the reasonable and plausible mesh for the functional FE model of Rappbode Dam.

### 4.1 Thermal analysis and structural analysis in FE modelling

This section firstly introduces principles for FE thermal and structural analyses in ANSYS. The external loads must then be considered to simulate the deformation behaviour of Rappbode Dam, and the corresponding simulation method is presented. Thirdly, the procedure of conducting a transient thermal analysis is described.

#### 4.1.1 Basis of thermal /structural analysis in ANSYS

The process of a typical analysis in ANSYS involves three steps: building the model; applying loads and executing the solution; and reviewing the results. This process is listed in Table 4.1, where the contents in one row presents the general tasks and corresponding processor for one step.

Table 4.1: Steps of a FE analysis in ANSYS

Step	Contents or tasks	Processor
Building the model	Definition of <ul style="list-style-type: none"> <li>➤ Geometry</li> <li>➤ Material properties</li> <li>➤ Mesh</li> </ul>	Preprocessor
Applying loads and executing the solution	Specification of <ul style="list-style-type: none"> <li>➤ Boundary conditions</li> <li>➤ Analysis type</li> <li>➤ Initiating the solution</li> </ul>	Solution
Reviewing the results	Results <ul style="list-style-type: none"> <li>➤ POST1</li> <li>➤ POST26</li> </ul>	Postprocessor



In the first step, the preprocessor is used to specify the model geometry, material properties, element types and mesh generation to build a FE model. The second step is done in solution processor, in which load and load step options are specified as well as analysis options to initiate the FE solution. Finally, the results can be reviewed using postprocessors POST1 or POST26. POST1 is a general postprocessor by which results are reviewed at one timepoint over the whole model or selected portion of the model; while in the time-history postprocessor POST26, results are reviewed at specific points in the model over all time steps in the calculation (ANSYS, 2013).

In ANSYS, two kinds of thermal analyses are supported: steady-state thermal analysis is used to determine the temperature distribution under steady-state loading conditions without considering the time-varying characteristics of heat storage effects over a time period; transient thermal analysis determines the temperature distribution under conditions that vary over a time period (ANSYS, 2005). When simulating the temperature distribution within the dam under varied ambient temperatures, the temperature distribution varies over time, hence transient thermal analysis is required to acquire a time-dependent temperature distribution within the dam. The computed temperature distribution at one time point can be obtained using the POST1 postprocessor, while the variation of the temperature at one point can be obtained using the POST26 postprocessor.

Thermal-structural coupled analysis occurs either by direct or load-transfer coupling (Qin, 2008). Direct coupling involves a single analysis using a coupled-field element type containing all requisite degrees of freedom. The load-transfer coupling involves two analyses belonging to different fields, and the results obtained from one analysis can serve as loads for another. The load-transfer method is more efficient and flexible for coupling situations that do not show a high degree of nonlinear interaction, because the two analyses are performed independently and nodal temperatures from any load step or time-point in the thermal analysis can be specified as loads for the structural analysis (ANSYS, 2005(a)). In this thesis, the more efficient load transfer method is adopted for the coupled analysis.

#### 4.1.2 Specification of external loads in deformation analysis

The water level and temperature are demonstrated to be the most significant factors influencing the deformation behaviour of an operational concrete dam, while the deformation influence from uplift pressure at the dam base depends on the dam's structural characteristics (Fahland, 2004). According to DIN 19700-11 (2004), the influence factors affecting the deformation behaviour of an operational gravity dam are divided into three groups depending on their duration and frequency: permanent or repeating loads, rare or time-limited loads and extraordinary loads.

As described in Section 3.3, the water level, uplift pressure, ambient temperature present cyclic characteristics. The Harz region is not an earthquake-prone zone (Tyagunov et al., 2006). Investigating the deformation behaviour of Rappbode Dam considers thus the hydrostatic pressure at upstream, uplift pressure at dam base, ambient air temperature, water temperature and self-weight, each of which belongs to either permanent or repeating load. The influence of time-limited or extraordinary effects such as wind pressure, ice, traffic loads, earthquake and so on are excluded from the numerical modelling.

The gravity dam is generally assumed to be leak proof (Rißler, 1998), and the loads related to water include the hydrostatic pressure at the upstream face from water thrust in the reservoir and the uplift pressure due to seepage water at the dam's base, as shown in Figure 3.9. This thesis does not analyse seepage problems such as seepage rate and exit gradient in dams and underlying bedrock. In the simulation, the recorded data of uplift pressure provide stress boundary specified at the base of the dam model. At the interface of the dam base and foundation, contact elements are created to enable specifying the uplift pressure. The horizontal hydrostatic pressure is applied to the upstream face of the dam as a stress boundary condition by assuming a linearly increasing boundary stress on the dam from the surface of the water table to the dam heel with a slope of water-specific gravity.

The self-weight of the dam-foundation system is defined by input gravitational acceleration in the vertical direction for the whole structure. The influence of self-weight on the deformation behaviour can be presented using the absolute values obtained via simulation, where specifying self-weight is needed to prevent the dam from floating up under the uplift pressure at the dam base. It should be mentioned that when investigating the relative displacements, the permanent effect from self-weight is not included and only the periodically changing effects are presented.

The temperature induced deformation is caused by the differences between two temperature values, one of which is the reference temperature indicating the temperature at which strain does not result from thermal expansion or contraction. Regarding the thermal displacement variation during a time period, different reference temperatures influence the computed absolute displacement but not the relative displacement. In this thesis, a reference temperature of 5 °C is specified. In the thermal deformation analysis, transient thermal analysis is firstly conducted to obtain the temperature distribution, specifically the temperature at each node of the FE model; in the structural analysis, the temperature distribution is then applied on each node to acquire the thermal displacement. The emphasis in this coupled analysis is the determination of the time-varying temperature distribution of the dam interior due to the variation of ambient temperature via the transient thermal analysis.

### 4.1.3 Transient thermal analysis

In this section, the fundamentals for heat flow conduction are introduced firstly, including the differential equation and conditions, and then the ambient boundary conditions for Rappbode Dam in the transient thermal analysis is presented.

#### *Differential equation of heat conduction*

According to the law of conservation of energy, isotropic material's heat conduction is carried out through the classical Fourier equation as follows (Ozisik, 1993):

$$\lambda \left( \frac{\partial^2 T}{\partial x^2} + \frac{\partial^2 T}{\partial y^2} + \frac{\partial^2 T}{\partial z^2} \right) = c \cdot \rho \frac{\partial T}{\partial \tau} + Q \quad (4.1)$$

where  $\lambda$  is the thermal conductivity,  $c$  is the specific heat,  $\rho$  is the material density,  $T$  is the temperature at the point  $(x, y, z)$ ,  $\tau$  is time,  $Q$  is the heat source and  $\frac{\partial T}{\partial \tau}$  presents the heat flow per unit of time.

For massive concrete structures such as dams, there are no heat sources inside, therefore in the heat equation above  $Q = 0$ , Equation (4.1) becomes

$$\frac{\partial T}{\partial \tau} = k \left( \frac{\partial^2 T}{\partial x^2} + \frac{\partial^2 T}{\partial y^2} + \frac{\partial^2 T}{\partial z^2} \right) \quad (4.2)$$

$$k = \frac{\lambda}{c \cdot \rho} \quad (4.3)$$

Where  $k$  is a real coefficient called the diffusivity of the medium.

However, numerous solutions can satisfy the heat conduction equation in Equation (4.2) without certain conditions. To determine the required temperature field, Equation (4.2) must be solved under appropriate boundary and initial conditions (for the time-dependent problem). The initial condition represents the temperature field in the medium at the beginning timepoint ( $\tau=0$ ), and the boundary condition presents the temperature or heat flow at the region's boundaries (Ozisik, 1993).

#### *Initial Condition*

With  $\tau$  as time, at the origin of the time coordinate, the temperature field is a given function  $T_0(x, y, z)$ , i.e.

when  $\tau = 0$ ,

$$T(x, y, z, 0) = T_0(x, y, z) \quad (4.4)$$

The determination of the initial temperature distribution state in the thermal analysis for Rappbode is investigated in Section 5.1.

### *Boundary Conditions*

The boundary conditions can be described in the following types for mass concrete, including prescribed surface temperature, heat transfer on the surface and contact surface between two solids (Zhu, 2014). Each boundary case is listed with the computation equation below.

#### (a) Prescribed surface temperature

The surface temperature of the concrete is prescribed as follows:

$$T_s(\tau) = f(\tau) \quad (4.5)$$

Where  $f(\tau)$  is the surface temperature and is a function of time.

#### (b) Convective heat transfer on the surface

The heat flux through the concrete surface is proportional to the difference between the concrete surface temperature and ambient air temperature, namely on the surface:

$$-\lambda \frac{\partial T}{\partial n} = \beta(T_s - T_a) \quad (4.6)$$

Where  $\beta$  is the surface conductance,  $T$  is the surface temperature of concrete and  $T_a$  is the air temperature.

#### (c) Contact surface between two different solids

The temperature would be continuous on the surface, then the boundary condition is:

$$\left. \begin{array}{l} T_1 = T_2 \\ \lambda_1 \frac{\partial T_1}{\partial n} = \lambda_2 \frac{\partial T_2}{\partial n} \end{array} \right\} \quad (4.7)$$

where  $\lambda_1$  and  $\lambda_2$  represent the conductivities of the two contacted solids respectively.  $T_1$  and  $T_2$  are the temperatures of the two contacted solids.

### *Specification of boundary ambient temperature in transient thermal analysis*

The boundary conditions of a concrete gravity dam regard three parts: the water-concrete contact boundary, ground-concrete contact boundary and air-concrete contact boundary (Léger et al., 1993).

For the ground-concrete contact boundary, the temperature of the water at the basin floor of the reservoir approximately remains the same and the foundation rock on the air side is mostly

covered with earth and has a strong vegetation. Figure 3.18 shows that based on the measured concrete temperature at the lower position of the dam, the temperatures inside the dam close to the ground are nearly constant, especially those at T17-T20 with medians around 5.2 °C. Hence, it is more efficient to calibrate the time-varying temperature distribution within the dam body when setting the constant temperature value (5.2 °C) at the ground-concrete contact boundary. The foundation modelling is ignored in the thermal analysis.

The water-concrete contact boundary belongs to the first boundary condition. Based on the analysis of the air-concrete contact boundary in Appendix B, when the yearly periodic variations of ambient air are considered, the air-concrete boundary can be treated as the first kind of boundary condition (Zhu, 2014).

Regarding the water and air temperatures, Venturelli (1992), Léger (1993) and Daoud et al. (1997) modelled the water temperature variation in the deep reservoir using a simplified profile, Zhu (1997) suggested formulas to predict the variation in water temperature at various depths for concrete dams. Tatin et al. (2015) adopted a theoretical model to define the water temperature, while Daoud et al. (1997) and Sheibany et al. (2004) approximated the air temperature using sinusoidal functions.

In this thesis however, the recorded air and water temperature in the reservoir are considered and specified to the boundary in the transient thermal analysis to avoid potential error in the estimated formulas. In terms of the load step, in this thesis, the load step of one day is adopted, and diurnal temperature variation is not taken into consideration. One temperature value for each day represents the day's mean temperature. Because no heat source inside the dam is specified, the temperature variations under specified initial uniform temperatures and time-varying ambient temperatures are simulated under the assumption that the development of hydration heat has dissipated.

Based on the analysis above, the ambient temperature boundary of the dam is specified as shown in Figure 4.1, and the recorded air temperature is specified on the air-concrete contact boundary of the dam. Because the lower part of the reservoir presents similar temperatures values for different elevations and the upper-part temperature changes with elevation, the temperature at the water side is applied with seven different layers for the upper part of the upstream face but one layer for the bottom part of the upstream face, as depicted in Figure 4.1. The different layers are defined based on the measurements that fall within a narrow height range, where the recorded values had a small difference. The corresponding defined elevations for each layer are listed in Table C.1 in Appendix C.

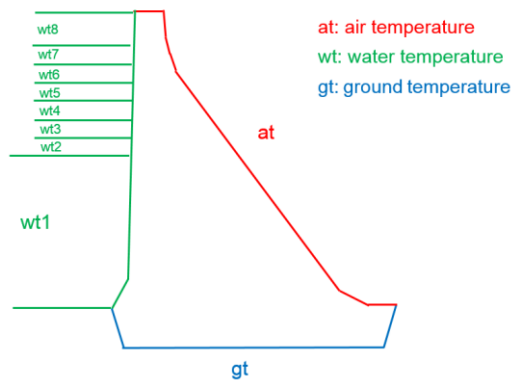


Figure 4.1: Diagram of cross-section view of boundary temperature specification

## 4.2 Geometry model and material behaviours of dam-foundation system

### 4.2.1 Geometry model

For gravity dams, the displacement in one section or at one point in the dam can be investigated using a planar model (Boberg et al., 2012; Léger et al., 1993; Varagilal, 2018); however, one planar model is insufficient to cover the displacement distribution in different blocks with different elevations. In addition, the mutual effects between adjacent blocks and constraints induced by the underling bedrock and lateral valley are not considered in a planar model. Hence, a three-dimensional model is used to investigate the displacement distribution in the deformation simulation of Rappbode Dam.

According to DIN 19700-11 (2004), underground or the soil/rock under the dam and body of the dam act as a whole structure and are thus modelled in the FE model together. The modelled foundation portion is dimensioned in such a way that the influences due to water-level fluctuations and temperature changes faded away as far as the model boundaries (Hintner, 2008). For dam structures, this boundary is recommended to be set at the position with a distance that is one to one-and-a-half times the reservoir depth (Khosravi et al., 2013; Zhang et al., 2009). To generate the geometrical foundation model, considering the reservoir depth of 89 m, the thickness of the modelled rock layer under the base of the dam and the width of bedrock on both sides of the river as well as the bedrock width along the river are set to 100 m, i.e., there is a 100 m extension in each direction where bedrock exists. The geometry of the valley is idealised according to the profile of the bedrock under the dam. Figure 4.2 illustrates the idealised three-dimensional solid geometrical model of the dam-foundation system and provides a full-scale geometrical model of the dam, which is about 415 m in length (longitudinal direction), 81 m in width at the bottom (upstream-downstream direction) and 106 m in height (z-direction). The axis along the dam's crown is defined as the x-axis, where the positive direction is from left valley to right valley from a water-side view; the direction along the river is y-axis, where the positive direction is from upstream to downstream face; and the

elevation direction is the z-axis, where the positive direction is upward. The coordinates are in accordance with the coordinates of the monitoring system, and the foundation is fixed at the far end boundary with displacements constraints in x, y and z directions for analyses in this thesis.

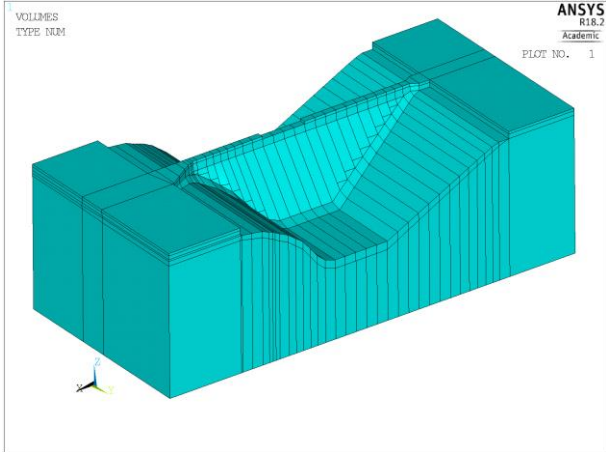


Figure 4.2: The solid geometrical model of the dam-foundation system from downstream view

4.2.2 Material behaviour

To perform transient thermal analysis for the time-varying temperature distribution and structural analysis for the deformation behaviour of dams in operational phase, the material parameters of the dam and foundation require specification. For the foundation, the parameters are defined based on the laboratory tests, while for the dam body, some assumptions are adopted for the material properties and an approach to their back analysis is described.

It should be mentioned that, in ANSYS, the unit depends on how the users define the input since there is no built-in unit in ANSYS itself. Table 4.2 lists the unit system used in this thesis, the International System of Unit.

Table 4.2: System of units used in analysis

Length	Mass	Time	Temperature	Stress	E modulus	Density
m	kg	s	K	Pa	Pa	kg/m <sup>3</sup>

In the case of Rappbode Dam for the foundation, four samples of drilling core from the bedrock were taken and tested in laboratory, and the mechanical parameters were reported (Popp, 2003). Because cracks or damage to bedrock are not included in this thesis, the bedrock is treated as a homogenous elastic material in this thesis. The mechanical parameters of the foundation are determined based on the values from tests in the report (Popp, 2003), and the

thermal-related parameters of the foundation are taken from the literature (Schneider, 2010) for normal clay shale, with the parameters' values listed in Table 4.3.

Table 4.3: Material parameters for the foundation of Rappbode Dam

Item	value
Elastic modulus (Pa)	5.298 e10
Poisson's ratio	0.125
Density (kg/m <sup>3</sup> )	2716
Thermal expansion (1/K)	6e-6
Specific heat J/ (kg·K)	1050

As for the material behaviour of the dam body, linear elastic material behaviour is assumed to investigate the dam's time-varying temperature distribution and deformation behaviour. The temperature dependence of concrete's thermal and mechanical properties is excluded from the framework of this thesis.

In this way the effective uniform material properties over the whole dam are used in this thesis to present the global material behaviour in the deformation behaviour analysis. This linear elastic hypothesis holds for undamaged structures; however, in damaged structures, cracks for example act as sources of nonlinearity. When cracks occur, the effective thermal expansion is enhanced, and the effective global elastic modulus is reduced using the approach presented herein.

The material parameters can be obtained through back analysis based on measured data widely used by engineering researchers (Zhou et al., 2011; Zheng et al., 2013; Sun et al., 2016). The effective material parameters in this thesis are back calculated as follows: the theoretical values from literature for the material parameters are taken as starting values; then, the values in the corresponding interval of each parameter are adopted to perform computations and the results are compared with the measured data to determine the most appropriate value as the effective value.

Equations (4.2) and (4.3) show that the quotient of heat capacity and thermal conductivity affect the temperature field calculation. Thus, it is reasonable to only consider the thermal conductivity in the parameter study and to set the heat capacity and density to be fixed values. For computing the displacement response in the mechanical analysis, the thermal expansion coefficient belongs to the critical material parameter for thermal displacement, and the elastic modulus is critical when considering the water-level fluctuation. The three above-mentioned critical parameters are determined via back analysis, while other parameters are set as fixed



values based on the literature. The fixed values are listed in Table 4.4, while the starting values and interval values of the three critical parameters are listed in Table 4.5 (Schneider, 2010; Verein Deutscher Zementwerke, 2002; DIN EN 206, 2016; Paschotta, 2017). Details about the back-analysis process are presented in Chapter 5.

Table 4.4: Material parameters of the concrete

Item	Value
Poisson's ratio	0.2
Density (kg/m <sup>3</sup> )	2500
Specific heat J/ (kg·K)	1050

Table 4.5: Starting values and interval values for the three critical parameters

Item	Starting values	Interval value in back analysis
Thermal conductivity (W/(m·K))	2	[1,4]
Thermal expansion coefficient (1/K)	9e-6	[5e-6, 14e-6]
Elastic modulus (Pa)	2.5e10	[1.5e10, 3.5e10]

### 4.3 Accuracy analysis of mesh elements for the dam body

Meshing is an essential part in numerical simulations, which influences the simulation's convergence, accuracy as well as speed. To achieve convergent and accurate results by simulating temperature distribution and deformation behaviour, meshing is investigated in thermal and structural analysis for the geometrical model of Rappbode Dam. Firstly, two different element types used for the meshing of solid three-dimensional model are introduced and compared in the deformation simulation. Then, the accuracy and convergency of different element sizes are investigated via thermal and structural analyses to determine an appropriate mesh of the FE model.

#### 4.3.1 Comparison of two different element types

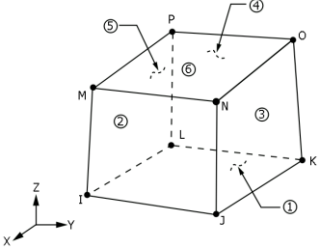
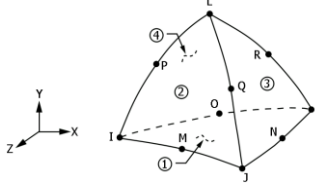
A three-dimensional geometrical model can be discretised by either hexahedral- or tetrahedral-shaped elements. Tetrahedral elements can be easily produced by automatic mesh generators compared to hexahedral elements, because although a general three-dimensional domain cannot always be decomposed into a collection of hexahedral-shaped elements, it can always be represented as an assembly of tetrahedral-shaped elements (Cifuentes et al., 1992).

Compared to linear elements, quadratic elements require additional computer resources and time for running large models. However, linear elements are stiffer than quadratic elements,

and thus the latter performs better for bending problems (Benzley et al., 1995). The elements library of ANSYS provides linear and quadratic hexahedral elements and quadratic tetrahedral elements. Linear tetrahedral elements do not provide satisfactory results, so the ANSYS element library lacks a defined element type with linear tetrahedral features. For the same analysis, results from a fine mesh of linear elements would provide better accuracy with less cost compared to a comparable coarse mesh of quadratic elements (ANSYS, 2004).

Two three-dimensional elements are selected to perform comparisons: the linear hexahedral (LH) element SOLID185 and quadratic tetrahedral (QT) element SOLID187, both of which are commonly used to discretise three-dimensional models. The goal is to investigate the performance of LH versus QT elements under the same loading conditions. The characteristics of the LH element SOLID185 and QT element SOLID187 are listed in Table 4.6. In their schematic diagram, the Arabic numbers present the faces of the solid element while the capital letters present the nodes. Despite the shape difference and node numbers, the capabilities of these two elements are similar and they have the same degrees of freedom at each node.

Table 4.6: Characteristics of element SOLID185 and SOLID187

	SOLID185	SOLID187
Element shape		
Nodes number	a 3-D, 8-node element	a 3-D, 10-node element
Capabilities	stress stiffening, creep, plasticity, large strain, large deflection, and swelling	stress stiffening, creep, plasticity, large strain, large deflection, and hyperelasticity
Degrees of freedom	At each node three: translations in the nodal x, y, and z directions	

The geometrical model of the foundation is not considered in comparing the two element types. An example of 75 m water level in the reservoir in the form of hydrostatic pressure on upstream face is adopted and specified on the model. The upstream view of the hydrostatic pressure applied on the upstream face is depicted in Figure 4.3 (a), presenting the maximum hydrostatic pressure at the bottom of the pressure area with a value of 0.735 MPa. In this analysis, an element size (edge of one element) of 10 m is defined for each element type to generate the mesh for the FE model. The boundary constraints on translation in x, y and z directions are

specified at the dam base. The material properties for this analysis adopt the values in Table 4.4 and starting values in Table 4.5, and the units used in this calculation are shown in Table 4.2.

For the difference between the LH and QT elements, the stress contours are taken to show the results. The upstream views of the stresses in the upstream-downstream direction are shown in Figure 4.3 (b) and (c), which depicts that, for both models, the compressive stresses tend to gradually increase from the top to the bottom of the dam. With the same element size however, the compressive stress distribution in the hydrostatic pressure area from the LH-element-discretised model presents better continuity and is smoother than that from the QT-element-discretised model. By decreasing the element edge or increasing the density of the mesh, the performance of the QT element is not improved. Hence, the LH element is selected to generate mesh for the FE model of Rappbode Dam.

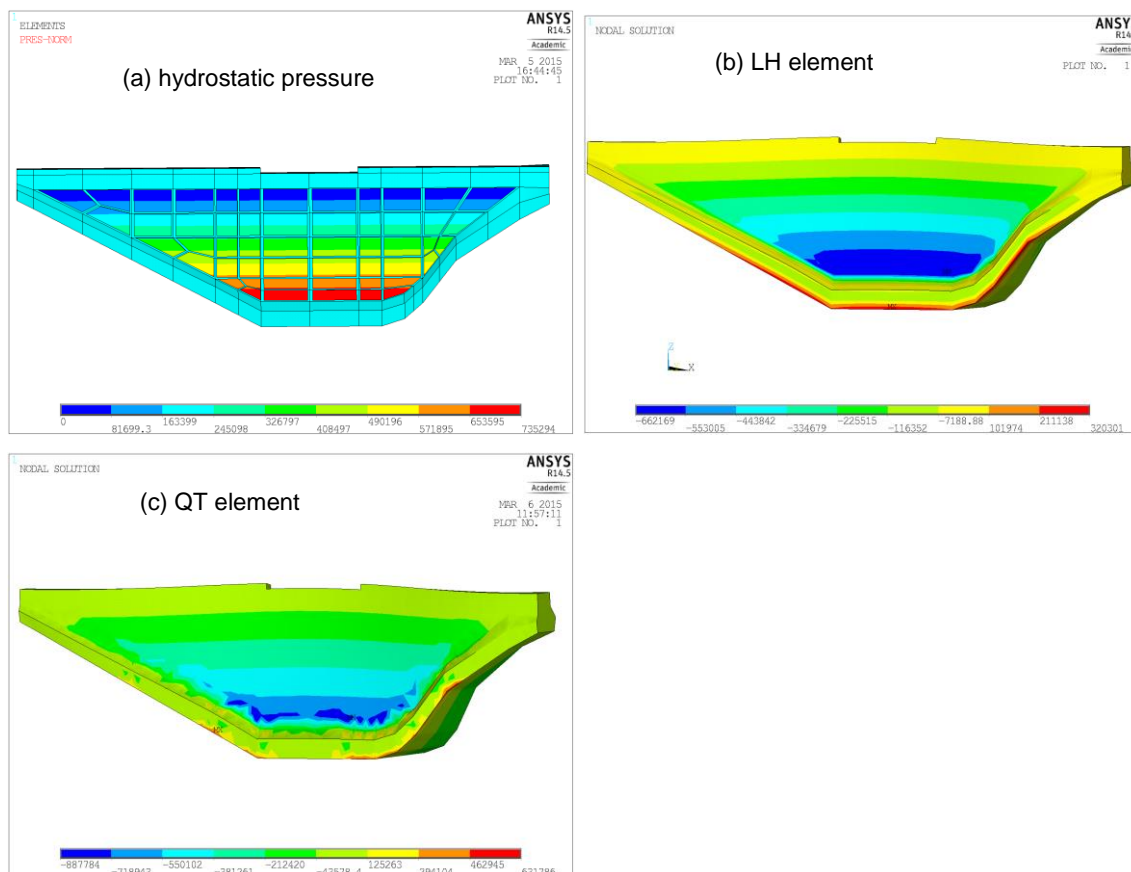


Figure 4.3: Upstream view of (a) applied hydrostatic pressure; (b) stress results from LH element; (c) stress results from QT element in upstream-downstream direction in ANSYS

#### 4.3.2 Analysis of mesh density under the hydrostatic pressure

The mesh densities are analysed by specifying different element sizes to the geometrical model of the dam in the simulations and investigating the convergency of the results from the structural and thermal analyses, including the temperatures, displacements and stresses at

certain representative points at different dam heights and depths from the surface. Theoretically, convergent curves should be obtained for each type of results at one location, i.e., if the mesh is sufficiently fine, the results from models with different element sizes convergent to a value. Figure 4.4 depicts the FE model with different element sizes, each of which has a corresponding number of nodes. The total number of nodes defined with different element sizes is shown in Figure 4.5, which reveals that the number of nodes increases with decreasing element size. When the element size decreased from 50 m to 6 m, the number of nodes increased stepwise. When the element size is larger, the mesh is coarser; the finer the mesh, the greater the stiffness matrix of the whole model and longer the calculation time. The focus is on the behaviour of the dam body, and thus the mesh density analysis is conducted on the model of dam body.

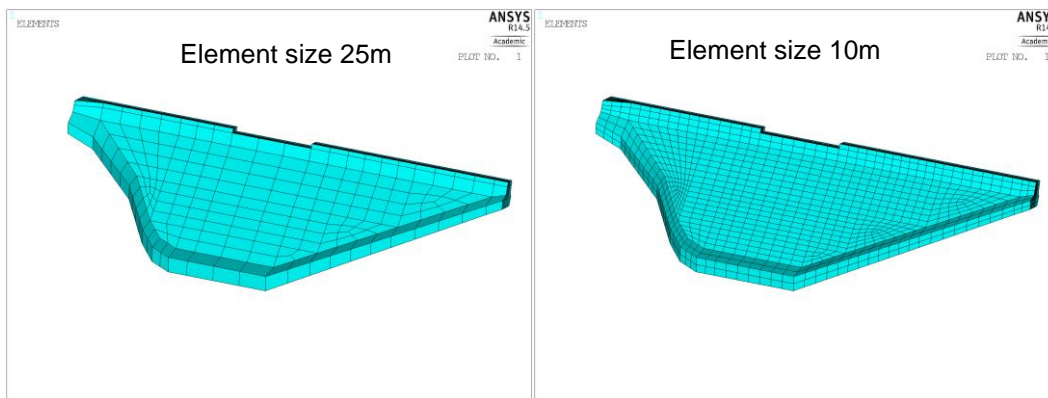


Figure 4.4: Visualisation of the FE model of the dam with different element sizes

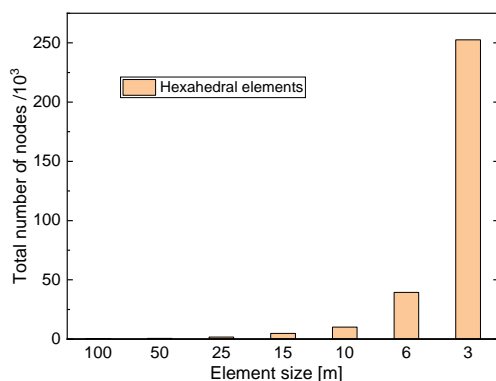


Figure 4.5: Number of nodes defined with different element sizes

Under the load case of hydrostatic pressure, structural analysis is conducted for different FE models with different element sizes. The accuracy analysis under hydrostatic pressure is then conducted by comparing the computed results at certain representative points, whose locations in the dam are shown by Figure 4.6. There are five points at the water side located at different elevations and comparable transverse sections, all belonging to Plane 1 (shown in cross section view in Figure 4.6) which is 4.5 m deep and lies parallel with the upstream face that specified with hydrostatic pressure. There are also two points at the downstream side.

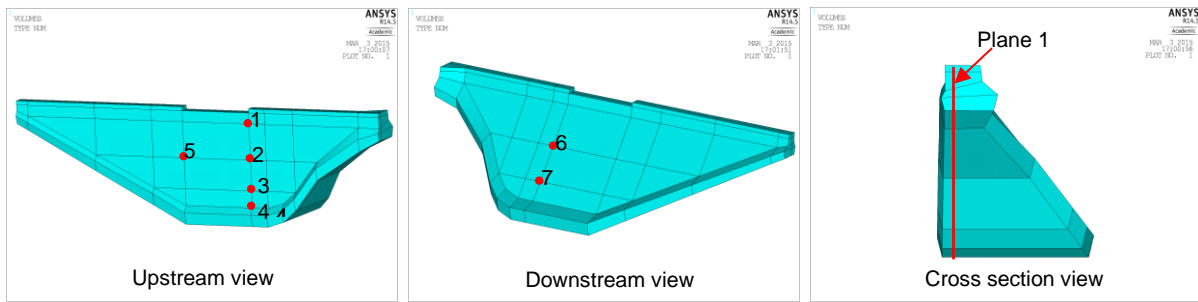


Figure 4.6: Display of the locations of the points for mesh density analysis under hydrostatic pressures

The values of the displacements and stresses in the upstream-downstream direction resulting from hydrostatic pressure at the selected points (as shown in Figure 4.6) are chosen to draw the convergent curves, as shown in Figure 4.7. A convergent curve is observed at each point, and the results of displacements are already convergent with an element size of 25 m; however, when the element size decrease to 10 m, both displacements and stresses remain steady and show a plain convergent feature for all selected points. The FE model with a global element size of 10 m can thus satisfy the accuracy requirements for hydrostatic pressure calculation.

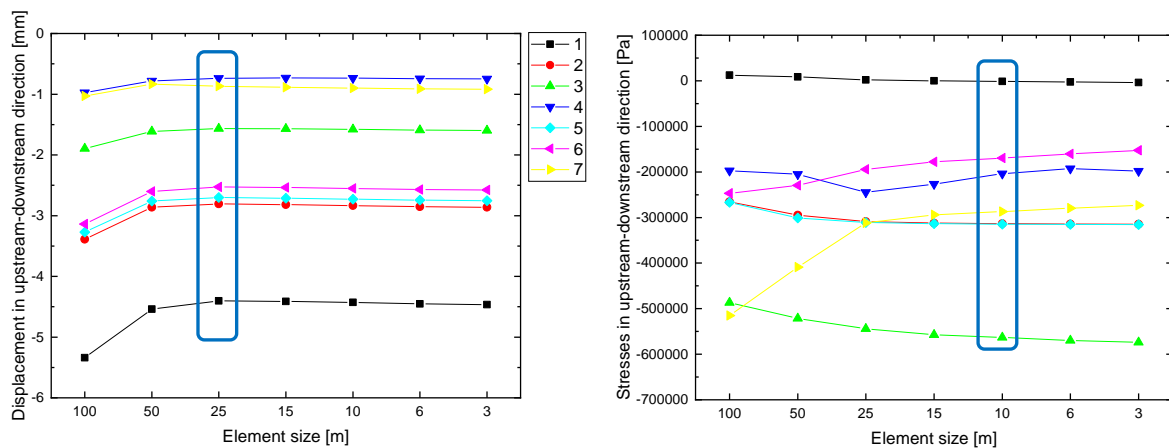


Figure 4.7: Convergence results of hydrostatic pressure computation

### 4.3.3 Analysis of mesh density under thermal load

Thermal-structural coupled analysis investigates the model accuracy with different mesh densities under ambient temperature conditions. For the thermal analysis, the results from both the transient- and steady-state thermal analyses are considered. The assumed boundary temperature for the mesh accuracy analysis is shown in Figure 4.8 with a cross-section view. The three parts of the exposed boundary are assumed as constant values to investigate the variation of temperature distribution inside the dam by time. An initial condition of 10 °C is specified for all the nodes of the dam model.

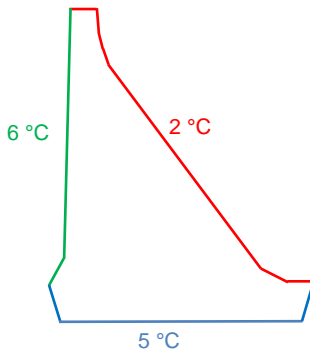


Figure 4.8: Diagram of assumed boundary temperatures for mesh density analysis

Transient thermal analysis is conducted to investigate the temperature distribution inside the dam from models with different element sizes. In this transient analysis, the temperature distributions are captured at different timepoints in the calculation period. Figure 4.9 displays the dam's temperature distribution at the timepoint of the 10<sup>th</sup> day in different FE models with different element sizes. To provide a clear view of the temperature field inside the dam, only half of the dam is displayed.

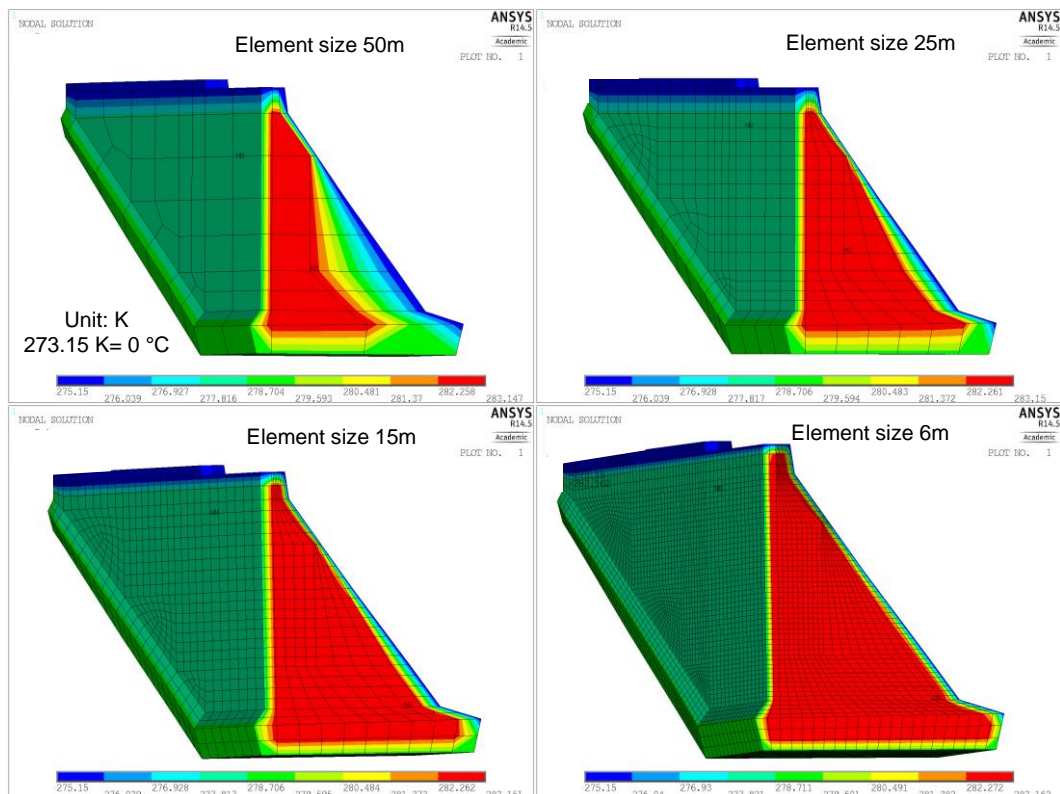


Figure 4.9: View of the temperature distribution inside the dam at timepoint of 10<sup>th</sup> day

Comparing these graphics in Figure 4.9, it is found that, at the exposed faces of the dam, the temperature equals the specified boundary temperature for the models with different element sizes, while the temperature distributions inside show great differences. Higher temperature gradients occur in the vicinity of the exposed surface of the dam, and the temperatures should be theoretically similar for locations at the certain same depth from the exposed face of the

dam. The first graphic with the element size of 50 m, presenting a highly coarse mesh, shows an unacceptable temperature distribution near the air-exposed surface. With the decrease of the element size, the model delivers better results of temperature distribution, because the finer mesh, the higher level of model accuracy. The temperature contour in the vicinity of the face exposed to air is parallel to the downstream, as depicted in the last graphic with the element size of 6 m, where maxima element edge in this vicinity reaches 3 m. This means that meshes with a 3 m element edge in this area can satisfy the accuracy request.

To eliminate the time effect on the thermal and structural responses, results from the steady-state analysis are analysed. The results of the temperatures, displacements and stresses in the upstream-downstream direction from the steady-state thermal analysis are depicted in Figure 4.10, and the locations of the points are depicted in Figure 4.11. The point groups 'a' and 'b' are nearly symmetrically located in the geometrical model of the dam, which makes it comparable while checking the calculation values at corresponding points. The perpendicular distances of these points to the exposed face of the dam are listed in Table D.1 (Appendix D). For the element size 10 m, all results listed at the representative points are convergent, and thus for thermal or structural analyses under thermal loads, the FE model with a global element size of 10 m can deliver satisfactory results.

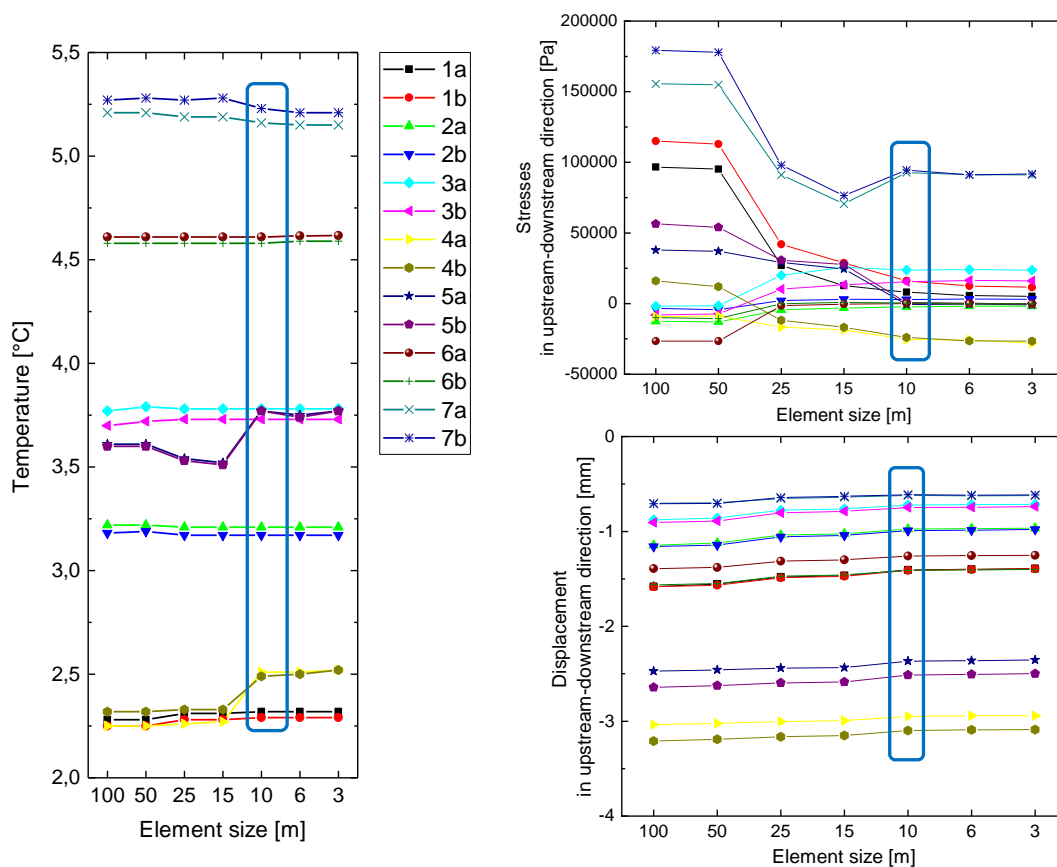


Figure 4.10: Convergent curves of transient thermal analysis results



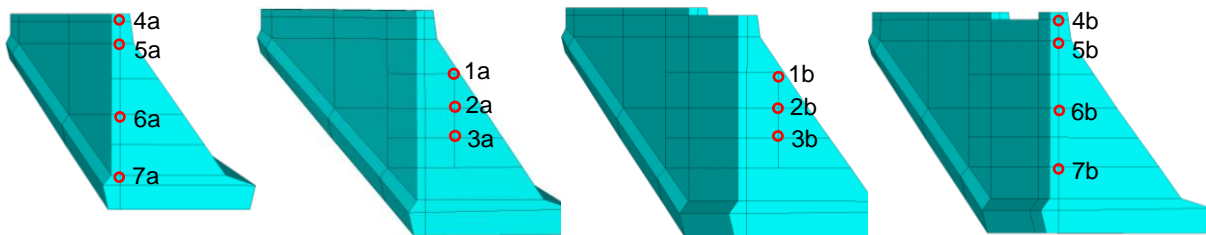


Figure 4.11: Display of the points for mesh accuracy analysis under thermal load

#### 4.3.4 FE model of Rappbode Dam with appropriate mesh

According to the accuracy analysis of mesh density in the thermal and structural analyses in Sections 4.3.2 and 4.3.3, an adequate mesh for the geometrical model of the dam can be concluded. A global element size of 10 m was found to be required to achieve a convergent result to simulate the dam temperature and displacement as well as stress. The computed responses remain steady when the global element size becomes smaller. Higher temperature gradients are detected in the vicinity of exposed boundaries, and finer meshes are thus required in this area.

Based on this analysis, the computational mesh for simulating temperature distribution and deformation behaviour in this thesis is generated as follows. Mesh control is made to generate smaller elements (with an element edge of ca. 0.5 m) for the upper thin area of the dam as well as the area near the structure surface (with an element edge of ca. 1 m) and larger elements (with the largest element edge of 10 m) for the inner area of the dam. Finer meshes in the vicinity of exposed boundary of the dam improve the accuracy of the model, and coarser meshes in the inner zone minimise computational costs. Figure 4.12 displays the FE model of the dam with half the dam to show the mesh control specified for the dam interior.

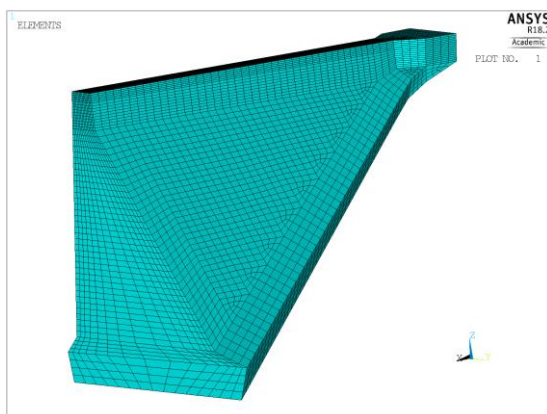


Figure 4.12: FE model of the dam (half of the dam)

The foundation is meshed with a global element size of 10 m. Figure 4.13 presents the FE model of the dam-foundation system with downstream and upstream views, and contact



elements are created for the interface of the dam base and foundation. This FE model with appropriate mesh consists of 169,410 nodes and 154,574 elements totally.

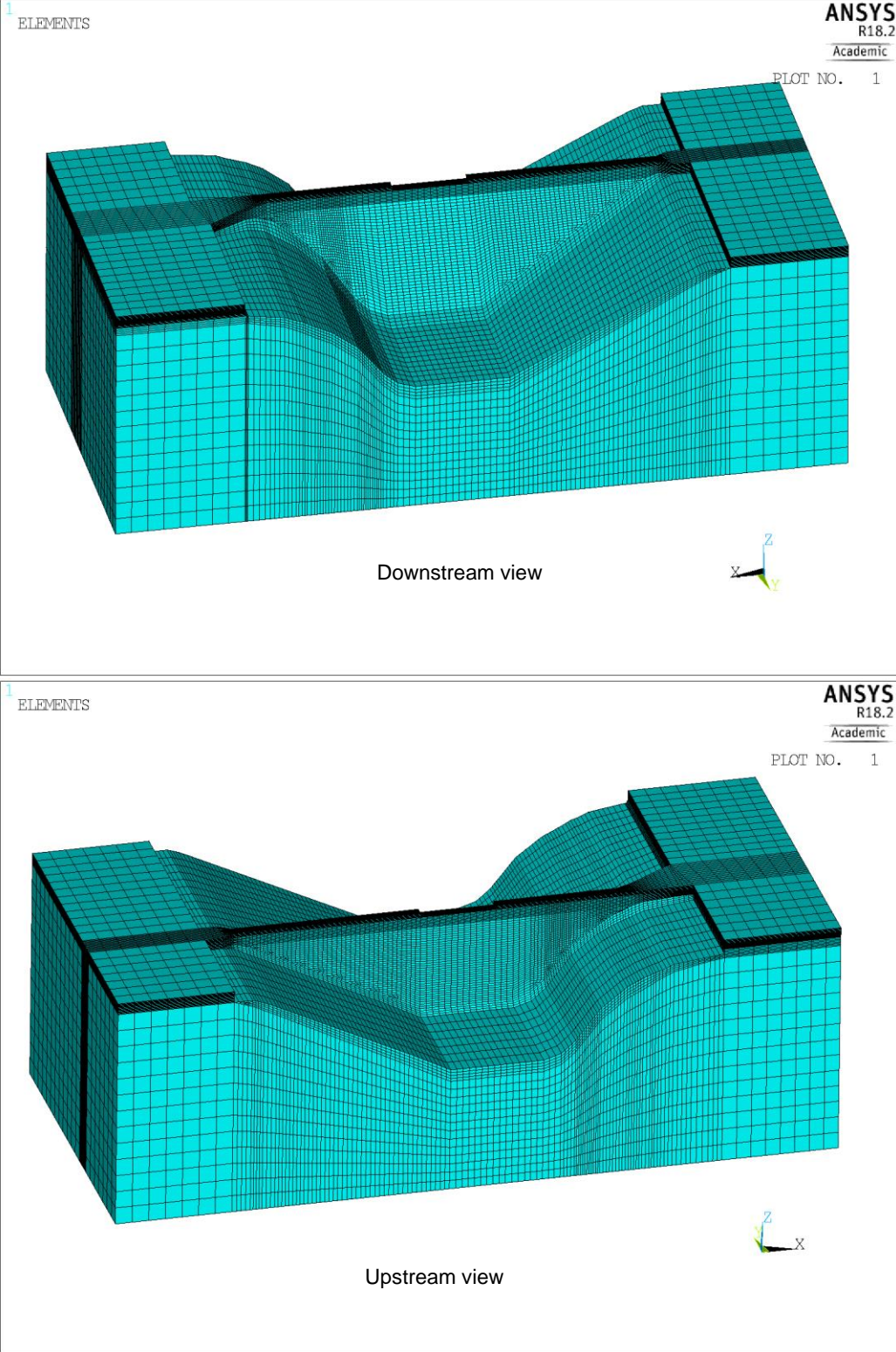


Figure 4.13: The FE model of dam-foundation system

## 5. Back analyses of the material parameters of Rappbode Dam

In this chapter, the parameters are back analysed by calibrating the functional FE model therewith the ANM is developed. The temperature distribution in the dam should be determined during the optimisation process of thermal displacements. The emphasis lies on accurately simulating the transient heat transfer process from the ambient environment to the dam inside. The approach to determine the unknown initial temperature distribution for the transient thermal calibration procedure is investigated firstly, and then, the heat transfer model is calibrated to obtain accurate time-varying temperature distributions interior the dam. Finally, based on the time-varying temperature distribution and superposition principle, the simulations of thermal and structural displacements are calibrated one after another.

### 5.1 Determination of initial temperature distribution

To obtain the temperature field inside the dam and its variation with time, transient thermal analysis is conducted, which should begin from a known temperature distribution state defined as the initial condition, as shown in Section 4.1.3. The quality of the initial temperature distribution greatly influences the calibration of the heat transfer model, because the temperature results in each time step are based on the temperature field of the previous time step. This state is unfortunately normally unknown, thus in this case, the initial temperature distribution must be assumed.

There are different approaches to specify the initial temperature distribution. Venturelli (1992) determined the initial condition by conducting a steady-state heat transfer analysis in which the mean annual air, water and foundation temperatures were applied at the boundaries; however, the effect on the interior temperature distribution due to time-varying ambient temperature could not be presented in the final steady-state results. Fahland (2004) performed a steady-state thermal analysis by applying the observed temperature values at several discrete points, and the thermal transfer process, from ambient environment to inside of the dam, was not considered. Colombo et al. (2016) imposed annual average temperatures on each node interior the dam as the initial condition; however, these annual average temperatures cannot represent the temperature distribution at the origin of the time coordinate for the transient thermal analysis.

To obtain a reliable initial temperature distribution for determining the dam's time-varying temperature distribution via transient thermal analysis, influence of different specified initial uniform temperatures on the interior temperature variation is investigated. In this investigation, transient thermal analysis is adopted to observe the temperature variation over a period based on different initial conditions and the same boundary conditions.

### 5.1.1 Influence of different initial uniform temperatures specified

Regarding the boundary conditions, the ambient environment temperatures are classified as air, water layers and ground temperature, as shown in Figure 4.1. The mean values for each day of the one-year period can be obtained by averaging the recorded temperature values at the same day in different years, which are defined as daily design temperatures in a one-year period in this thesis. Air temperature and water side temperature wt1, wt2, ... wt8 for a design year are displayed in Figure 5.1. The minimum value of air temperature is in January, while the maximum is in July. The temperature variation for additional years can be obtained by repeating the daily design temperature year after year.

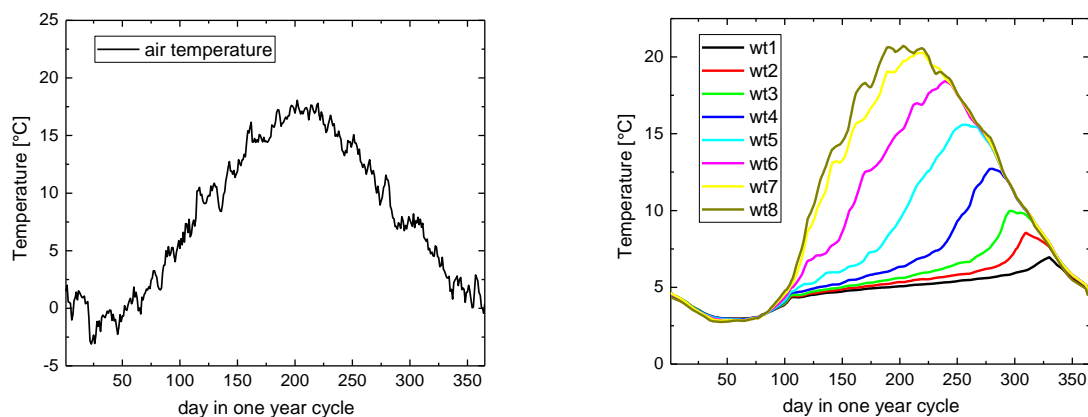


Figure 5.1: The daily design temperature in a one-year period

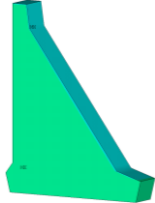


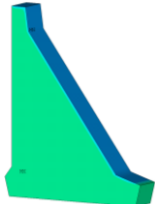

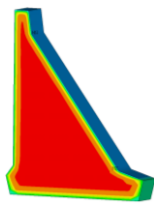

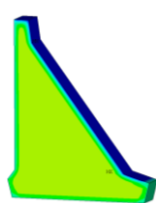
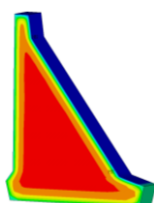

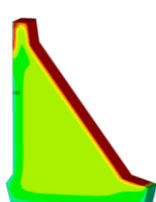

Three arbitrary temperature values, namely 5°C, 10°C and 15°C, are selected to represent three different initial temperature states, and each value is specified on all the nodes of the FE model as a uniform temperature. Then under the above described boundary conditions, three transient thermal analyses are conducted with initial uniform temperatures of 5°C, 10°C and 15°C for all the nodes respectively to investigate the influence of different initial uniform temperatures on the time-varying temperature distribution interior the dam. The material properties used in these calculations utilise the values in Table 4.4 and starting values in Table 4.5, and the unit system is listed in Table 4.2.

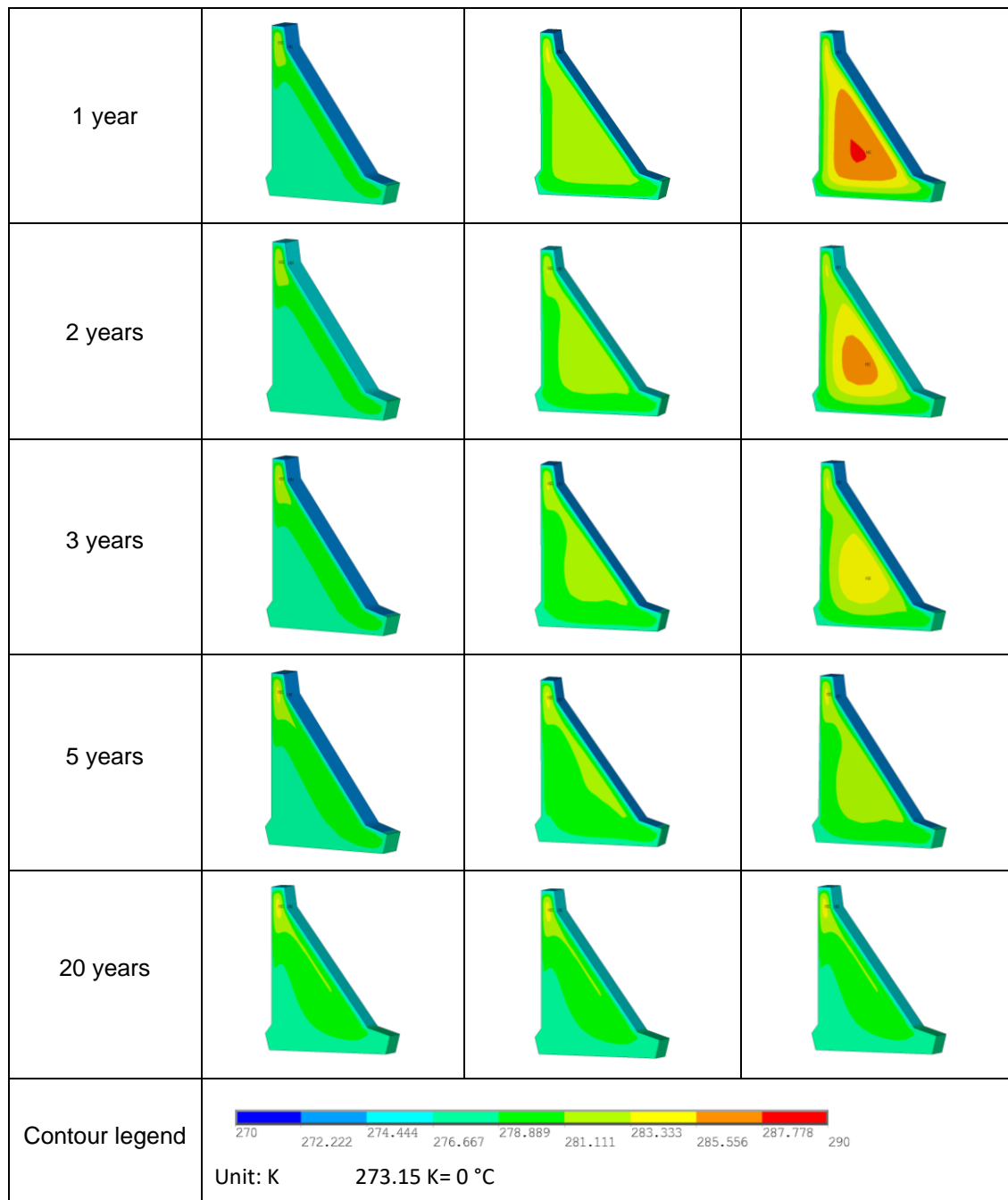
The colour contours of the temperature distributions interior the dam at different timepoints of the transient thermal analyses are displayed in Table 5.1 with a section view of the central block 14. The same legend is adopted for these colour contours to present the change in interior temperature distribution over time.

For the time point 1 day, only the temperatures at the face exposed to the environment are the same, while the temperatures inside are totally different among the three analyses. As time passes, the temperature influence zone gradually increased from the surface to the inside. At the time point of 6 months, for the temperature distribution inside from the calculation with

initial uniform temperature of 5 °C, except the vicinity of exposed surface to air, the upper thin zone is also changed when compared with the result at time point of 1 day; for the calculation with initial uniform temperature of 10 °C, compared with the temperature distribution at the beginning, all the zones adjacent to the surface specified with boundary conditions changed; for the calculation with initial uniform temperature of 15 °C, the boundary temperatures influenced a larger zone than the former two starting temperatures. At the timepoint of 1 year for the initial uniform temperature of 15 °C, only a small zone inside the lower thicker part of the dam remains the same colour as the beginning before the colour contours slowly change in the whole dam. At the timepoint of 5 years, the temperature distributions inside the dam from the three calculations are more analogous compared to the previous timepoint; for the zone near the boundary surface, the temperature distributions are already identical, while the temperature distributions at the core of the lower thicker part of the dam are still different. Finally, at the timepoint of 20 years, the colour contours of temperature distribution from the three calculations are identical.

Table 5.1: The temperature field change inside the dam with different initial temperatures

Time	Initial temperature 5°C	Initial temperature 10°C	Initial temperature 15°C
1 day			
10 days			
1 month			
6 months			



For the purpose of investigating the changing of temperature values inside the dam, Figure 5.2 displays the time series of temperatures at locations T1, T6, T11 at block 18 (shown in Figure 3.5). Despite different initial temperature values, the temperature values at the same location eventually converge to the same value over time. Convergence occurs when a repetitive temperature series is obtained from year to year or constant temperature values for one location are achieved.

T1 is located 2.5 m under the crown in the upper thin part of the dam, the outside temperature variation conquers the temperature variation at this location after 250 days in the 1<sup>st</sup> year cycle. For location T6, whose perpendicular distance to the upstream face is 3.3 m and located at a thicker part of the dam than T1, convergence is obtained after 1,500 days in the 5<sup>th</sup> year cycle.

For in the core of the lower thick part of the dam located T11, the temperature values converge to a constant value after about 5,500 days in the 16<sup>th</sup> year cycle. In the calculation with same material properties, different dam locations have different convergence rates, where locations closer to exposed surface have a rapid convergent rate.

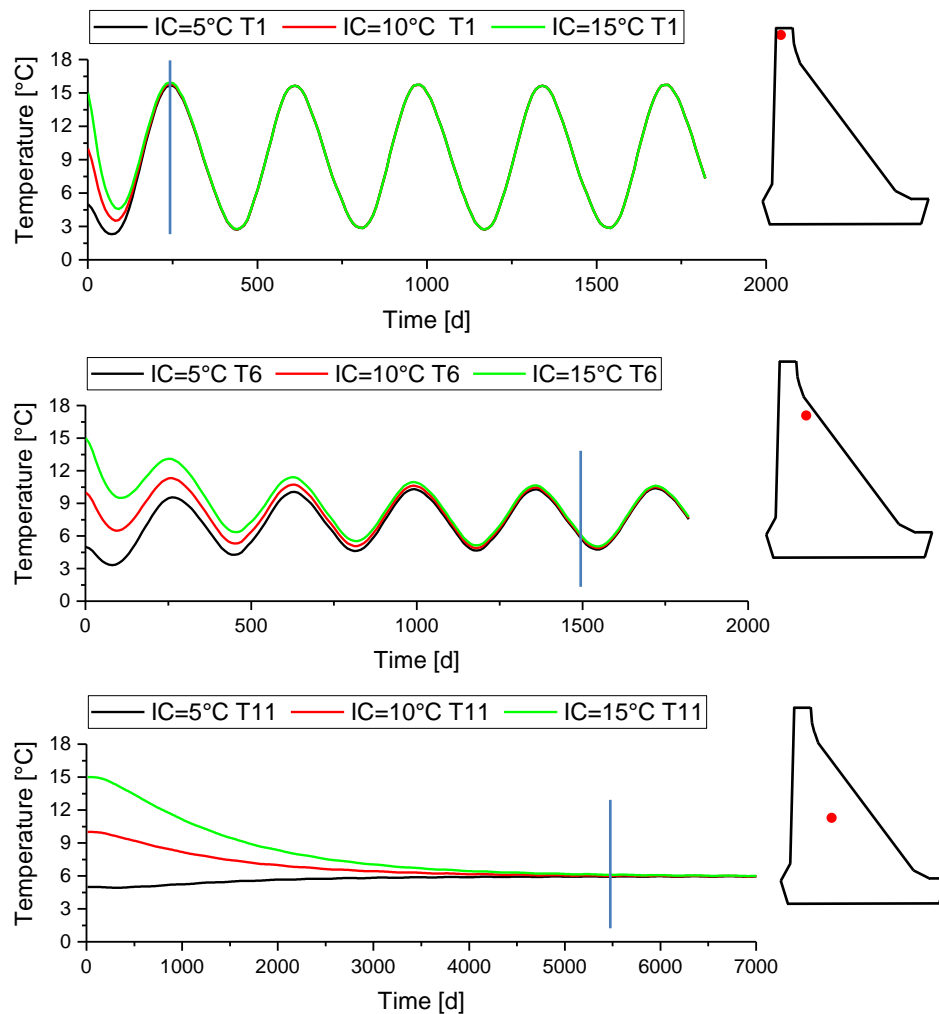


Figure 5.2: The time series of temperature value at different locations in the dam

It can be concluded that, when there is no heat source inside the dam and the heat of hydration development has dissipated, with an arbitrary initial temperature distribution, the longer the periodically changed temperature load is applied to the model, the more convergent the structure's calculated temperature distribution to the actual distribution. After a sufficient period, the periodically changed temperatures finally control the temperature variation in the dam and the time-varying temperature distribution reaches a quasi-stationary state. This is in accordance with the theoretical results (seen in Equation (B.10)) from the one-dimensional heat transfer problem (seen in Appendix B). The influence from the initial uniform temperature value is faded away if the boundary temperature conditions act on the dam for a sufficient length of time. In the case of Rappbode Dam, a 20-year period is demonstrated to be sufficient to acquire the convergent temperature distribution.

### 5.1.2 Specification of appropriate initial temperature field

Based on the analysis in Section 5.1.1, a reliable simulation of time-varying temperature distribution can begin from a temperature state from a 20-year transient thermal analysis under ambient temperature conditions. However, the in-situ ambient temperature measurements do not cover so much time for the Rappbode Dam, thus as an efficient alternative, the daily design temperature is repeated 20 times to represent the variation of boundary temperature conditions for a 20-year period.

The initial temperature distribution inside the dam in this thesis is specified in the way as follows: Firstly, a transient thermal analysis was conducted for a time period of 20 years with an initial uniform temperature field of 5°C and under daily design temperature boundary conditions. Then, the temperature distribution from the above transient thermal analysis in the last year cycle can be set as the initial temperature field for later analyses. The temperature distribution on which day in the last year cycle is eventually specified depending on the starting date of the desired calculation. For example, if the desired thermal analysis begins on February 1<sup>st</sup> in a certain year, then the temperature distribution on the 31<sup>st</sup> day in the last year's cycle is chosen as the initial temperature field.

In this way, the initial temperature field can take the thermal transfer process (from ambient environment to inside of the dam) into consideration; can present the effect of time-varying ambient temperatures on the interior temperature distribution; and can represent the temperature distribution at the origin of the time coordinate for the transient thermal analysis.

Figure 5.3 shows a section view for block 18 of the temperature field inside the dam on the 365<sup>th</sup> day in the last year's cycle of the 20-year transient thermal analysis. It can be seen from Figure 5.3, firstly, a continuous nonlinear temperature contour exists for the interior of the dam; secondly, the upper thin part of the dam shows a warm interior and cold surface, which is the effect of time-varying boundary temperatures; thirdly, for the lower thick part of the dam from the downstream face to inside, there is also a warm zone under the cold downstream face interior the dam.

Figure 5.4 shows the temperature for horizontal paths at different elevations: a (339.5 m a.s.l.), b (377.5 m a.s.l.) and c (415.5 m a.s.l.) in the cross section of block 18. Although the temperature values at the upstream and downstream faces for these different elevations remain identical, the temperature values between upstream and downstream face demonstrate a great difference: for the path at elevations a and b, a higher temperature gradient occurs at the zone near the downstream face and a lower temperature gradient at the zone from the upstream face to the highest temperature point; for elevation c, a higher temperature gradient occurs both before and after the highest temperature point. This results



from the time series of ambient temperature specified on the boundary of the model and the structural geometrical features, where different elevations in the dam correspond to different thicknesses in the upstream-downstream direction.

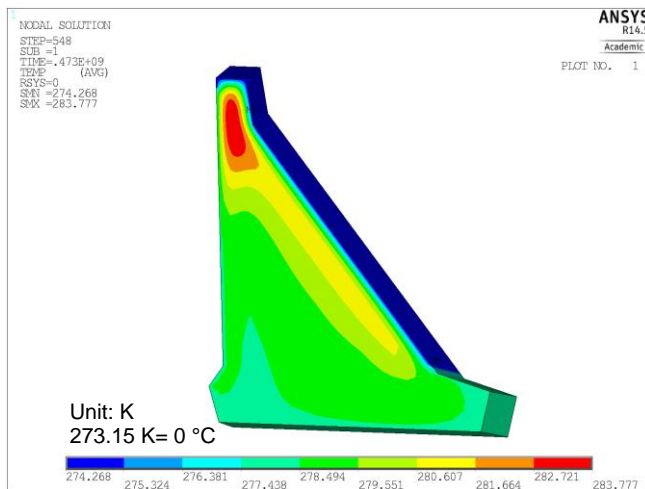


Figure 5.3: Cross section view for block 18 of the temperature distribution

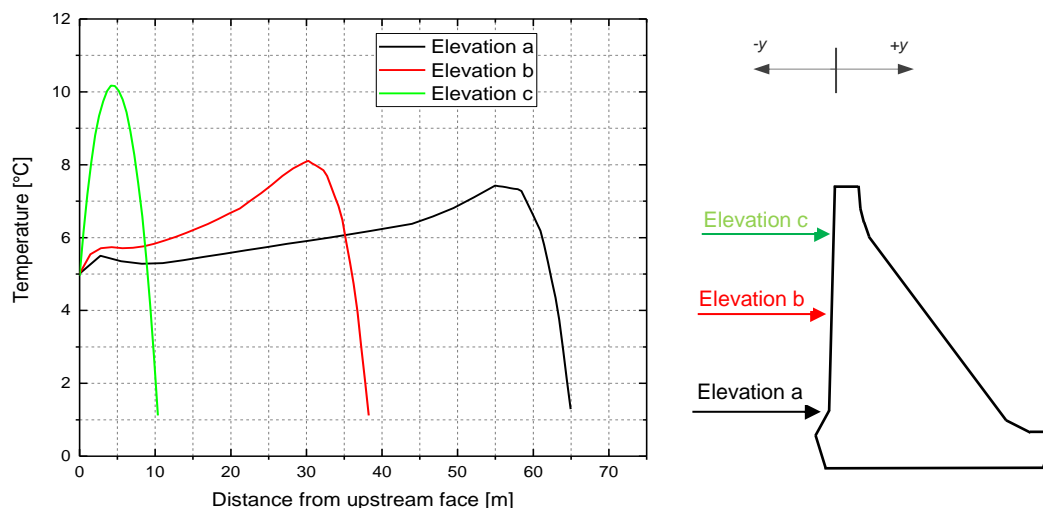


Figure 5.4: Temperature values for elevations a, b and c in cross section of Block 18

## 5.2 Calibration of transient heat transfer model

The accuracy of the temperature distribution affects the accuracy of the thermal displacement. In this Section, the heat transfer model is calibrated using the concrete temperature recorded within the dam. This optimisation process back analyses the thermal material parameter, thermal conductivity of the concrete for dam body and modifies the boundary conditions.

### 5.2.1 Back analysis of effective thermal conductivity

As described in Section 4.2.2, the critical material parameters are back calculated by defining a starting value, and then, an interval of this parameter can be investigated to achieve the final effective value.



Based on the FE model of the dam, a starting value of 2 W/(mK) is specified for the thermal conductivity of concrete of the dam and interval values of [1,2,3,4] are adopted, as listed in Table 4.5, and the other material properties used in these calculations are the values listed in Table 4.4. Secondly, as for the initial temperature distribution state, the temperature distribution on 365<sup>th</sup> day of the last year cycle from the previous 20-year transient thermal analysis in Section 5.1.2 is specified. Thirdly, as for the boundary condition, the classification of the boundary temperatures in Figure 4.1 is used here, and except for the ground temperature with the constant value of 5 °C, the air- and water-side temperatures are the in-situ measurements. This transient thermal analysis is conducted for the period from 2009 to 2012.

Comparisons between measurements and computed temperature values from calculations with different thermal conductivities are conducted. Figure 5.5 shows the comparison results for two measuring points T2 and T9 in the upper part of the dam, which belongs to temperature-prone zone, to present the differences from different thermal conductivity values.

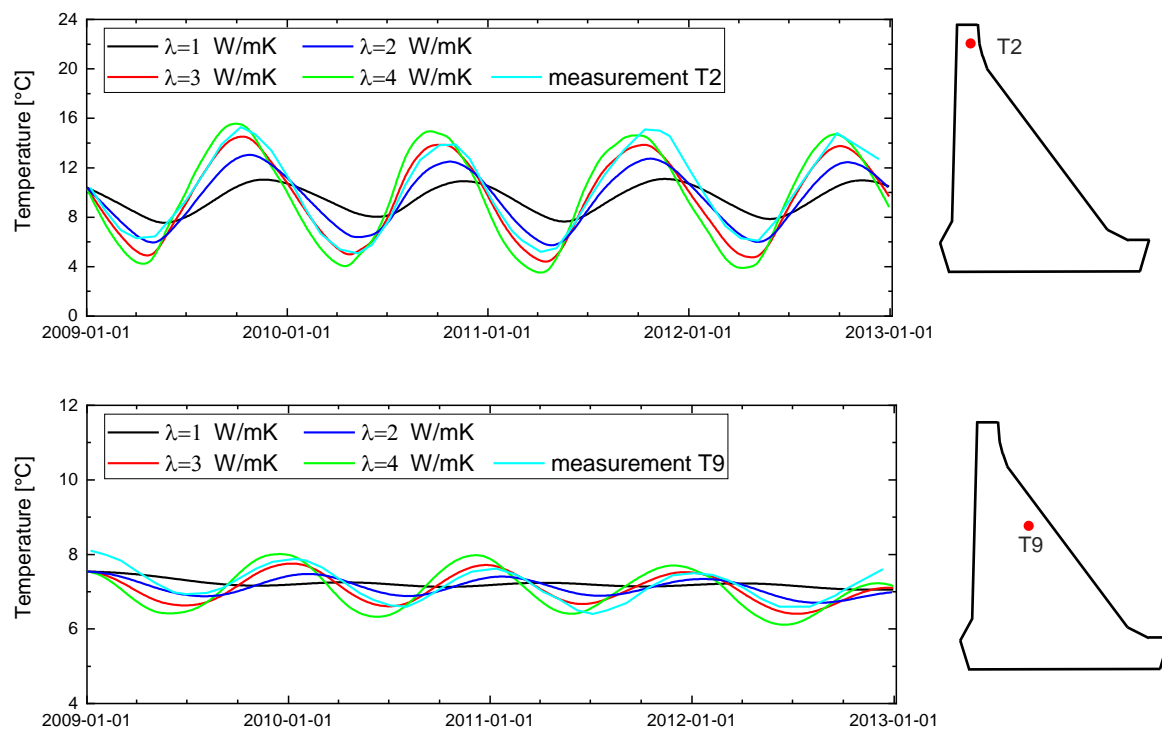


Figure 5.5: Comparison between calculated temperatures with different thermal conductivity values and measured data at T2 and T9

In these comparison graphics in Figure 5.5, similar to measurements, a yearly sinusoidal tendency of calculated temperatures can be detected. Both the amplitude and phase position of each calculated curve should be compared with the corresponding measured temperature curve. In terms of temperature variation amplitude, for measuring point T2, the thermal conductivity values 3 and 4 W/(mK) perform better than 1 and 2 W/(mK); for T9, results from 3

W/(mK) are better aligned with measurements than the other values. As for phase position, the thermal conductivity value of 3 W/(mK) matches best for both T2 and T9. Compared to amplitude, the phase position of the calculated temperature curve plays a greater role since the amplitude of the curve can be influenced by the specified boundary temperature values, but the phase position presents the results that how rapid betheat transfer from the outside to inside under the specified parameter of thermal conductivity.

In Figure 5.6, the computed temperatures at measurement point T0 present tiny differences with the change in thermal conductivity but significant deviations from the measurement data. Considering T0 is only 0.3 m away from the upper surface of the dam, thus rather than the thermal conductivity, the specified air temperature at the boundary is decisive for the computed temperature values at T0.

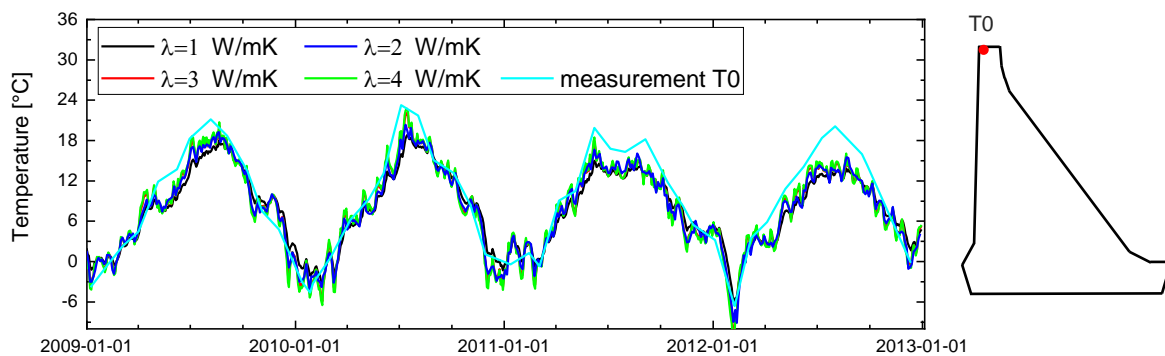


Figure 5.6: Comparison between calculated temperatures with different thermal conductivity values and measured data at T0

By investigating the specified air temperature and recorded temperature at T0, there is deviation between them. The mean value of these deviations is 1.93 °C, which is potentially due to solar radiation or the temperature's recorded time. Solar radiation can heat the dam surface via conduction, which results in deviation between the surface concrete and ambient air temperature. The air temperature recorded at 7 am is taken as the mean value of a day in this thesis, but this value could be lower than a day's actual mean temperature.

Seen in Figure 5.7, for in the lower thick part located T19, temperature values from calculations with different thermal conductivity  $\lambda$  show actually the same results. Slight variation throughout the year is obtained from the measured temperatures, but the computed temperatures remain constant and are about 0.5 °C higher than the measured values. The same problem is also found at T20.

In conclusion, a reasonable value of thermal conductivity for concrete is determined by comparing the computed and measured temperatures. A value of 3 W/(mK) is adopted as the effective thermal conductivity of concrete in the case of Rappbode Dam. For the temperature at T0, better alignment with measurements could be reached by modifying the boundary air

temperature, while for the temperature at T9 (seen in Figure 3.5) with a thermal conductivity of 3 W/(m K), good agreement is already achieved between the computed and measured values. For the stated problem at T0, T19 and T20, some adjustments to the specification of boundary temperature are proposed in the next section.

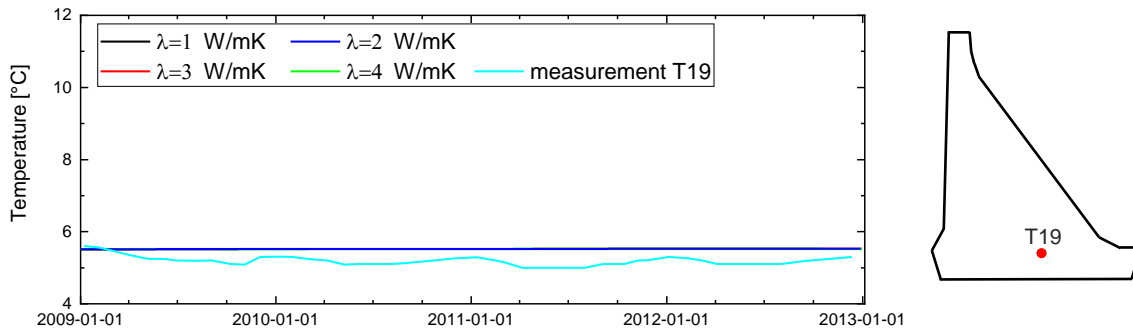


Figure 5.7: Comparison between calculated temperatures with different thermal conductivity values and measured data at T19

### 5.2.2 Adjustment of the boundary temperature conditions

Based on the analysis in Section 5.2.1, improvement of results at T0 could be achieved by increasing the boundary air temperature at the upper thin part of the dam. Because computed temperatures at T19 and T20 in the lowest row are higher than the measurements, the matches would be better if the boundary ground temperature near these two locations is decreased.

Hence, a modified boundary condition, shown in Figure 5.8, is proposed herein. The air-concrete contact boundaries are specified with two slightly different values at the upper and lower parts of the downstream face respectively. The lower thick part of the dam (below 400 m a.s.l.) is specified with the original air temperature “at”, while the upper part is the modified air temperature “at2”. For the modified air temperature “at2”, attempts of increasing the air temperature by 1 °C, 2 °C, 3 °C, 4 °C and 5 °C are performed and it has been proved that the calculation results by increasing the upper boundary air temperature by 2 °C, which corresponds to the mean deviation between the recorded air temperature and recorded temperature at T0, provide better alignment for the measurement positions located in the upper thin zone of the dam. The ground temperature is also analogously divided into two parts; the temperature “gt1” at the ground adjacent to the air side is 0.5 °C lower than that adjacent to the water side. These modified boundary conditions in Figure 5.8 are proposed to overcome the deviation between computed values from former boundary conditions and measurements.

The results from the modified boundary condition are then compared with the former boundary condition, and the comparison results for measuring points T0, T2 and T19 are presented to demonstrate improvements.

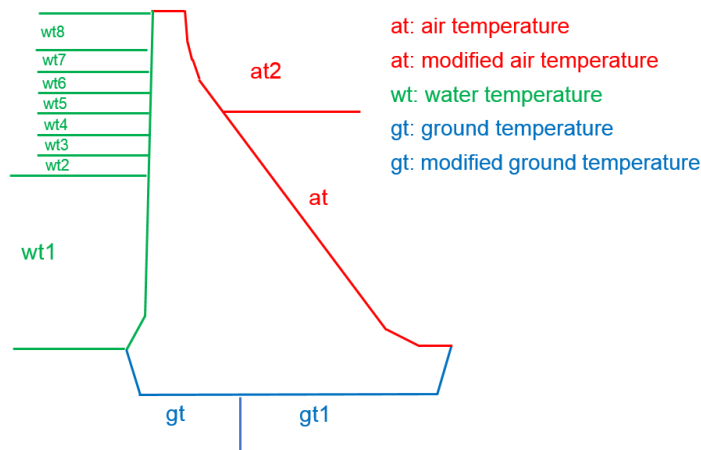


Figure 5.8: Modified boundary temperature conditions

Figure 5.9 shows the comparison between computed temperatures from the original and modified boundary conditions and measured temperatures at T0 in block 18. The black line (represents results from modified boundary conditions) is better aligned with the measurements in this window. Although variation tendencies remain the same, deviations occur in the middle of 2011 and 2012, which may stem from the time of measurements in the same day (air temperatures at 7 am, and T0 unknown). It is not worthwhile to further increase the modified air temperature, because besides these two deviations, favourable agreement has been achieved for T0 at other time points.

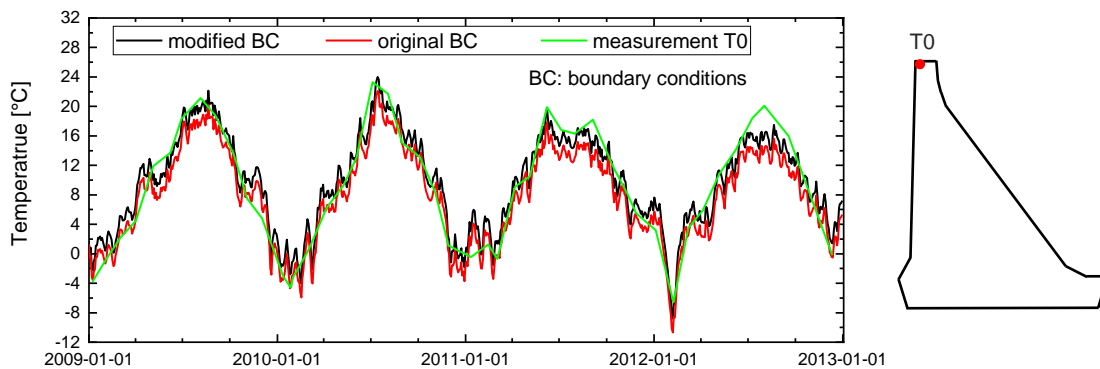


Figure 5.9: Comparison of computed values from two different calculations with measured values at T0

The computed and measured temperature values at T19 in Figure 5.10 demonstrate that the computed values from the modified boundary conditions presents a better match with the measured temperature than those from the original boundary conditions.

Figure 5.11 shows the comparison of computed and measured temperatures at T2 (location shown in Figure 3.5) as an example from the upper measurement points from T1 to T6. Here, the black line shows the results from the calculation with increased air temperature and the red line the original air temperature. In the four temperature variation cycles, peak values from the first, third and fourth cycles of the black line match better than those of the red line, and

the red line matches better with the green line only in the second cycle. An improvement in temperature matching is thus achieved when increasing the original air temperature by 2 °C.

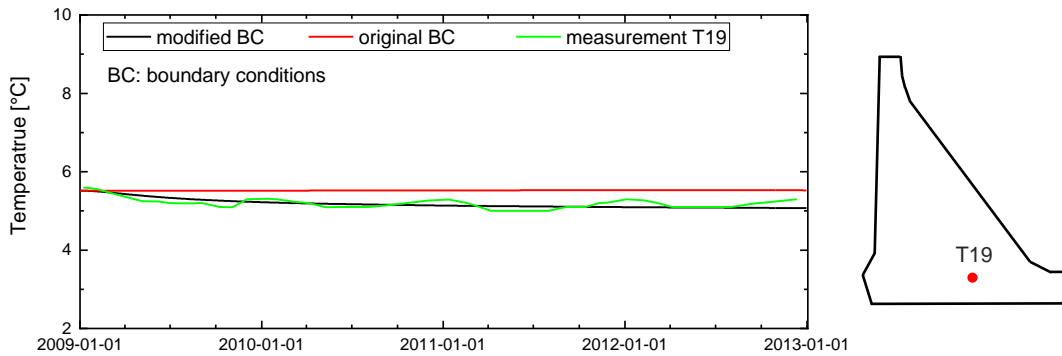


Figure 5.10: Comparison of computed values from two different calculations with measured values at T19

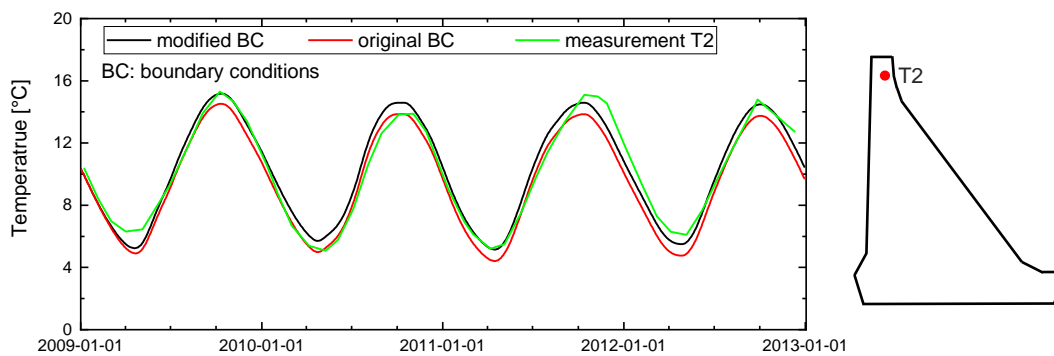


Figure 5.11: Comparison of computed values from two different calculations with measured values at T0

The comparison results between the computed and measured temperature values for the 21 measuring points are displayed in Figure 5.12, and the locations of the measuring points are displayed in Figure 3.5. The temperature variations inside the dam due to this transient thermal analysis present alignment with the measurements. The temperature displayed in Figure 5.3 is specified as the initial temperature distribution conditions, and in Figure 5.8 depicted modified boundary conditions are specified on the boundary. The transient thermal analysis can provide temperature distribution results those are aligned with measurements by specifying reasonable initial conditions, calibrating the material parameter thermal conductivity of concrete and adjusting the boundary conditions.

So far, the transient heat transfer model is calibrated to acquire precise temperature distributions inside the dam for any desired timepoint. It should be mentioned that, a well-match-oriented modification of the boundary conditions in this section represents an effective method to acquire accurate temperature distribution inside the dam, but it is not the sole method in the numerical simulation of temperature fields. For example, modifications of the FE

model or concrete properties provide further opportunity, but in this thesis, these two factors are handled as stated in Chapter 4.

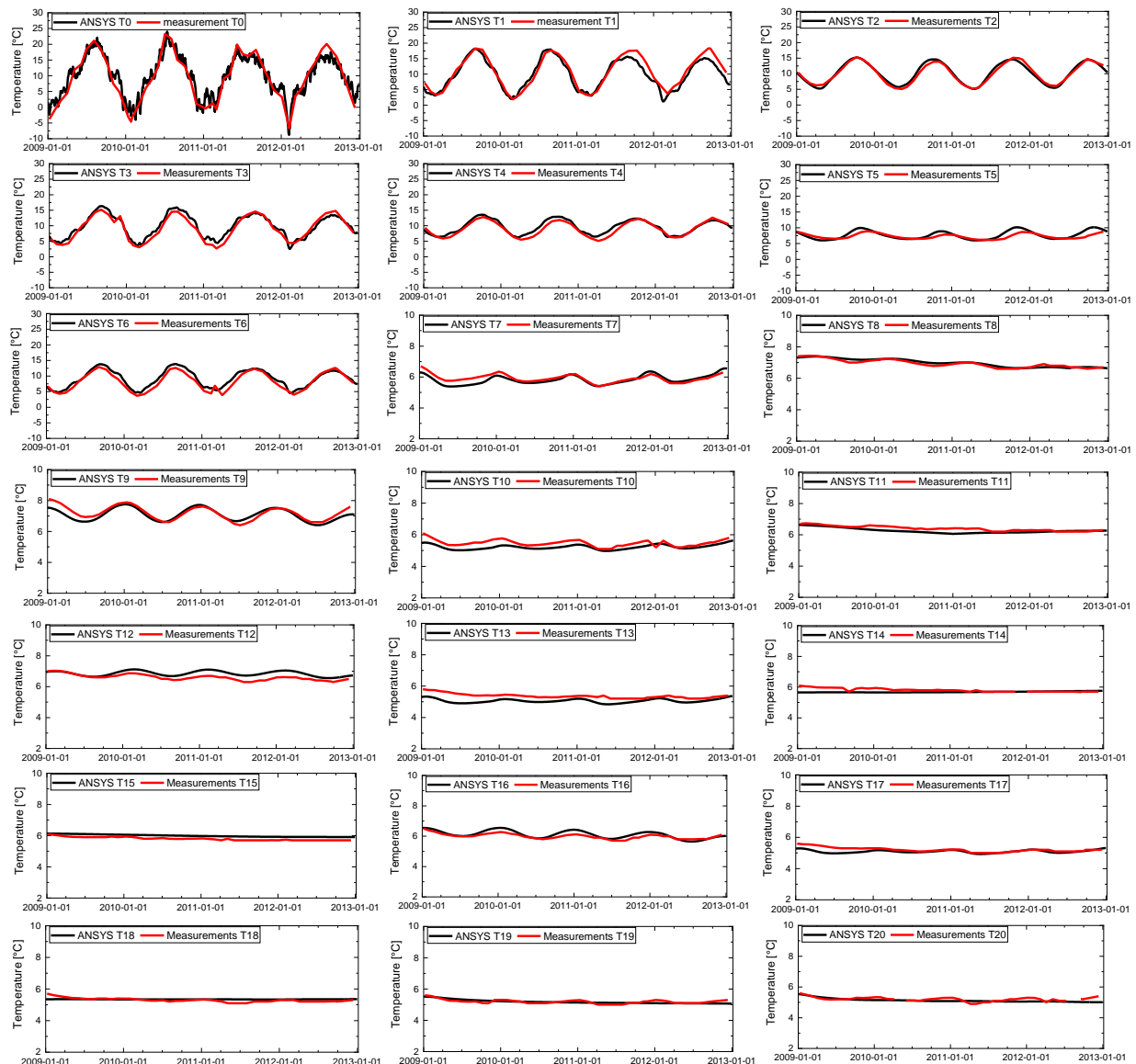


Figure 5.12: Comparisons of computed temperature and measured temperature at T0-T20

### 5.3 Back analysis of parameters in structural analysis

In the structural analysis of concrete dams' deformation behaviour, the seasonal thermal load induces delayed displacement and the water pressure load induces immediate displacement, as mentioned in Section 2.3. To perform a separate calibration, a time period is firstly chosen with small changes or steady state in water level but regular cycles in temperature, thereby allowing the effective thermal expansion coefficient to be back analysed with subsequent calibration of the thermal displacements. Based on the superposition principle, the effective elastic modulus of the concrete can then be back analysed when choosing the period with both variations of water level and ambient temperature.

### 5.3.1 Back analysis of effective coefficient of thermal expansion

The air temperature and water level time series in Figure 5.13 shows that, in the time period between 26<sup>th</sup> March 2007 and 13<sup>th</sup> August 2007, the monthly recorded water levels narrowly varied between 420.01 m a.s.l. and 420.94 m a.s.l. Hence, this period is chosen as a steady water level to perform the back calculation of the effective coefficient of thermal expansion.

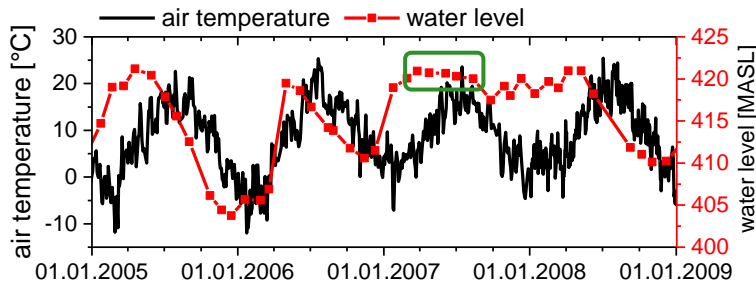


Figure 5.13: Comparison of time series of water level and air temperature

The model, unit system and material properties for this back analysis are shown in Figure 4.13, Table 4.2 and Table 4.4. The thermal conductivity of concrete is specified with the value 3 W/(mK), and the thermal expansion coefficient  $\alpha$  is investigated with a starting value of  $9\text{e-}6$  1/K, where the indicated interval of 5 to  $14\text{e-}6$  1/K is considered. Transient thermal analysis is firstly conducted to obtain the temperature distributions. The temperature distribution on the 365<sup>th</sup> day in the last year's cycle of the 20-year transient thermal analysis in Section 5.1.2 is specified as the initial temperature conditions, and the boundary conditions shown in Figure 5.8 are used for the transient thermal analysis of the period from 1<sup>st</sup> January 2007 to 31<sup>st</sup> August 2007, which allows obtaining the temperature distribution each day during this time period. The temperature distribution results of the displacement recorded dates between 26<sup>th</sup> March 2007 and 13<sup>th</sup> August 2007 are then specified as body loads to obtain the computed thermal displacements. To compare the displacement variations, the displacement values from the calculation are processed by removing their mean value to obtain the variation, namely the relative displacements. Each thermal expansion coefficient corresponds with a set of computed relative displacements, which is compared with the recorded relative displacements, aiming to determine the effective thermal expansion coefficient.

Figure 5.14 lists 6 measurement points in 2 blocks (blocks 14 and 18) at elevations C, B and A, namely 14C, 14B, 14A, 18C, 18B and 18A (as shown in Figure 3.4), to determine the most appropriate value of effective thermal expansion coefficient. For points 18C and 18B, results from the thermal expansion coefficient  $11\text{e-}6$  1/K provides better alignment with measurements; for points 14C and 14A,  $11\text{e-}6$  1/K or  $14\text{e-}6$  1/K matches better with measurements; for point 14B,  $9\text{e-}6$  1/K and  $11\text{e-}6$  1/K are appropriate; for point 18A,  $14\text{e-}6$

1/K presents better results. Considering the alignment for each graphic overall, 11 e-6 1/K is decided as the effective thermal expansion coefficient of the concrete.

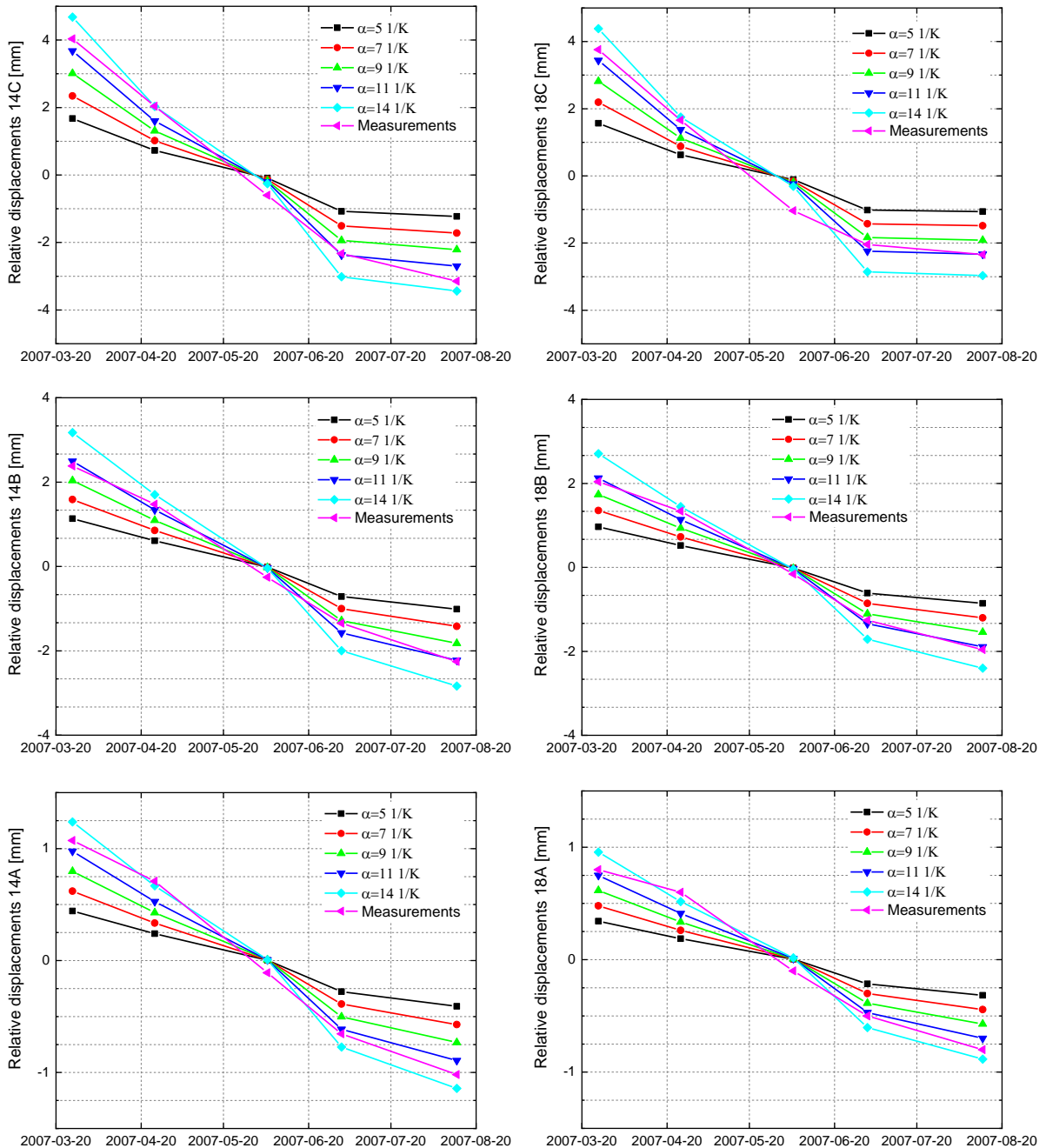


Figure 5.14: The calculating displacements with different  $\alpha$  and measured displacements

### 5.3.2 Back analysis of effective elastic modulus for dam body

Because of the delayed thermal response of temperature inside the dam, even for time periods with small changes or steady state in temperature but regular cycles in water level, the thermal effects cannot be excluded. Based on the superposition principle in linear elastic material assumption and computed thermal displacements from the calibrated model, the structural displacements due to water level are therefore obtained by removing the computed thermal



displacements from the measured displacements, which is here defined as the reference values of water-induced displacement. Then, the decisive material parameter related to water load, the effective elastic modulus  $E$  of dam body, is back analysed based on the reference values of the structural displacements.

The period from 1<sup>st</sup> April 2011 to 31<sup>st</sup> August 2011 is chosen to investigate the effective elastic modulus of the concrete. The thermal-structural coupled analyses are conducted using the methodology described in Section 5.3.1 with the effective thermal expansion coefficient of  $11 \times 10^{-6}$  1/K to obtain the relative thermal displacements on the displacement recorded dates during this time period. Then, the reference value of structural displacement induced from water level can be gained for each displacement recorded date.

To compute the structural displacement due to water level, the model of the dam-foundation system displayed in Figure 4.13 is employed, and in Table 4.2, Table 4.3 and Table 4.4 listed unit system and material parameters are specified. Additionally, as already listed in Table 4.5, the starting value of  $2.0 \times 10^{10}$  Pa and interval of  $[1.5 \times 10^{10}, 3.5 \times 10^{10}]$  Pa for the elastic modulus of concrete is taken into consideration. The relative displacements under the loads of hydrostatic pressure on the upstream surface, the uplift pressure at dam base and self-weight of dam-foundation system are taken into consideration. Each elastic modulus has a corresponding set of relative displacement results, and Figure 5.15 shows comparisons between these computed and reference values of relative displacements.

As can be seen from Figure 5.15, the different  $E$  values present different slope parameters in the computed results, where the smaller the  $E$ , the larger the relative displacements for a certain point in the dam. Each measurement point includes deviations between the computed displacements and reference values which could be due to many reasons: errors in temperature induced thermal displacements, existence of galleries and shafts, inhomogeneous material and measurements errors. For points 18C, 14B and 18A, the value of  $2 \times 10^{10}$  Pa shows better alignment along with  $1.5 \times 10^{10}$  Pa and  $2 \times 10^{10}$  Pa for 14C, and  $2.0 \times 10^{10}$  Pa and  $2.5 \times 10^{10}$  Pa for 18B and 14C respectively. Based on these results, the effective elastic modulus of the concrete is decided to be specified with the value of  $2 \times 10^{10}$  Pa.

The effective values of parameters from the back analysis are summarised and listed in Table 5.2. It should be mentioned that, these parameters are effective values of parameters that can reflect the current state of the material properties of the dam body when simulating time-varying temperature distribution and deformation behaviour. So far, the numerical model is calibrated by describing the thermal distribution within the dam body and deformation behaviour of Rappbode Dam. The ANM is finally developed based on the functional FE model in Section 4.3, the initial temperature field specification in Section 5.1, the modified temperature boundary conditions in Section 5.2 and the updated effective material parameters in Table 5.2.

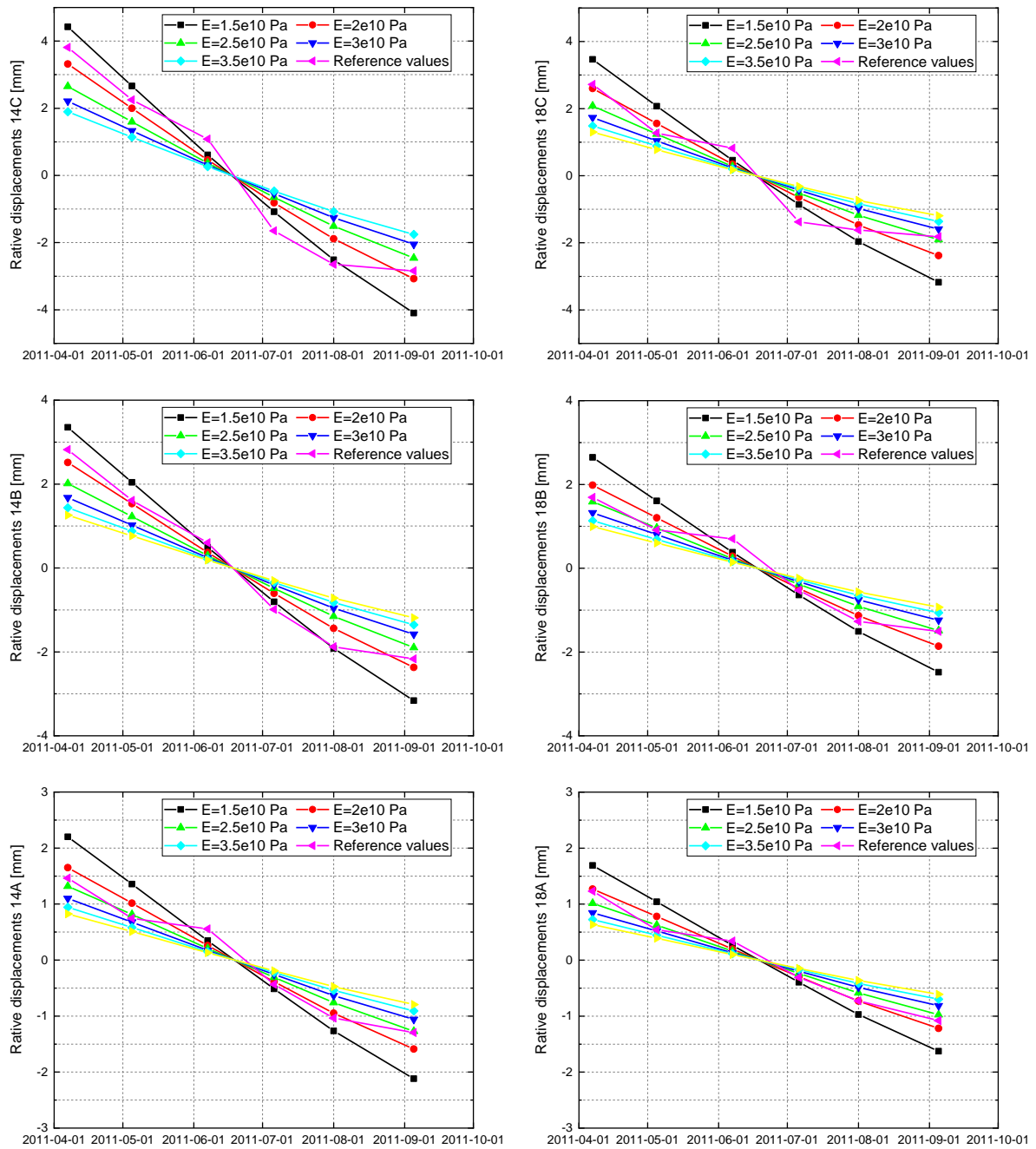


Figure 5.15: Comparison of water level induced displacements and reference values

Table 5.2: Effective values for the three critical parameters

Material parameters of concrete	Effective values
Thermal conductivity (W/(m·K))	3
Thermal expansion coefficient (1/K)	11e-6
Elastic modulus (Pa)	2.0e10

## 5.4 Conclusions

In this chapter, the material parameters including effective thermal conductivity, effective coefficient of thermal expansion and effective elastic modulus for the dam body are back analysed in the thermal and structural analyses.

The transient thermal analysis shows that the influence due to the initial temperature state diminishes over time; in the case of Rappbode Dam, this influence can be neglected after a 20-year time period under annual-cyclic boundary temperature. The temperature in the vicinity of the dam's exposed face is strongly influenced by the temperature at the exposed face, and slightly adjusting the corresponding boundary temperature resulted in better alignment between the computed and measured temperatures of the dam.

In the deformation model calibration, the effective coefficient of thermal expansion and effective elastic modulus of concrete are back analysed one after another based on calibrated time-varying temperature distribution and the superposition principle. The thermal and mechanical material properties are thereby updated to adapt the operational phase of the dam, and an ANM is thereby developed which is capable to investigate the current deformation behaviour of Rappbode Dam due to external water and temperature loads.

This calibration procedure of the numerical model provided a general guideline for the parameter determination of a dam in operational phase regarding the temperature distributions and deformation behaviours. The greatest advantage of this methodology is that the delayed thermal response interior the dam can be taken into consideration since the temperature response process inside the dam is optimised via transient thermal analysis, presenting a reliable simulation of time-varying temperature distributions.

## 6. Deformation behaviour based on numerical simulation

The monitoring data cannot tell the information about how the dam deforms with changes in water level or ambient temperature. Based on the developed ANM, it becomes accessible to separate the individual proportions of time-varying temperature distribution induced thermal displacements and water level related hydrostatic pressure and uplift pressure induced structural displacements. In this chapter, the thermal displacements, structural displacements and simultaneous displacements as well as their relationships are investigated in detail. Firstly, the thermal and structural displacements are presented respectively to comprehend the deformation behaviour of the dam under single time-varying variable. In these simulations based on ANM, not only the usual variation ranges of temperature and water level but also the unusual variation ranges are taken into consideration. And then, simultaneous simulations of regular ambient temperature and water level as well as an example of unusual load case is conducted based on the ANM. In the simultaneous simulation, the computed deformation behaviour under usual loading conditions is compared with monitoring data to verify the performance of the ANM. The relationship between displacements due to single variable and displacements due to both variables are investigated to detect the weightiness of different external variables of ambient temperature and water level on the displacement distributions. In the example of an unusual loading condition, the combination of unusual weather and water level is taken into consideration to predict the displacement as well as the health state of the dam.

### 6.1 Thermal displacements under time-varying temperature distribution

In the structural analysis, the thermal displacement is computed based on the input of the time-varying thermal distribution within the dam body from the transient thermal analysis, as shown in Sections 5.1 and 5.2. As mentioned in Section 4.1.2, the reference temperature for the thermomechanical response is set to 5 °C.

#### 6.1.1 Thermal response under usual temperature situations

As stated in Sections 3.3.3 and 3.3.4, the ambient temperature changes over time, so that it is necessary to investigate changes of interior temperature and thermal displacement at the same location in the dam and identify their relationship. Because the ambient temperature presents different characteristics in wintertime and summertime, the corresponding thermal responses are compared to show the differences in this section.

### Time series of temperature and thermal displacements

To present the dam response under ambient temperature variations, the time series of concrete temperatures at certain points and corresponding thermal displacements in the upstream-downstream direction are plotted together in Figure 6.1 for the year 2010. Points 17C, 17B and 17A (shown in Figure 3.4) are selected to represent the responses at different elevations of the dam.

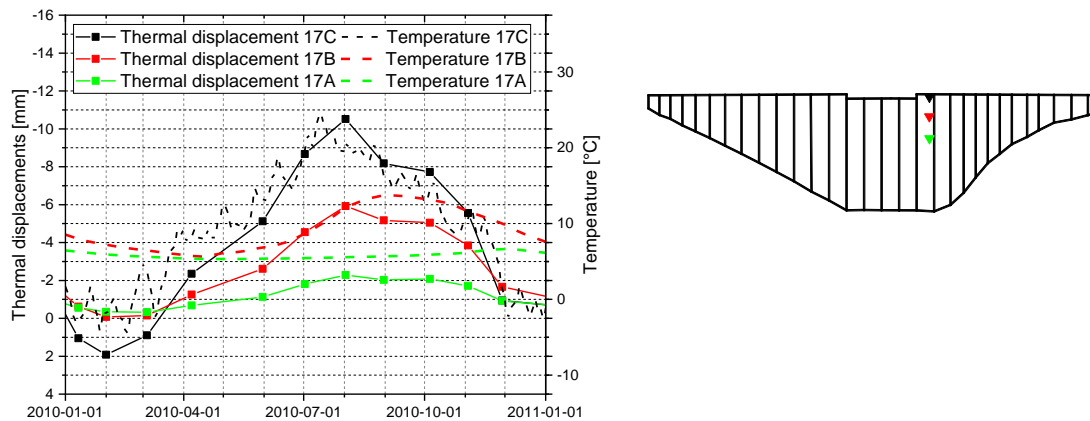


Figure 6.1: Time series of temperatures and thermal displacements at 17C, 17B and 17A

Regarding the time series of temperatures at 17C, 17B and 17A, both the magnitude and phase substantially vary between points. Specifically, for point 17C in the year of 2010, the temperature varies from  $-4.4\text{ }^{\circ}\text{C}$  to  $24.3\text{ }^{\circ}\text{C}$ , and the peak values occur in February and July, which is analogous with ambient air temperature; for point 17B, the peak values are  $5.6\text{ }^{\circ}\text{C}$  in April and  $13.7\text{ }^{\circ}\text{C}$  in September; while at 17A, there is a  $1.3\text{ }^{\circ}\text{C}$  temperature difference in the whole year period.

Regarding the time series of thermal displacements in Figure 6.1, the magnitudes vary substantially, but no phase shift is detected between the three points. The peak values of thermal displacement are reached at the same time for different points, where the minimum value occurs at the beginning of February and maximum value at the beginning of August. The variation range of thermal displacement at 17C is greatest among the three points, and the narrowest range is presented at 17A. The variation of thermal displacements slightly lags the temperature variation at 17C.

In summary, the magnitudes of temperature and thermal displacement decrease with the decrease of the point elevation. Despite the phase difference in temperature variation at these points, there is no phase difference between the thermal displacements. The variation of thermal displacement with time is not in coincidence with the variation of temperature with time at the identical point.

Figure 6.2 depicts the time series of thermal displacements at 17C and the mean temperature at the crown zone. A typical daily design temperature in a one-year period (shown in Figure 5.1) is specified as the boundary conditions. It is found that the variation of displacement at 17C in the upstream-downstream direction is in phase with the mean temperature value for the crest zone. The maximum/minimum displacement is obtained on the day when the mean temperature of the crest zone is maximum/minimum. The thermal displacement at one point in the dam is not determined by the temperature at a single identical point, but the temperature distribution around the investigated point.

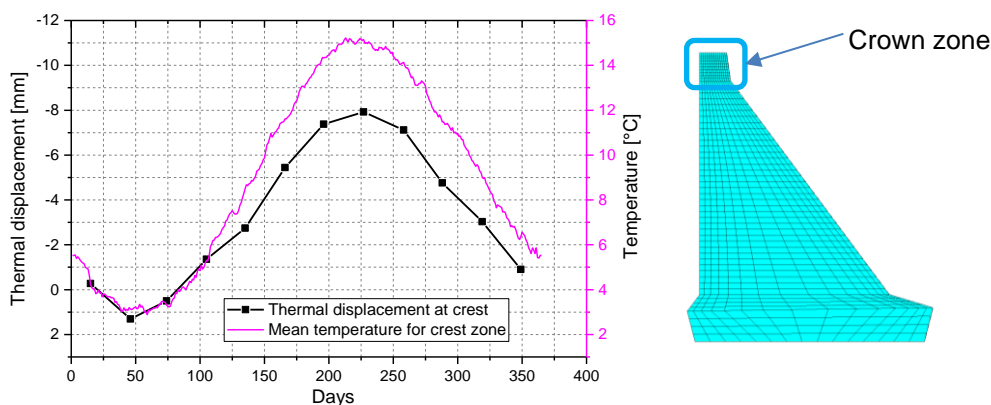


Figure 6.2: Time series of mean temperature for crown zone and thermal displacement at 17C

#### *Thermal responses in wintertime and summertime*

Figure 6.3 depicts the computed thermal response of displacements of the whole dam under temperature distributions within the dam, and the contours of horizontal displacements in the upstream-downstream direction are displayed for wintertime and summertime. The temperature distributions on 1<sup>st</sup> February 2010 and 2<sup>nd</sup> August 2010 are selected to represent wintertime and summertime respectively. It can be noticed that, in Figure 6.3 regardless of season, the most significant deformation occurs at the dam crown while the lower portion of the dam presents relatively lesser deformation. The blocks with spillway lower than the other blocks present slightly smaller thermal displacement towards downstream in wintertime. The maximum thermal displacement in winter is 2.17 mm at the crown towards the downstream side. Due to the influence of higher ambient temperatures in summertime however, the dam body tends to expand and show a deformation towards the water side. The displacement increases from the lateral block to central block and from the bottom of the dam to the top. The maximum thermal displacement in summertime reaches 11.54 mm at the crown towards the upstream side. The foundation part shows no deformation due to constant temperature assumption for this part.

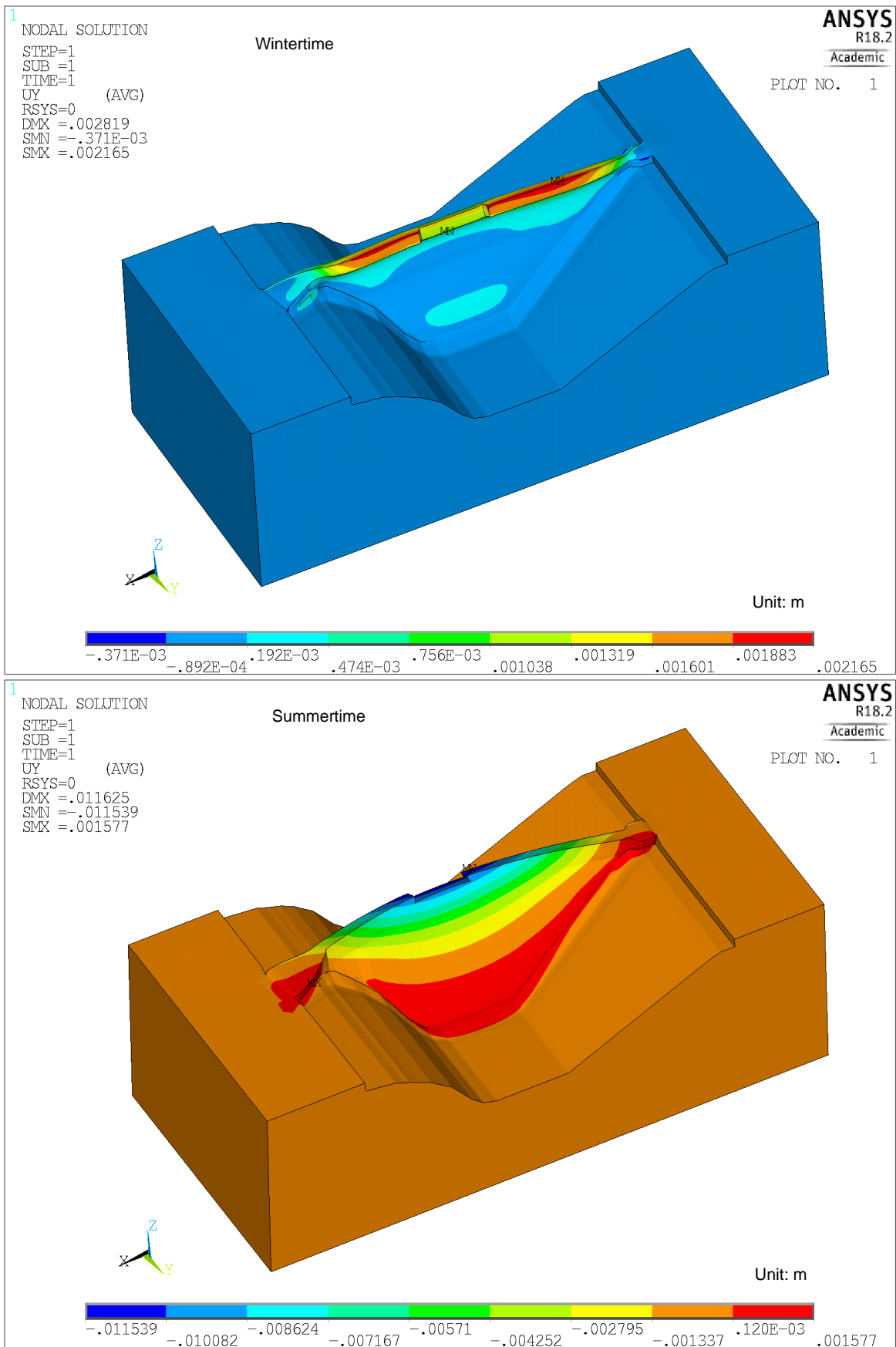


Figure 6.3: Contours of thermal displacement in upstream-downstream direction in wintertime and summertime

Figure 6.4 displays cross-section views of thermal responses for summertime and wintertime for central block 14, including temperature distribution and horizontal displacements in the upstream-downstream direction, and because the temperature at the foundation is assumed as constant values, the foundation part is not displayed. Figure 6.4 (a-1) and (b-1) shows that regardless of season, the higher temperature gradient is detected in the zone near the surface exposed to air and the crown of the dam. In wintertime, a nonlinear temperature distribution is presented, where the surface temperature is lower than the inner temperature and the highest temperature exists in the upper core part in the crown. While in summertime, the ambient temperature is warmer than the inner part, and there is no warm core inside the dam.

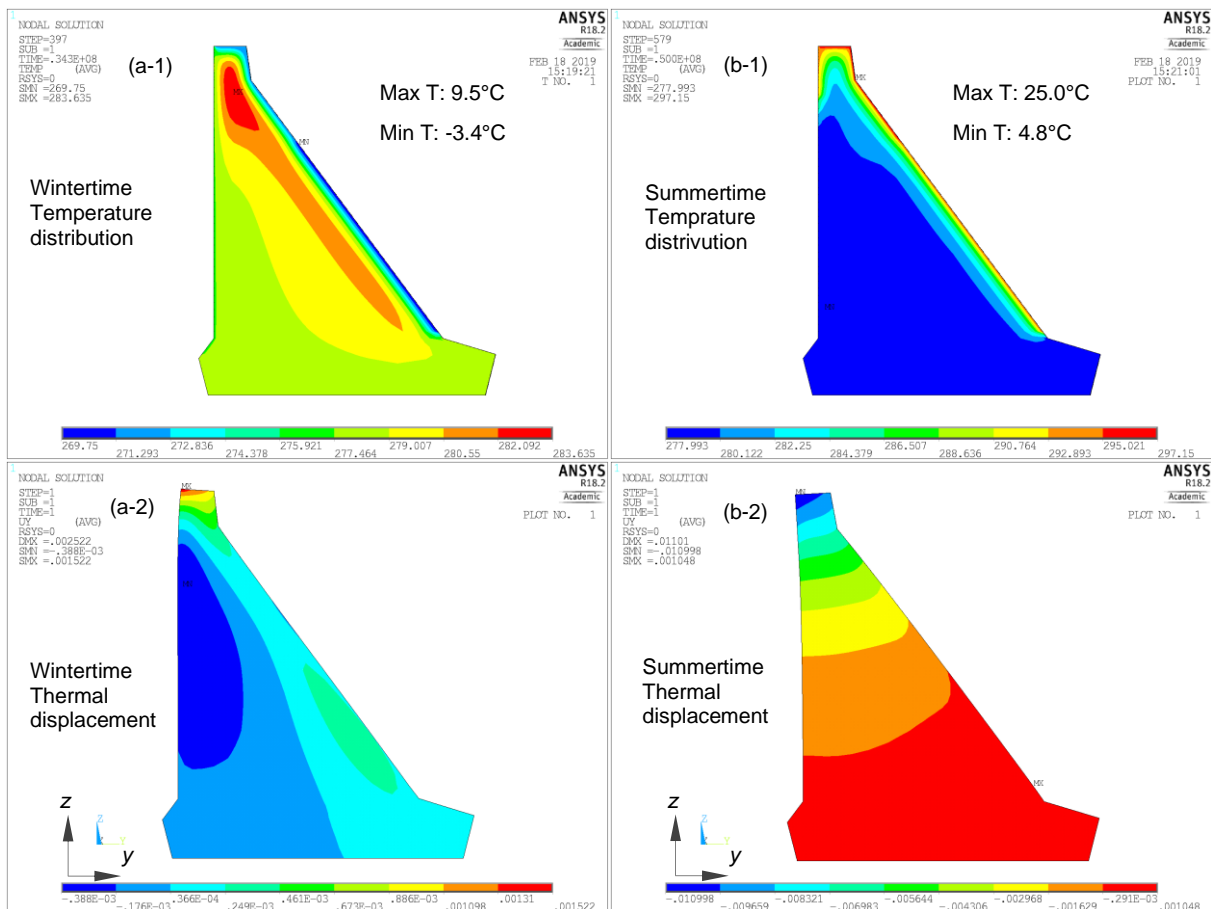


Figure 6.4: Thermomechanical response in wintertime and summertime

Regarding the thermal displacements in Figure 6.4 (a-2) and (b-2), a significant difference is shown between wintertime and summertime. In wintertime, the crown of the dam shows horizontally layered displacement characteristics and deforms towards the air side, and the maximum displacements occur at the top of the crown in the water side. In contrast, the rest of the dam shows quasi-vertically layered displacements from a cross-section view, the zone adjacent to the upstream face shows slight displacements towards the water side, and zero displacement exists in the quasi-middle vertical layer and dam heel, where the zone adjacent to the downstream face deforms towards the air side. In summertime, the whole dam shows



horizontally layered displacements, where the higher the layer, the larger displacement towards the water side.

### *Thermal responses at different elevations in the same block*

Because different thicknesses in upstream-downstream direction exist for different dam elevations, six paths at different elevations with corresponding thickness from 11 m to 65 m are chosen to investigate the influence of dam thickness on the thermal response. The elevation and the corresponding thickness are listed in Table E.1, and Figure 6.5 shows the computed temperature distribution for the paths at different elevations at the central block 14 in wintertime and summertime.

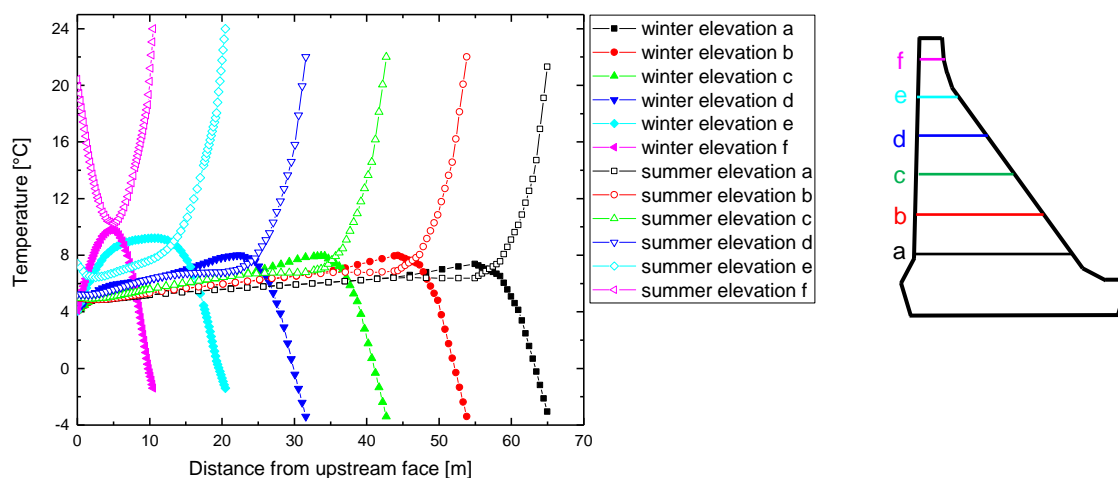


Figure 6.5: Computed temperature for wintertime and summertime at different elevations of block 14

All the temperatures begin from the same point at distance zero in wintertime, showing that the water-side temperature shows homogenous characteristics, while in summer the temperature values at distance zero are different, especially at elevations e and f. The temperature distribution across the thickness mostly depends on the water temperature on the upstream face, and only a certain depth from the downstream face is significantly influenced by the air temperature. Due to elevation and solar radiation for the 106 m high Rappbode Dam, the air temperature at the air side slightly increases from the dam toe to dam crown, which are represented by temperature values at the end points of each curve. At elevation a with a thickness of 65 m, the temperature presents a slight variation until about 8 m from the downstream inside the dam body, both in winter and summer, i.e., the ambient air temperature clearly influences the temperature distribution in the zone adjacent to the downstream face. When comparing the temperature curves in wintertime with summertime for the path at elevation f with a thickness of 11 m, the temperatures at the point located 5 m away from the upstream remain the same despite the different temperatures at the beginning and end points of the curve. Regardless of dam thickness, the ambient temperature influences only a certain

depth from the exposed surface; and in this certain depth the temperature varies with the ambient temperature, while the core area of the dam presents a relatively steady temperature distribution throughout wintertime and summertime.

The thermal displacements in the upstream-downstream direction for the paths at different elevations at block 14 are displayed in Figure 6.6. Comparing the displacements in wintertime with summertime at the same elevation shows that the displacements in winter are much smaller than those in summer. The positive direction is from upstream to downstream face (towards air side). The path at elevation f has the most significant change of thermal displacements from wintertime to summertime. Specifically, at the upstream face from 0.3 mm towards the air side to 8.5 mm towards the water side and at the downstream face from 0.5 mm towards the air side to 7.4 mm towards the water side. When comparing the displacements for different paths in summertime, the higher location presents a greater displacements value. Through the thickness from upstream face to downstream face, the thermal displacements in summertime tend to decrease, especially in the vicinity of surface exposed to air, corresponding to the air temperature influence depth from the downstream face. While the wintertime thermal displacements through the thickness tend to slightly decrease from the upstream face and then slightly increase in the air temperature influenced depth.

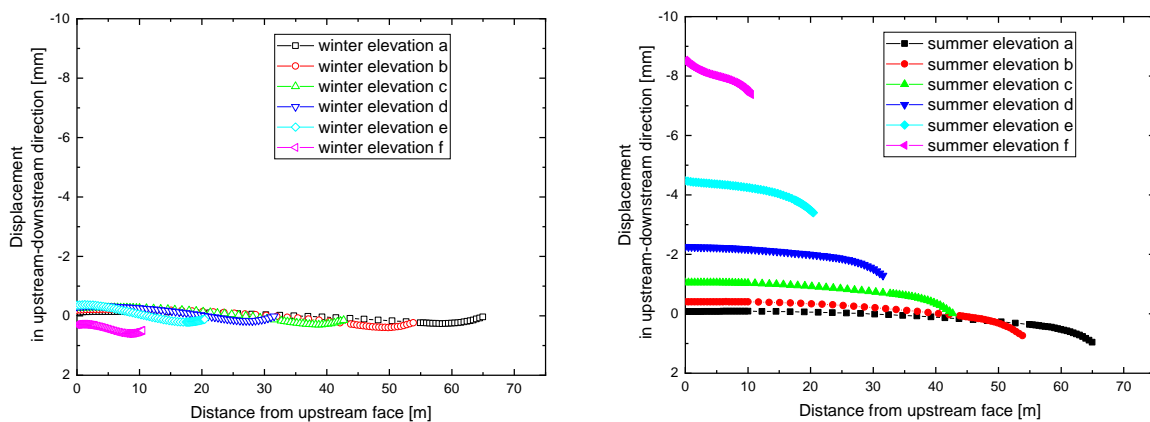


Figure 6.6: Computed thermal displacements of in wintertime and summertime at different elevations of block 14

Concrete gravity dams are often vulnerable to tensile stress under the load of temperature variation due to concrete's material characteristics. Figure 6.7 depicts the tensile stresses in the horizontal path at different elevations in wintertime and summertime due to thermal distributions within the dam body. The magnitude of these stresses in summer is generally smaller than those in winter, and the stresses demonstrate opposite characteristics across the thickness of the dam from the upstream face to downstream face for the two different seasons. In winter, the tensile stress at each elevation is greater in the vicinity of exposed faces (upstream face and downstream face) and near zero at the locations between. In summer

however, the tensile stresses are smaller in the vicinity of exposed faces but more significant at the locations between.

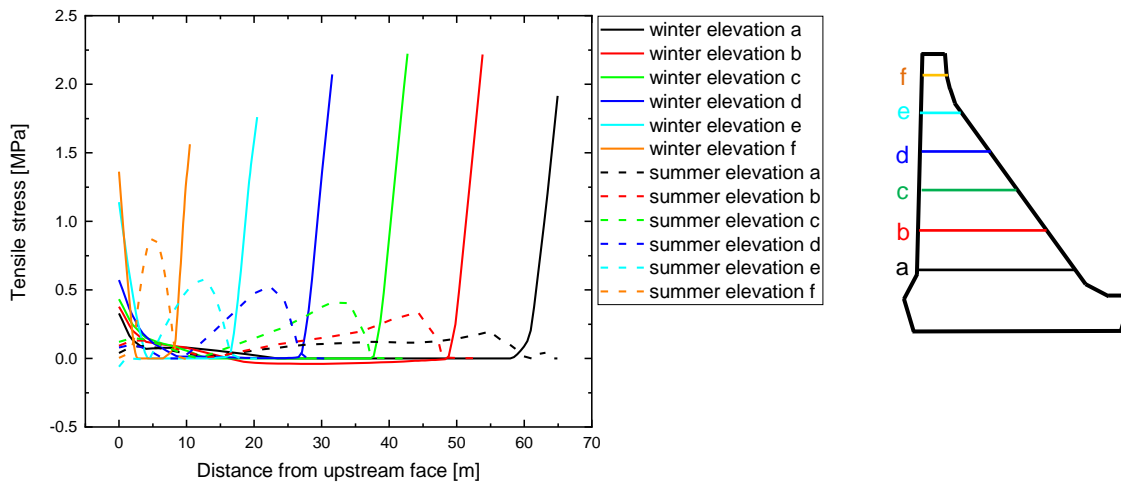


Figure 6.7: Tensile stresses in wintertime and summertime due to thermal load at different elevations of block 14

In wintertime, the internal temperature is nonlinearly distributed (as shown in Figure 6.4 (a-1)): and the temperature at the upstream face or downstream face is lower than the dam's inner temperature. The surface of the dam tends to shrink, which is restrained by the inner warm concrete, resulting in tensile stress in the vicinity of exposed surface and compressive stress in the interior, as shown in Figure 6.7. The greatest tensile stress occurs in winter at the downstream face of elevation b. The stress values here are all smaller than 2.5 MPa, which fall within the safe interval compared to the tensile strength of 2.9 MPa (seen in Appendix F) for the face concrete of Rappbode dam. Tensile stress cannot be avoided under ambient temperature variation, especially when the ambient temperatures considerably fall in wintertime.

#### *Thermal responses at different blocks at the same elevation*

Different blocks in the dam possess different heights from the bottom to the dam crown. To illustrate the influences of block height on the thermal responses, Figure 6.8 displays the temperature distribution, thermal displacement in the upstream-downstream direction and tensile stress in summertime at the same elevation for blocks 8, 11 and 14, the locations of which are shown in Figure 3.3. The heights of the blocks presented in Figure 6.8 are listed in Table E.2. The height of block 8 is the smallest and block 14 the greatest. The positive direction of the displacements is from upstream to downstream face.

Figure 6.8 (a) shows that the temperature values for the paths at the same elevation d for different blocks are identical. The temperature rapidly decreases from the downstream face to the point located 25 m from the upstream face, presenting a higher temperature gradient within

this influence depth of air temperature. In Figure 6.8 (b), the thermal displacement at elevation  $d$  for different blocks shows different values towards the water side in summertime. The greater the block's height, the greater the thermal displacement towards water side at the same elevation. However, the thermal displacement pattern through the thickness is analogous: increasing gradually from the upstream face to the downstream face and increasing faster in the vicinity of the downstream face where higher temperature gradient occurs. In Figure 6.8 (c), the tensile stress values show slight differences less than 0.1 MPa between different blocks. The peak value for block 8 is slightly smaller; however, the pattern of stress distribution through the thickness from the upstream face to the downstream face is the same for different blocks, where the lower stresses are found in the vicinity of the upstream and downstream face of the dam while the peak values of tensile stresses occur in between.

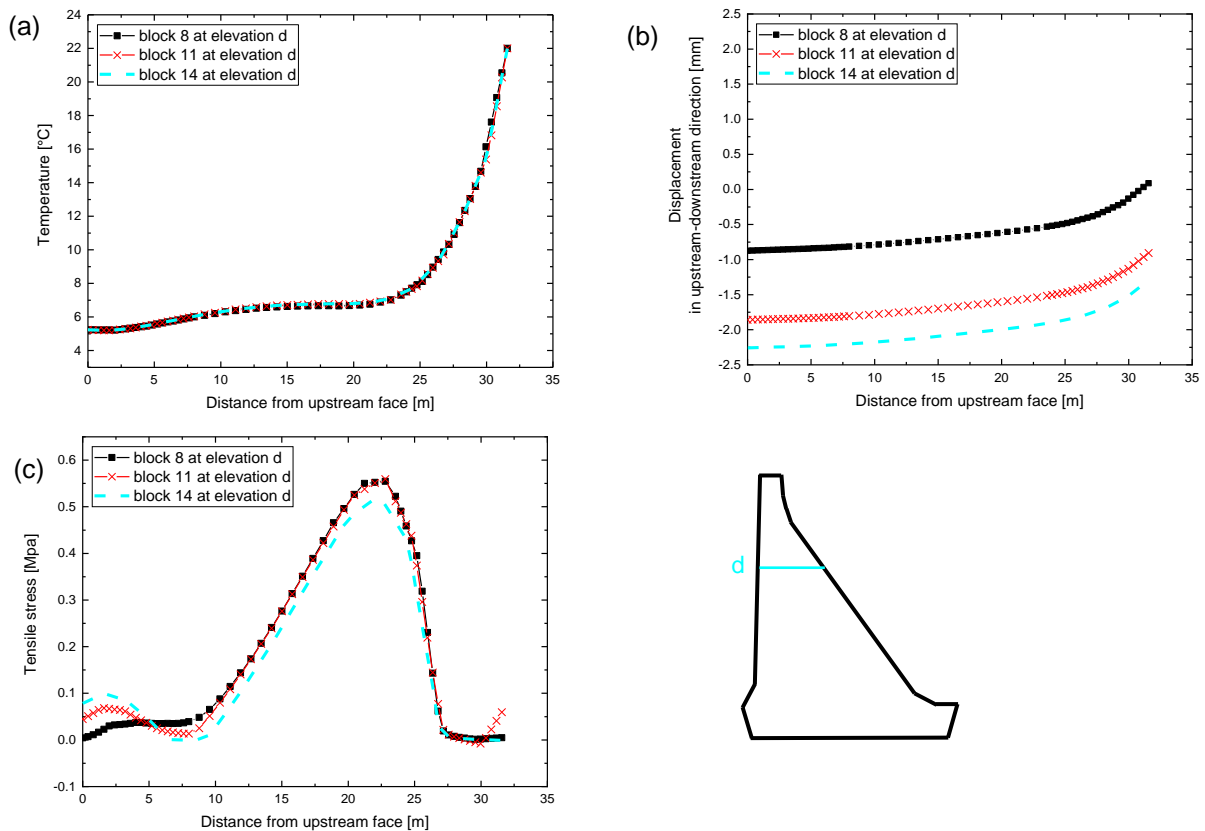


Figure 6.8: Thermal responses at elevation  $d$  in different blocks in summertime

By comparing the thermal responses of temperature, displacement and tensile stress for the paths at the same elevation in different blocks, analogous temperature distribution and stress distribution are presented, while different thermal displacement values results are presented due to the different heights of the blocks.

### 6.1.2 Simulation of unusual temperature situations

This section describes the simulation of thermal responses under unusual temperature conditions. Two unusual temperature scenarios are taken into account: one considers a

coefficient based on the daily design temperature illustrated in Section 5.1.1, while the other regards the temperature envelope throughout the recorded period of ambient temperature. The thermal displacements in the upstream-downstream direction as well as tensile stresses with a reference value of 5°C under two mentioned unusual scenarios are investigated by simulating unusual temperature situations.

### *Unusual temperature scenario I*

Unusual temperature scenario I in Figure 6.9 is defined based on the daily design temperature in a one-year period in Figure 5.1 by multiplying a coefficient. The median daily design temperature of 7.2 °C in Figure 5.1 is defined to be the fixed value and this daily design temperature is defined as the basic 'at'. As for the coefficients, the values of 1.5, 2, 2.5 are decided based on the consideration that the maximum range of the unusual temperature scenario I should inclusive the maximum (27.5°C) and minimum (-17.5°C) recorded air temperatures.

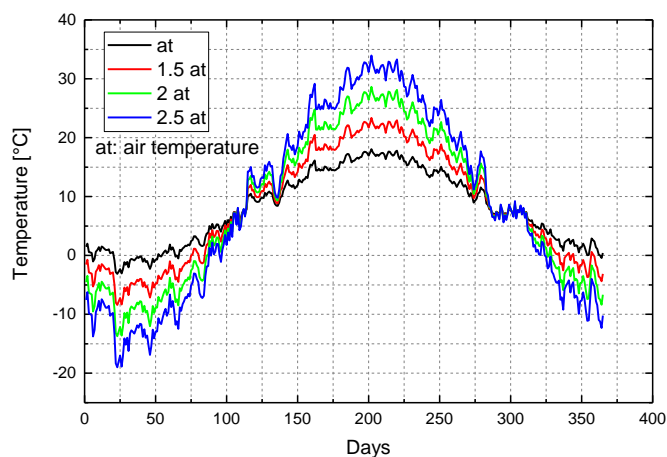


Figure 6.9: Unusual air temperature scenarios I in a one-year period

As for how to obtain the unusual temperature variation, take the dataset '2 at' for example: firstly, median (7.2 °C) in Figure 5.1 is subtracted from the daily design temperature; these new temperature values are then multiplied with the coefficient 2 to enlarge the variation range of the temperature; thirdly, the median 7.2 °C is again added to the enlarged variation range of temperature values, and the maximum value and minimum value for dataset '2 at' obtained are 28.7 °C and -13.7 °C respectively. For temperatures at the water side of the dam, the yearly design temperatures at the water side in Figure 5.1 are processed in the same way to acquire the corresponding wt1, wt2,... wt8 for unusual temperature scenario I. Thermal analysis is conducted in a one-year period, and the structural analysis is conducted at midmonth of the twelve months in the year to present the results of thermal displacements and tensile stresses.

Figure 6.10 displays the thermal displacements at a representative point 14C, which is the crown of the central block 14 of the dam in the upstream-downstream direction. Firstly, there is a similar time-varying tendency of thermal displacements under load condition of at, 1.5 at, 2 at and 2.5 at, and the time series presents no phase shift between each other. Secondly, around day 50, they reach the maximum positive displacement towards the air side, while around day 225, they attain the maximum negative displacement towards the water side. Between days 50 and 225, the thermal displacements gradually decrease, i.e., during this period, the dam deforms from the air side towards the water side. When comparing this tendency with the unusual air temperature variation in Figure 6.9, it is observed that the ambient air temperatures reach peak values around days 25 and 200. It can be concluded that the variations of thermal displacement of the dam lag the ambient air temperature around 25 days. When ignoring this time shift, the crown of the dam tends to move from the air side towards the water side with the increase of ambient air temperature. Thirdly, regarding the magnitude of the displacement variations, the peak to peak amplitude of thermal displacement under basic at is smallest ( $\approx 9$  mm); when the coefficient in unusual temperature scenario I increases from 1.5 to 2.5, the variation range of thermal displacement also increases; under an unusual load of 2.5 at, the peak to peak amplitude of thermal displacement reaches 23 mm, which is around 2.5 times the variation range of that under basic at. The thermal displacement rises proportionally with the defined ambient temperature.

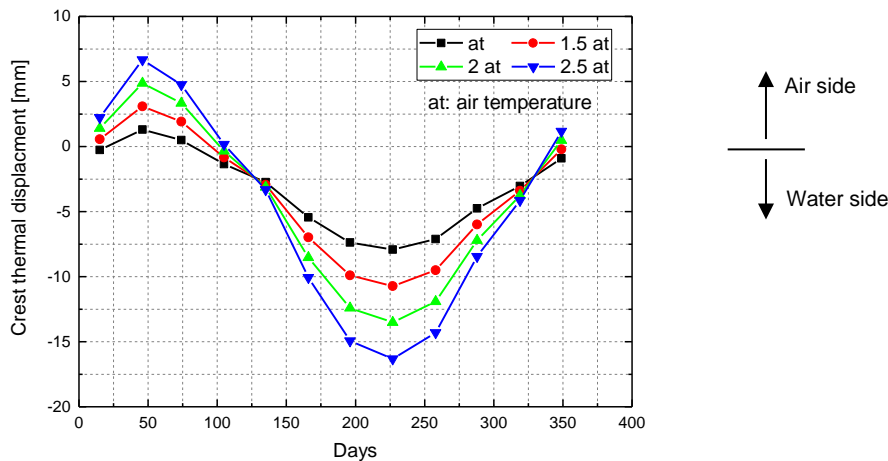


Figure 6.10: Thermal displacement at 14C under unusual temperature I

As already mentioned in Figure 6.7, the stresses at the downstream face at elevation b is the most significant among the chosen elevations. The point located at elevation b at the downstream face in block 14 is defined as the investigated point. Figure 6.11 depicts time series of tensile stresses at the investigated point under different assumed unusual temperatures. Firstly, the value of tensile stress is directly proportional to the assumed boundary temperature, and the increase and decrease tendencies of the tensile stresses under unusual temperature scenarios I present the same characteristics. Secondly, in the days

between 100 and 250, there are no tensile stresses at the investigated point, while the tensile stress at the investigated point are more significant the rest of the year. Thirdly, in the midmonth of February, the tensile stress reaches its peak value; when the unusual temperature is enlarged to '2 at', the tensile stress at this investigated point reaches 3.3 MPa, which exceeds the concrete tensile strength of 2.9 MPa (shown in Appendix F), which results in probable cracks at and around the investigated point.

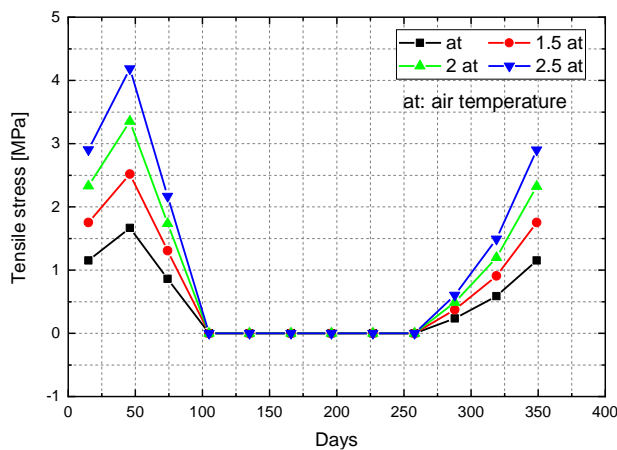


Figure 6.11: Tensile stresses at the investigated point under unusual temperature scenario I

#### *Unusual temperature scenario II*

Unusual temperature scenario II is defined based on the maximum and minimum recorded ambient temperatures. The daily maximal and minimal temperature values from the available data for a certain day in different years are chosen and constitute the maximum and minimum unusual temperature scenarios in one design year period.

The air temperature and ambient temperature at water side in different layers (defined in Section 4.1) for unusual scenario II are shown in Figure 6.12 and Figure 6.13 respectively, which show that the maximum and minimum unusual temperature formulate the top and bottom envelope curve of the ambient temperature respectively. For the air temperature, the maximum and minimum scenario reach the year's peak values in the same period. For the ambient temperature at the water side, neither the maximum nor minimum value in different layers are below 0 °C throughout the year. Regarding both the maximum and minimum scenarios, the same characteristics can be observed, which is that from days 1 to 365 in this design year period for two adjacent layers, the lower layer warms slower than the upper layer but cools together with upper layer after the upper layer cools to the temperature of the lower layer.

The thermal analysis for unusual temperature scenario II is firstly conducted in the one-year period, and the temperature distributions at every midmonth are specified on the model to



achieve the thermomechanical results of thermal displacements and tensile stresses at midmonth of the twelve months during the one-year period.

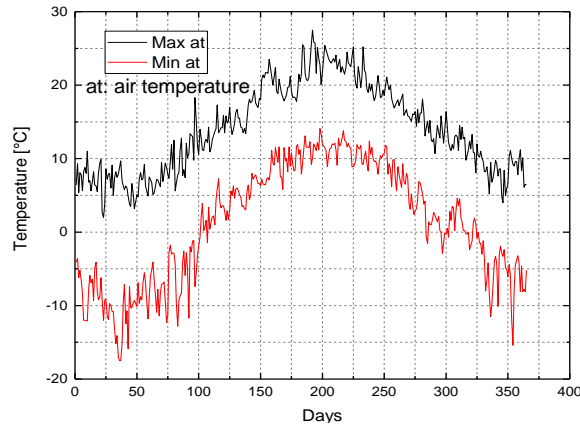


Figure 6.12: Air temperature for unusual temperature scenario II

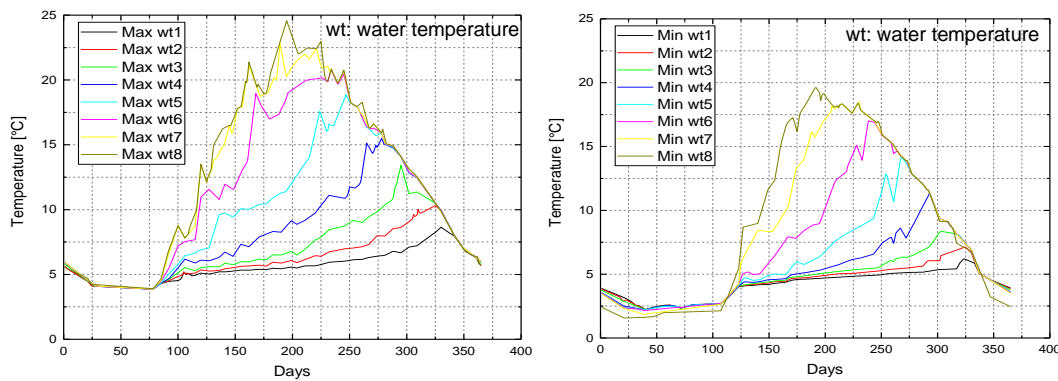


Figure 6.13: Ambient temperature at water side for unusual temperature scenarios II

Figure 6.14 illustrates the maximum and minimum envelopes of thermal displacements in the upstream-downstream direction at 14°C that are possible under unusual temperature scenario II. It is found that, firstly, the thermal displacements resulting from the minimum unusual temperature scenario are smaller than those from the maximum unusual temperature scenario. Secondly, the variation ranges of thermal displacements are comparable between these two scenarios, with the peak-to-peak variation about 10 mm for each of the cases. Thirdly, during the first 75 days of the year, the thermal displacements under these two scenarios show different tendencies, where the thermal displacement under the maximum temperature scenario increase towards the air side and decreases under the minimum temperature scenario, which is due to the difference between the assumed unusual air temperature during the first 50 days. Fourthly, for the period between days 75 and 365, the thermal displacements under two load conditions show the same variation tendency to first decrease and then increase. During this time period, the dam thus firstly deforms from the air side to the water side; however, the maximum displacements towards the water side are obtained at around day 225, and then the crown of the dam begins to move towards the air side.



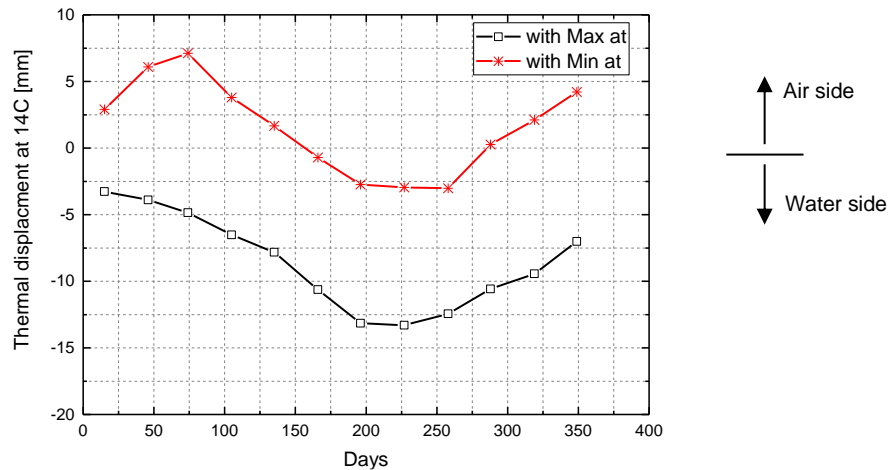


Figure 6.14: Thermal displacements at 14C under unusual temperature scenario II

The change in thermal tensile stress at the aforesaid investigated point is displayed in Figure 6.15. Great differences can be observed in tensile stresses resulting from the maximum and minimum temperature scenarios. With the maximum temperature scenario, the tensile stress at the investigated point is around 0 for the first eleven months and less than 1 MPa in December. However, with the minimum temperature scenario for the first three month of the year when the assumed air temperature decreases, the tensile stresses are greater than 3 MPa, exceeding the tensile strength of 2.9 MPa (seen in Appendix F); and then, at the midmonth of June to September, the tensile stresses return to 0 due to the higher ambient temperature before increasing again (but less than 2.9 MPa) from the midmonth of September.

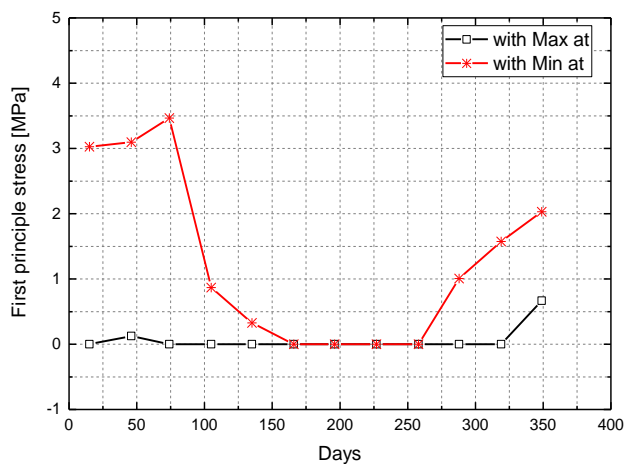


Figure 6.15: Tensile stress at investigated point under unusual temperature scenario II

In conclusion, the thermomechanical response is more significant in winter when the ambient environment is cold, which normally leads to the hazardous tensile stress at the face concrete of dams. Unusual temperature scenario I represents the enlarged variation of ambient temperature in a one-year period, which leads to the enlarged variation of thermal displacements and thermal stress. Unusual temperature scenario II represents unusual cold or warm ambient temperatures in a one-year period, and the results of corresponding thermal

displacements are analogous for cold and warm ambient temperature conditions, where the tensile stress is especially noticeable under the cold ambient temperature.

## 6.2 Structural displacements due to water level variation

To investigate the structural displacement of the dam under water level variation, both the usual and unusual water level variations are considered in the simulation. As already mentioned in 4.1.2, hydrostatic pressure as well as uplift pressure have a directional relationship with water level in the reservoir, and the self-weight is needed in the simulation to prevent the dam from floating away under the uplift pressure. This section includes calculations of displacement response of the dam under the loads of hydrostatic pressure, uplift pressure and self-weight. Questions like how the dam deforms when the water level increases or decreases, is the uplift pressure affects the dam deformation as significantly as the hydrostatic pressure at the upstream face, and whether the foundation is essential in the simulation of deformation behaviour will be answered in this section.

### 6.2.1 Response under usual water level variations

#### *Structural displacements at different elevations*

To survey the response of relative displacement under regular water level variation, the period of 2010 was selected to present the results. Figure 6.16 shows a comparison of the water level and response of relative displacement induced from water level variation in the upstream-downstream direction at locations 17C, 17B and 17A (shown in Figure 3.4). The positive direction of displacements is towards the air side and the water level varied between 412.87 m a.s.l. and 422.67 m a.s.l. in 2010.

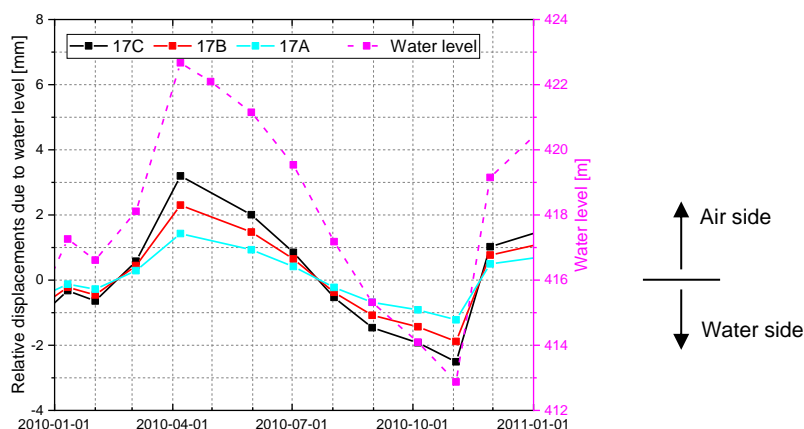


Figure 6.16: Time series of water level and relative structural displacement

It can be seen that, firstly, the variation of water level and the response of water level induced displacement fall into step with each other, whereby when the water level rises, the displacement increases (moves towards the air side). Secondly, the amplitude differs for

different investigated points 17C, 17B and 17A, where the higher the point, the greater the amplitude. Thirdly, the highest water level and corresponding largest displacement for each point in the window occurred in April, while the lowest water level and corresponding smallest displacement for each point occurred in November. The largest relative displacements for 17C, 17B and 17A correspond to 3.2 mm, 2.3 mm and 1.4 mm respectively, while the smallest relative displacements are -2.5 mm for 17C, -1.9 mm for 17B and -1.2 mm for 17A.

To show the difference of the displacement induced from water level variation at the upstream side and downstream side, comparisons are made to investigate the response of relative displacement on certain points located at each side. The time series of water level induced relative displacements at certain points are plotted in Figure 6.17. The points 14C and 14C-a are located at the same elevation, but one is at the upstream side and the other the downstream side, which also holds for points 14B and 14B-a, 14A and 14A-a.

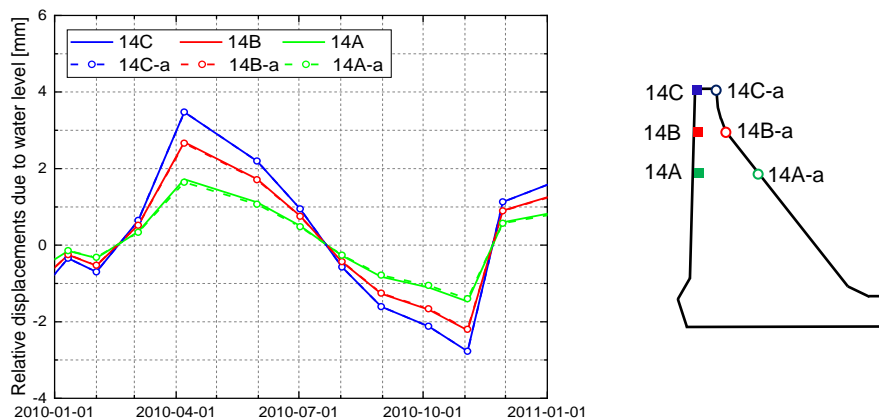


Figure 6.17: Comparisons of water level induced displacements at different points of block 14

It can be seen from Figure 6.17, all the variations of relative displacement fall totally into step and the relative displacements at the same elevation are comparable for the points located at the upstream side and downstream side. Specifically, for the points at elevation C, the relative displacements are identical for 14C and 14C-a, and the relative displacements at 14B and 14B-a are almost overlap for the points at elevation B. At elevation A, the relative displacement at 14A-a is slightly smaller than that at 14A. Under the hydrostatic pressure at the upstream face, the dam is minimally compressed along the thickness from upstream to downstream. Elevation A is always under the water table, and due to the contraction of the concrete, the relative displacement for the point at the downstream side is slightly smaller than that at the upstream side, but all differences stay within negligible ranges.

#### *Displacements at crown of different blocks*

A schematic drawing for the deformation of the dam under water load in Figure 6.18 illustrates that the central crown of the dam shows greater displacements than the lateral of the dam. From the top view of the dam, the dam crown forms a deflection curve as a simple supported

beam under a uniformly distributed load. Based on the assumed zero displacement restraints at the dam base in this model, the deformation is enlarged with increased water level. The dam crown is the most critical location for the water level variation induced displacement.

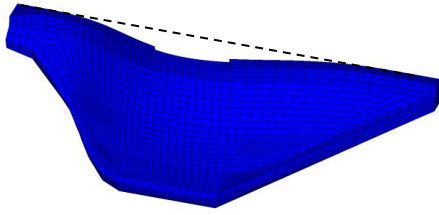


Figure 6.18: Schematic drawing of deformation of the dam due to water load (air side view)

The displacement values at the dam crown in the upstream-downstream direction are displayed in Figure 6.19 along with a compared time series of relative displacements and presentation of the mean value for each investigated point for the year 2010.

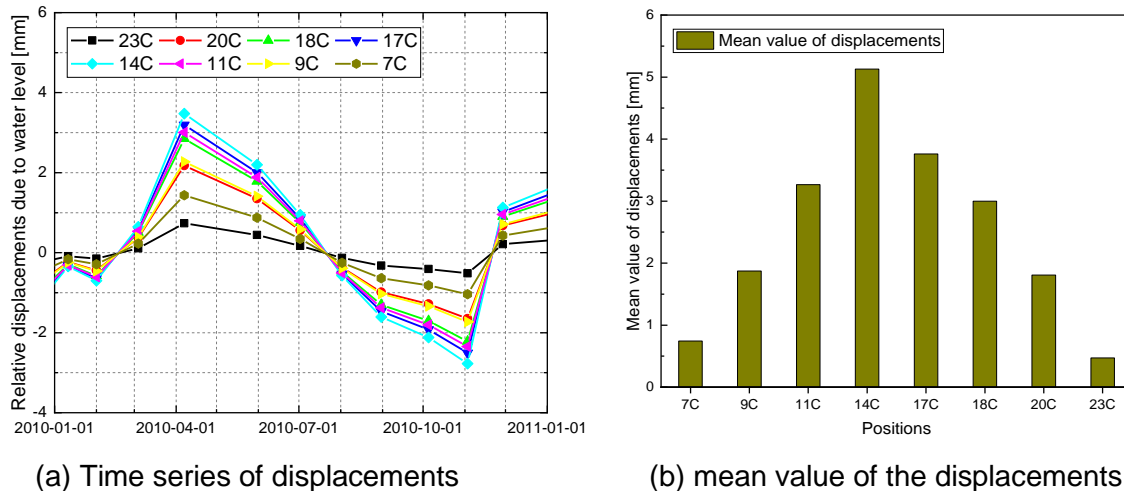


Figure 6.19: Water level induced displacements at crown of different blocks in 2010

Figure 6.19 (a) illustrates the time series of the structural displacements relative to the mean value. The locations of the different points seen in Figure 3.4. The variations of water level induced displacement are in synchrony, but the mean value of the displacement and amplitude for each location differ at different blocks. The largest variation for these locations exists at 14C located in the centre of the crown with a variation between 3.5 mm and 2.8 mm and a mean value of 5.1 mm, while the smallest variation occurs at 23C located at the right side of the dam from the water side view with a variation range between 0 mm and 1.2 mm and a mean value of 0.5 mm. It is found that, the order of the variation ranges of relative displacements is in coincidence with that of the mean values for different points, where the greater the mean value, the greater the variation range. In the order of 14C, 17C, 11C, 18C, 9C, 20C, 7C and 23C, these points' corresponding variation ranges of relative displacements decrease along with their corresponding mean values.

### 6.2.2 Response under unusual water level variations

As already mentioned in Section 3.3.1, the water level varied in previous years in a relatively narrow range of 25 m when compared with the reservoir depth of 89 m (shown in Section 3.1). In this section, the unusual water level involving the variation from 0 m (corresponding to 334.6 m a.s.l.) to 89 m (corresponding to 423.6 m a.s.l.) is simulated to check the displacement response.

To explore the displacement response quantitatively, the displacements in the upstream-downstream direction at representative point 14C are depicted in Figure 6.20. The results of displacement are shown for three different load cases: case 1 applies the hydrostatic pressure, uplift pressure at dam base and self-weight together on the model of the dam-foundation system; case 2 applies the hydrostatic pressure and self-weight together on the model of the dam-foundation system; case 3 applies the hydrostatic pressure and self-weight on the model without the foundation. As for the uplifting pressure applied in case 1, the theoretical uplift pressure with a reduction factor  $\eta$  of 0.85 is adopted for the simulation according to Figure 3.9. Regarding the constraints, zero displacement constraint is prescribed in all directions at the boundary of the foundation part for cases 1 and 2; for case 3, zero displacement constraint is defined in all directions at the base of the dam body.

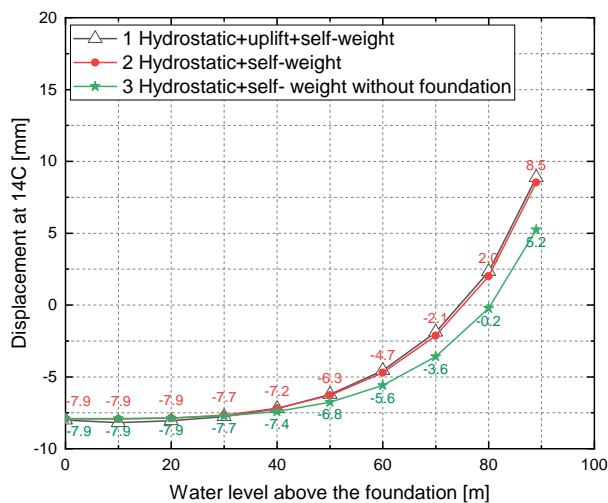


Figure 6.20: Displacements at 14C with unusual water level variation

As depicted in Figure 6.20, the results from the three cases begin from -7.9 mm when the water level is 0 m, which stems from deformation due to the self-weight of the dam, which means that with no water in the reservoir, the dam crown deforms towards the water side with 7.9 mm under its self-weight. Secondly, when comparing the results of cases 1 and 2, it turns out that with the increase of water level in the reservoir, the displacement curve of case 1 is almost overlapped with that of case 2, which means that uplift pressure minorly influences the displacement of this concrete gravity dam. Thirdly, under the load combination of hydrostatic

pressure, uplift pressure and self-weight, a displacement variation of 1.4 mm is obtained at point 14C when the water level rose from 0 to 50 m, while a variation of 14.8 mm occurred when the water level rose from 50 m to 89 m. Last but not least, differences can be detected for the model with and without the foundation by a comparison between cases 2 and 3; specifically, when the water level is lower than 40 m, the difference values are minimal, while more apparent differences could be observed when the water level exceeds 40 m in the reservoir. A water level of 70 m in the reservoir results in a difference of 1.5 mm between the two load cases, and a different value of 3.3 mm is obtained with the full storage of the reservoir.

The comparisons indicate that, the hydrostatic pressure at the upstream face is decisive in the investigation of displacement response of the dam due to water level variation; the uplift pressure at dam base plays a negligible role; the foundation part should be taken into consideration together with the body of the dam in the simulation.

### 6.3 Simultaneous displacements due to water level and temperature variation

In the simulation of deformation behaviour due to time-varying temperature distribution and variation of water level, the time series of computed simultaneous displacements are compared with those of measured displacements firstly. The structural displacement induced from water level variation and thermal displacement induced from temperature distribution within the dam body are then compared with the computed simultaneous displacement to comprehend the weightiness of a single variable on the displacement distribution. Lastly, an example of an unusual load case is considered to investigate the response of displacements and to predict the health state of the dam under this load case.

#### 6.3.1 Simultaneous displacements based on ANM

In this section, simulations of deformation behaviour under ambient temperature and water level variations are conducted to obtain simultaneous displacements, which can be used to evaluate the plausibility of this ANM. In the evaluating process, the evaluating method is introduced at first, and then, the performance of the ANM is evaluated.

Thermal-structural coupled analyses are adopted in this simulation, as shown in Section 4.1. The unit system is listed in Table 4.2 and the material properties in Table 4.3, Table 4.4 and Table 5.2. The FE model for the transient thermal and structural analyses can be seen in Section 4.3.4.

The calculation procedure is as follows:

- a) Transient thermal analysis is firstly conducted to acquire the temperature distribution over the whole dam on the displacement recorded date during the calculation period. The initial condition adopts the specified approach presented in Section 5.1 and boundary conditions in Figure 5.8.
- b) Structural analyses are performed for displacements' recorded dates by imposing the hydrostatic pressure on the upstream and corresponding uplift pressure at base of the dam, self-weight and temperature distribution within the dam body at all nodes. The displacements at measurement points can then be selected from the simulation results.

In order to investigate the displacement variations, each dataset from the computation for one measurement point is processed by removing the mean value of the identical set, like the way to process the measurements in Section 3.4.2. This data-processing approach is adopted for the purpose of obviating the permanent displacements and focusing on the variations of the displacements. Finally, performance evaluation of this ANM can be done by means of conducting comparisons between computed displacements and a whole string of measured displacements for the measure locations described in Figure 3.4.

In evaluating the performance of the model, the computed and measured results are firstly plotted together to provide a visual inspection of the performance of this model. This time series comparison enables showing the presence of potential outliers of measured or computed values. Second, the coefficient of determination or R-square is adopted to indicate the goodness-of-fit of the ANM (Ritter et al., 2013). The general definition of the indicator is:

$$R^2 = 1 - \frac{\sum_{i=1}^N (O_i - P_i)^2}{\sum_{i=1}^N (O_i - \bar{O})^2} \quad (6.1)$$

where  $P_i$  - single computed value;

$\bar{O}$  - mean value of measured values;

$O_i$  - single measured value;

$N$  - number of measured values.

$R^2$  is a dimensionless indicator of the percentage of total variation of the measured data described by the computed data. The range of this indicator is  $[0, 1]$ , where the higher the better. For example, in statistical meaning, where  $R^2 = 1$  indicates a perfect fit, i.e., 100% of the variation could be described by the computation model.

The criteria for evaluating the model performance using  $R^2$  are shown in Table 6.1 (Ritter et al., 2013).

Table 6.1: Criteria for goodness-of-fit evaluation

Performance rating	Value of $R^2$
Very good	$\geq 0.900$
Good	0.800 – 0.899
Acceptable	0.650 – 0.799
Unsatisfactory	$< 0.650$

*Comparison between the computed values with measured values*

A whole string data of the measured and computed upstream-downstream relative displacements under self-weight, hydrostatic pressure, uplift pressure, air temperature and water temperature for the measurement points at middle-located block 14 (seen in Figure 3.4) is shown in Figure 6.21.

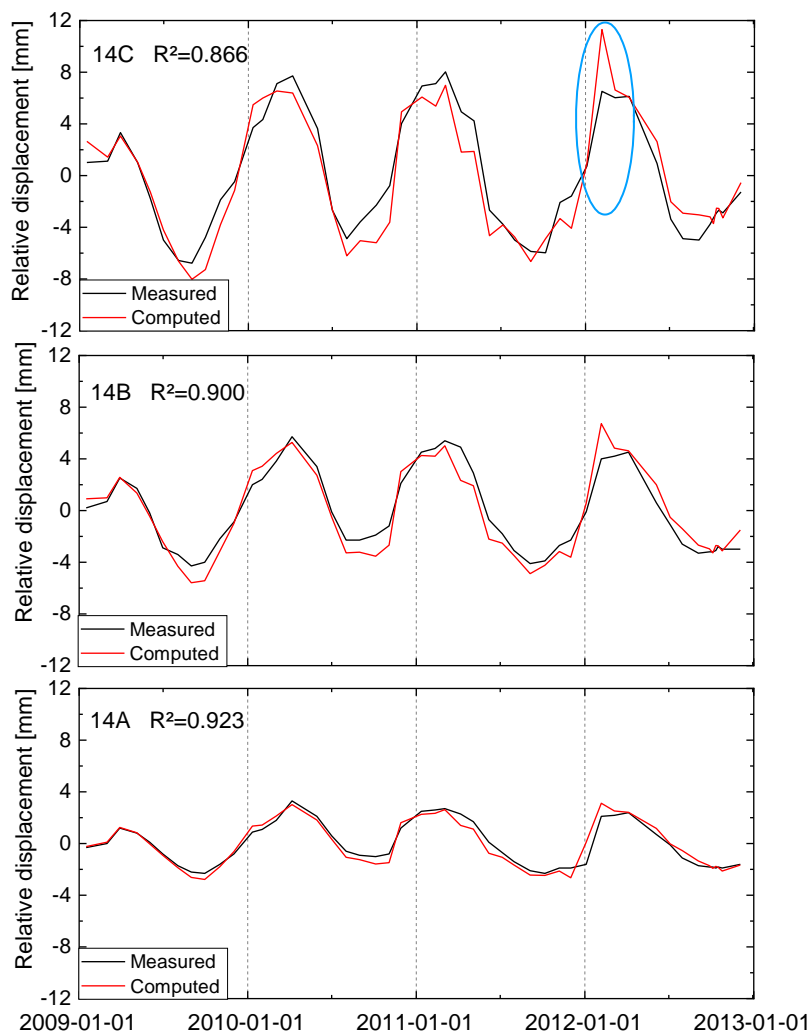


Figure 6.21: Comparisons between computed and measured relative displacements in upstream-downstream direction at 14C, 14B and 14A



In accordance with the period of temperature distribution results in Section 5.2.2, the time period from 2009 to 2012 is taken into consideration to display the results. Firstly, regarding the increase or decrease tendency, the computed displacements at 14C, 14B and 14A are in accordance with the measurements overall, and present clear seasonal periodicity. Secondly, according to the performance criteria in Table 6.1, the evaluation values of  $R^2$  provide a performance rating of good at 14C and 14B and very good at 14A. Despite the similar increase and decrease tendency, a displacement drift (which is discussed later in this section) occurs in February 2012 for point 14C and diminishes from point 14C to 14A. The largest positive relative displacement (movement towards the air side of the dam) at 14 C is 11.3 mm in February 2012, while the largest negative relative displacement (movement towards the water side of the dam) is 8.1 mm in September 2009. The maximum and minimum relative displacements for point 14B are smaller presenting 6.6 mm and 5.7 mm respectively. For point 14A, the variation range of relative displacements is even tiny. With an amplitude decay, the displacement responses at 14B and 14A present a better value of  $R^2$  than that at 14C. At point 14C, the value of  $R^2$  is 0.866, i.e., 86 % of the variation of measured displacements at this location can be presented by the simulation based on ANM.  $R^2$  is 0.900 and 0.923 for 14B and 14A respectively.

Figure 6.22 depicts the comparison of values of  $R^2$  for each year from 2009 to 2012 and for the total four years displayed in Figure 6.21 for points 14C, 14B and 14A. The values of  $R^2$  indicate better alignments between computed and measured displacements in 2009 and 2011 for each point of 14C, 14B and 14A than those in 2010 and 2012. Due to the difference between the computed and measured values in the second half of 2010 and the drift in 2012 shown in Figure 6.21, the  $R^2$  values for these two years presented in Figure 6.22 are smaller. The values of  $R^2$  for 2009-2012 are in between. For point 14C with a displacement drift in February 2012, the  $R^2$  for 2012 presents the rating of acceptable with a value of 0.789. For points 14B and 14A,  $R^2$  at the year 2012 show better results since the drift in February 2012 diminishes for points 14B and 14A, which is in accordance with the time series comparison in Figure 6.21.

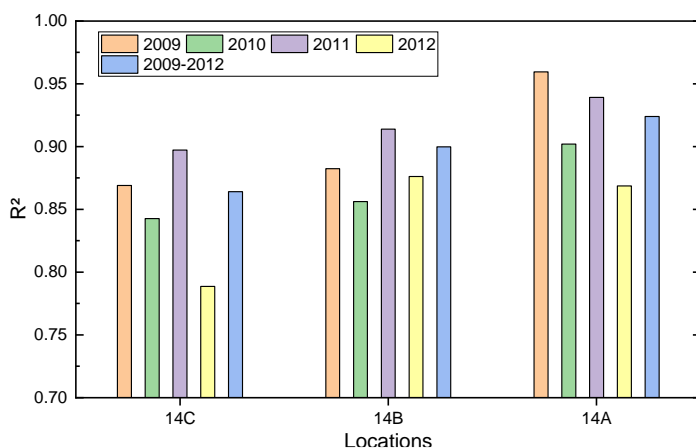


Figure 6.22:  $R^2$  for points 14C, 14B and 14A

As already stated in Section 3.4.1, the dam crown is more significant than other locations in terms of variation range of relative displacements. Figure 6.23 displays comparisons between the computed and measured relative displacements in the upstream-downstream direction at the crown of the instruments' installed blocks. Two graphics in the same row present results of blocks located at quasi-symmetrical positions, where the magnitudes of displacements variation ranges are comparable with each other. Displacement drift in February of 2012 can be detected for all the measurement points at the crown. Except for this displacement drift, the computed relative displacements are aligned with the corresponding measurements in terms of time series comparisons which show the same variation trend and seasonal variation cycle despite minor differences in values. The increase and decrease tendency of the relative displacements for different points are highly similar and differ only in magnitude. From the first to the fourth row, the graphically presented block tends to be increasingly further from the middle of the dam, while the magnitude of the displacement tends to decrease. The most significant displacement variation occurs at 14C, and the smallest displacement variation at 23C (shown in Figure 3.4), with the largest positive relative displacement of 2.2 mm and negative relative displacement of 2.4 mm. As for  $R^2$ , most points show values that greater than 0.750, except for points 11C and 7C with values of 0.734 and 0.741 respectively. Based on the evaluation criteria in Table 6.1, the values of  $R^2$  for the measurement points located at the crown demonstrate an acceptable to good goodness-of-fit.

Comparisons between the computed and measured displacements at elevations B and A for different blocks are displayed in Appendix G along with a good alignment at each measurement point.

A bar chart of the evaluating parameter  $R^2$  for the 25 measure points is depicted in Figure 6.24, and these points' locations are shown in Figure 3.4. Based on the criteria stated in Table 6.1, the goodness-of-fit rating presented by the values of  $R^2$  ranges from acceptable to very good. For points at elevation C, the performance rating of good is shown at 14C, 17C and 18C, while others show a rating of acceptable; for elevation B, most points show a rating of good, while the performance rating of very good occurs at most points at elevation A.

The performance rating presented from points at elevation C is not so good as that from the points at elevations B and A, possible reasons for which are as follows: firstly, elevation C is higher and its displacement variation is greater than that of lower elevations. Secondly, the crown of the dam is relatively thinner than the lower part of the dam and is more prone than the lower part to influence from the external environment including wind, ice, water waves, ambient vibrations etc. Thirdly, the load step of one day for the ambient temperature is adopted in the thermal analysis, and the diurnal temperature variation is not considered.

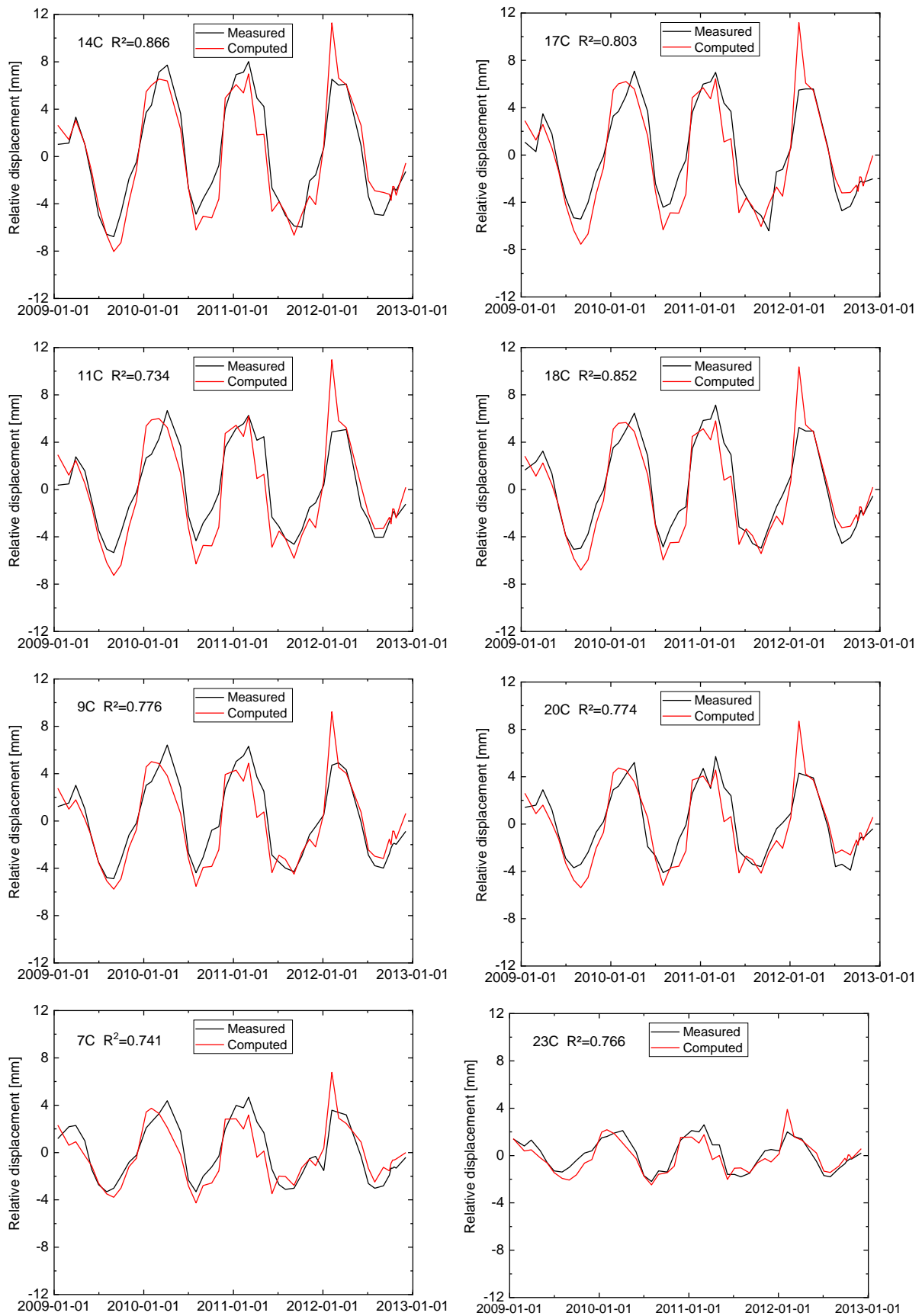


Figure 6.23: Comparisons between computed and measured relative displacements in upstream-downstream direction at dam crown

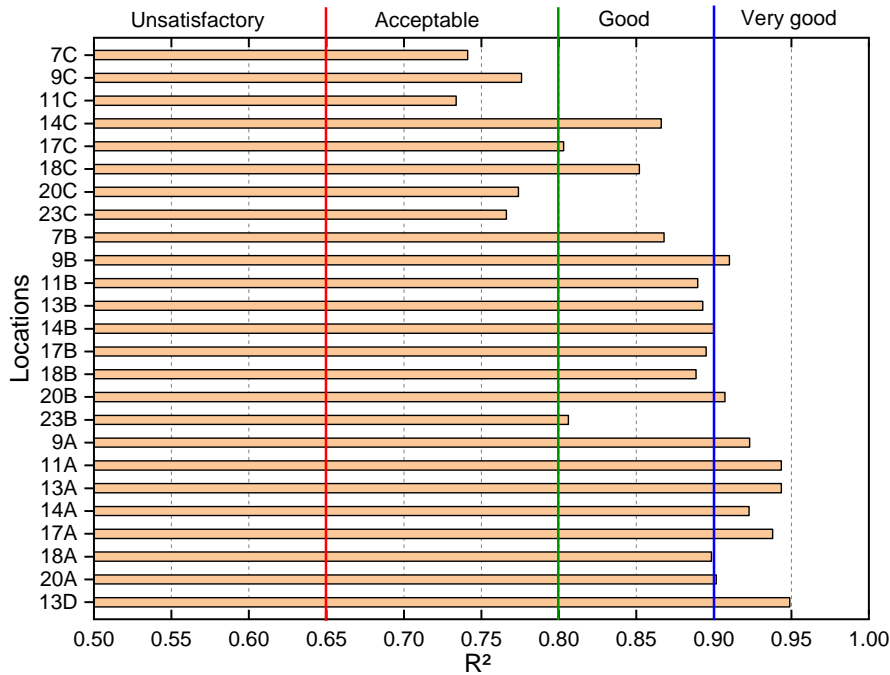


Figure 6.24: Goodness-of-fit evaluation of computed values

#### *Investigation of the drift*

As mentioned, when comparing the computed values with the measured values, a displacement drift was detected on 6<sup>th</sup> Feb. 2012, especially for the measurement points at the crown. The drift presents a dramatic difference between the computed and measured values and the computed values are greater than the measured values. This difference is caused by errors in either computed or measured values, and errors in measured values are not easy to be traced back. The possible error in computed values could be from the input data, specifically, the specified external loads, which originated from the monitoring data of the ambient environment.

Checking the input data of the external load, including the hydrostatic pressure, uplift pressure, air temperature and water side temperature, it is found that there is a 10-day information gap of air temperature in the time period from 20<sup>th</sup> Jan. 2012 to 29<sup>th</sup> Jan. 2012. For the input air temperature data, a linear interpolation was assumed to bridge the information gap in former simulation. In consideration of the time shift between thermal displacement and ambient temperature, the drift in February 2012 could represent the consequence of the assumed temperature data in the information gap, which cannot present the reality of the air temperature during this time period.

Consequently, investigations are made to check the response of displacements based on different assumed air temperatures proposed during the 10-day gap. In Figure 6.25, the black line shows the recorded air temperature but is missing the 10 days late January 2012; variations are proposed as assumed air temperatures 1 (red line) and 2 (green line) to bridge

this information gap. The red line represents a plain linear interpolation between the two recorded values to present the assumptions in the former simulation, while the green line came from the recorded values of the same period during other years. The green line indicates a firstly increasing and then dramatically decreasing temperature variation, and the mean value of assumed air temperature 2 is significantly greater than that of assumed air temperature 1.

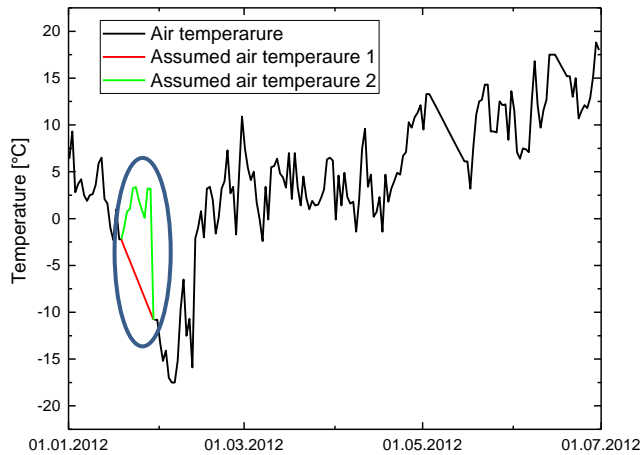


Figure 6.25: Time series of air temperature with assumed variations in the gap

Thermal analysis is conducted with a time step of one day during the first half of 2012, and then the temperature distribution on displacement recorded dates is chosen for the structural analyses. Comparisons between the measured and computed values from the two different assumed air temperatures in information gap are carried out and the results of relative displacements in a six-month window are illustrated in Figure 6.26. The results at two measurement points 14C and 14B are displayed as representative. Differences in relative displacement values on 6<sup>th</sup>, Feb. 2012 can be noticed firstly, and better alignment is achieved when computing the results with assumed air temperature 2 for the information gap. In Figure 6.26 (a), a relative displacement of 11.3 mm on 6<sup>th</sup> Feb. 2012 is obtained at measuring point 14C when using the assumed air temperature 1, while a value of 8.0 mm is obtained under assumed air temperature 2, which is closer to the measured value of 6.5 mm. Likewise, in Figure 6.26 (b), an improvement of 2.1 mm at measuring point 14B is presented when computing the relative displacement under assumed air temperature 2.

Examining the drift can help explain the improvements from assumed air temperature 2. As shown in Figure 6.23, the computed values are larger (too much more towards air side) than the measured values at drift point and the dam deforms towards the water side with temperature increases, as mentioned in Section 6.1. Therefore, compared with the former assumed air temperature 1, the assumed air temperature 2 in the information gap which represents the increased temperature can reduce the difference between the computed and measured values on 6<sup>th</sup> Feb. 2012.

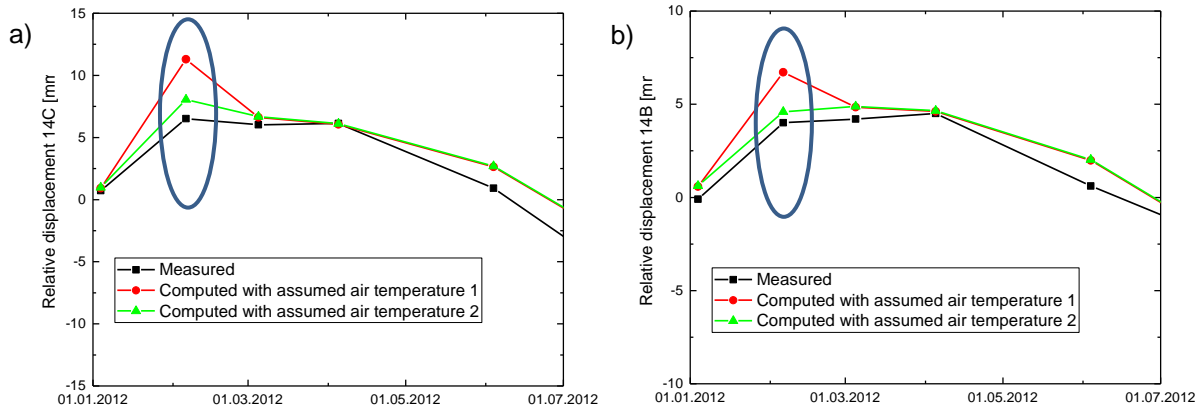


Figure 6.26: Comparison of relative displacements with two different assumed temperatures in the gap

Based on the analysis above, the assumed air temperature in the vacancy of 10 days significantly influences the deformation behaviour in the following days. The model is thus sensitive to the load specified, and uncertainties due to a 10-day information gap in air temperature can induce imprecise displacement responses.

### 6.3.2 Relationship between structural/thermal and simultaneous displacements

Due to the superposition principle assumption, the relative displacement due to ambient temperature and water level equals the sum of the water-level-variation-induced and ambient-temperature-variation-induced relative displacement, which can be expressed by the general equation:

$$D_{t+w} = D_t + D_w \quad (6.2)$$

where  $D_{t+w}$  - the relative displacement due to water level and temperature variation;

$D_w$  - the relative displacement due to water level variation;

$D_t$  - the relative displacement due to ambient temperature variation.

This verified ANM enables checking the correlation between  $D_t$  and  $D_{t+w}$  as well as  $D_w$  and  $D_{t+w}$ .

#### Correlation calculation

In the correlation analysis, the Pearson correlation coefficient  $r$  is adopted to measure the linear correlation between two continuous variables. Given paired data  $\{(x_1, y_1), \dots, (x_n, y_n)\}$  consisting of  $n$  pairs,  $r$  is defined as:

$$r = \frac{\sum_{i=1}^l (x_i - \bar{x})(y_i - \bar{y})}{\sqrt{\sum_{i=1}^l (x_i - \bar{x})^2} \sqrt{\sum_{i=1}^l (y_i - \bar{y})^2}} \quad (6.3)$$

where  $x_i, y_i$  - individual sample points indexed with  $i$ ;

$\bar{x}, \bar{y}$  - mean value;

$l$  - number of pairs.

This indicator  $r$  ranges from -1 to 1 and is used to quantify the degree to which two variables are related or how much one variable change when the other one does. The values of 1 or -1 indicate that a linear equation could perfectly describes the relationship between two variables, while a value of 0 implies that the relationship of two variables cannot be expressed using linear correlation (Rodgers & Nicewander, 1988).

$r_t$  describes the correlation between  $D_t$  and  $D_{t+w}$ , and  $r_w$  describes the correlation between  $D_w$  and  $D_{t+w}$ .  $r_t$  and  $r_w$  can be calculated based on Equation (6.3). In Figure 6.27, the values of  $r_t$  and  $r_w$  are displayed with histograms for each measurement point, and diagrams of the location of each point are shown in Figure 3.4. Firstly, by comparing the values of  $r_t$  and  $r_w$  for an identical point, in terms of weightiness of  $D_t$  and  $D_w$  for different suspension groups, general conclusions can be drawn as follows:

- Displacement at suspension C:  $D_t$  dominate
- Displacement at suspension B:  $D_t$  dominate, but less significant
- Displacement at suspension A&D:  $D_w$  dominate

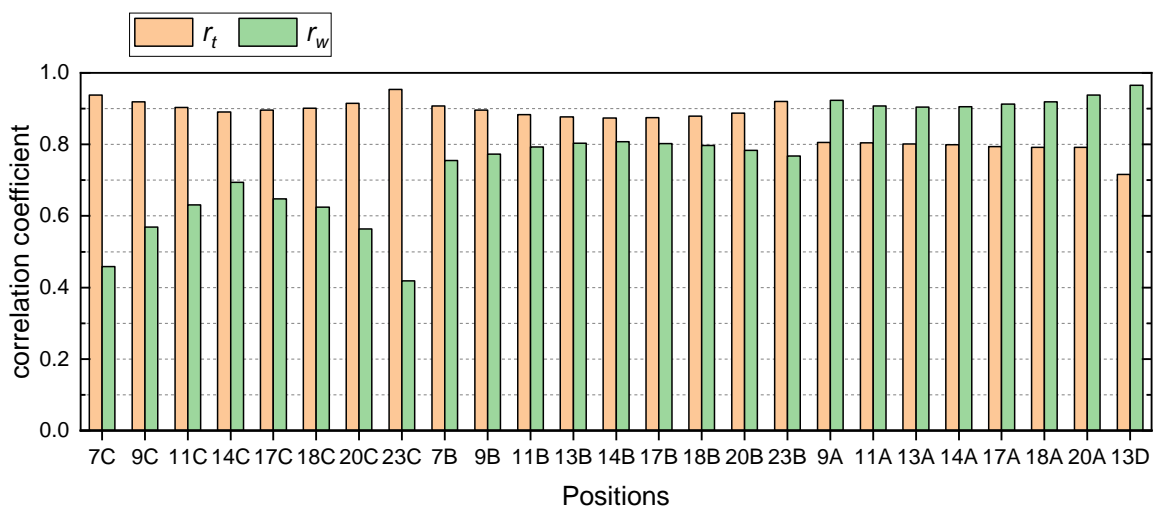


Figure 6.27: Values of correlation coefficient  $r_t$  or  $r_w$

This means that for the points at the crown (with an elevation of 426.4 m a.s.l.), the temperature dominates the deformation behaviour; with the decrease of elevation, the water-level-induced displacement becomes increasingly significant; for the point at elevation B (408.5 m a.s.l.), the temperature plays a little bit greater role than water level in the deformation behaviour; however, the water level began to dominate the displacement when it decreased to the elevation of elevations A (390 m a.s.l.) and D (370 m a.s.l.).

Secondly, the values of  $r_t$  or  $r_w$  are compared for the points at the same elevation, which shows that for points at suspension C or B,  $r_{t,middle} < r_{t,side}$  and  $r_{w,middle} > r_{w,side}$ , but this trend is more obvious for points at suspension C than B. For points at suspension A,  $r_{t,middle}$  and  $r_{t,side}$  stay almost the same value, and  $r_{w,middle}$  is slightly smaller than  $r_{w,side}$ . This means that for the upper part of the dam, the domination of temperature is more significant at side blocks than middle blocks; in contrast, for the lower part of the dam, the domination of water level in deformation behaviour is clearer at blocks at the side than in the middle.

#### Comparison of time series

Further comparisons of the time series of  $D_t$ ,  $D_w$  and  $D_{t+w}$  are conducted, and the results of two measurement points 14C and 14A (locations seen in Figure 3.4) are shown in Figure 6.28 to investigate the phase differences between different items and in Figure 6.29 to investigate the quantities of different items.

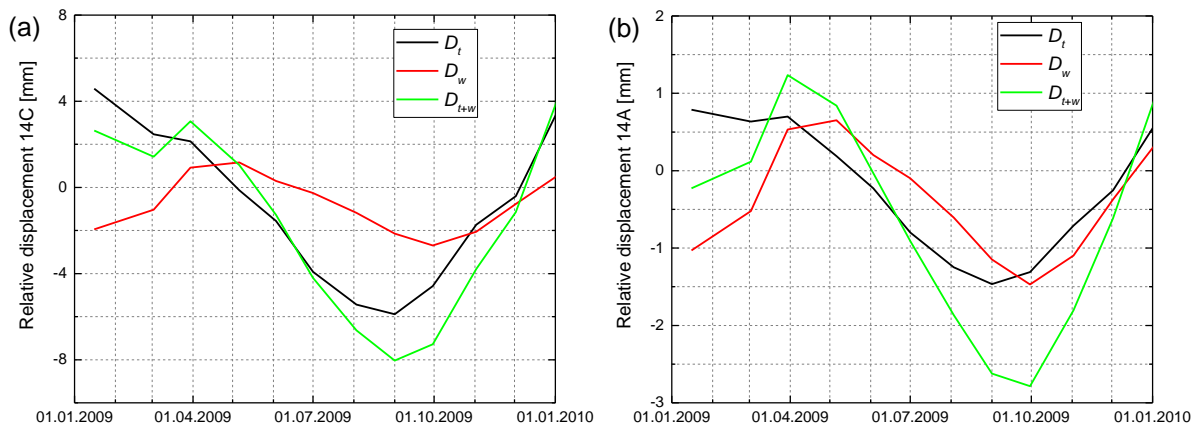


Figure 6.28: Comparisons of time series between  $D_t$ ,  $D_w$  and  $D_{t+w}$

Figure 6.28 shows that for point 14C, the phase position of  $D_{t+w}$  is closer to that of  $D_t$ , while  $D_w$  presents a phase delay compared with that of  $D_{t+w}$ . For the measurement point 14A however, the variation of  $D_{t+w}$  illustrates the same phase position with  $D_w$ , and the phase position of  $D_t$  is ahead of the phase position of  $D_{t+w}$ .

Figure 6.29 shows that the quantity of each item in the identical month is smaller at 14A in Figure 6.29 (b) than at 14C in Figure 6.29 (a). The differences of  $D_t$  between points 14C and 14A in each month are greater than that of  $D_w$ . Specifically, Figure 6.29 (a) shows that, for point 14C, the  $D_t$  and  $D_w$  do not always show the same direction throughout the year; when neglecting the positive or negative direction, the value of  $D_t$  is greater than  $D_w$  for each month except April and October. For point 14A in Figure 6.29 (b), for most of the months, the value of  $D_w$  is slightly greater than that of  $D_t$ . Regarding the quantity and the phase position of  $D_t$ ,  $D_w$  and  $D_{t+w}$ , it can be concluded that the dominating item also dominates the phase position of displacement  $D_{t+w}$ .



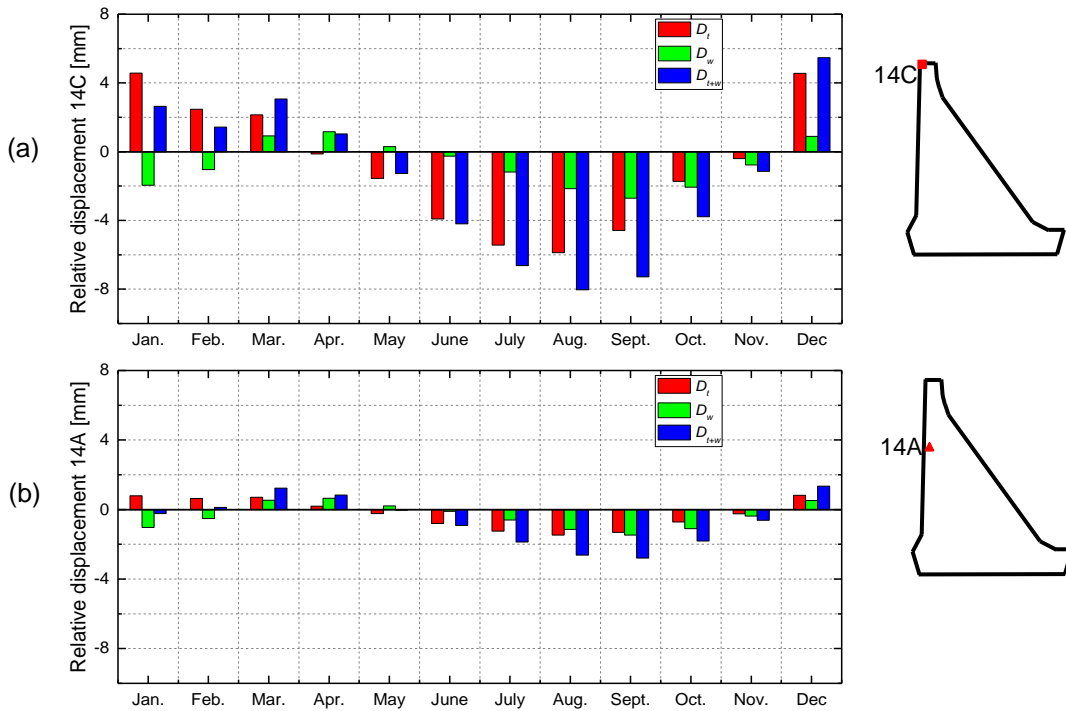


Figure 6.29: The proportion of  $D_t$ ,  $D_w$  at locations 14C and 14A in 2009

### 6.3.3 An example of unusual load case

Based on the ANM, it is possible to acquire simulation results under different combinations of unusual situations. In terms of displacements under single variable, it is obtained from Sections 6.1 and 6.2 that the dam deforms towards downstream with the increase of water level and deforms towards upstream with the increase of temperature. The critical load condition thus regards the combination of high water-level and low temperature as well as low water level and high temperature.

As an application example, Figure 6.30 illustrates an unusual load case for a 365-day period, and an unusual environmental condition with critical load combination is adopted to investigate the response. Regarding the temperature, unusual ambient temperature conditions with air temperature of “1.5 at” in the aforesaid unusual temperature scenario I are adopted. Because the temperature is lower in winter and relatively higher in summer, unusual water level situations are assumed for each time period, i.e., full storage of water is assumed in winter and the opposite, an empty reservoir, is assumed in summer. A stepped water level between summer and winter is assumed rather than ramped water level variation, i.e., the water level varies only in two water levels in this example: the full storage of 423.6 m a.s.l. during cold seasons and an empty reservoir during warm seasons. For the full storage period, the upstream face is specified with water temperatures of different layers; while the air temperature instead of water temperature is specified on the upstream face as boundary temperature conditions for the empty reservoir in summer. As for the switch time point of the unusual load,

it should be mentioned that, it is defined that from the end of April to the end of October as the warm seasons.

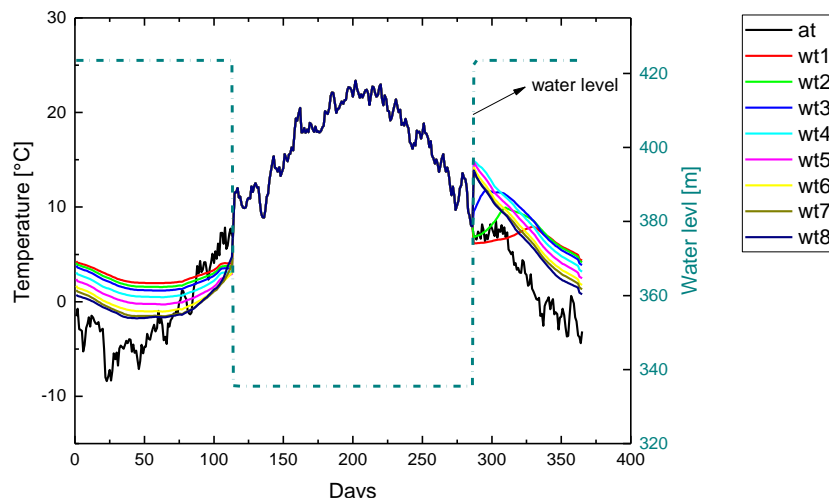


Figure 6.30: An unusual load case considering the critical loading conditions

Figure 6.31 depicts the response of relative displacements in the upstream-downstream direction at the representative location 14C under unusual load conditions described in Figure 6.30. The assumption that the changes in water level from full storage to empty reservoir, and the step increase of temperature on the upstream face accounts for the majority of the dramatic decrease of  $\Delta D_1$  and increase of  $\Delta D_2$  in Figure 6.31. The displacements at 14C vary between 11.3 mm in winter and -10.4 mm in summer. This variation range of 21.7 mm is about 1.5 times the recorded variation range of 14.8 mm (shown in Figure 3.20).

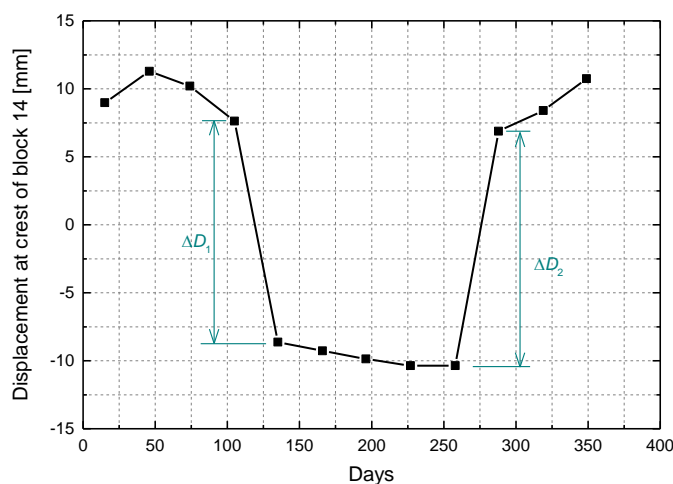


Figure 6.31: Displacement at 14C in upstream-downstream under unusual temperature and water level assumption

When the variation range of displacements increases to 1.5 times the recorded range, it is not possible to evaluate the health state of the dam or tell possible failure or damage in the dam using the displacement results due to the linear elastic material assumption. To investigate the

performance state of the dam under this unusual load case, the tensile stresses are presented to investigate whether the dam exceeds the tensile strength or not. The results of tensile stress distributions of the dam subjected to thermal distribution within the dam body, hydrostatic pressure, self-weight and uplift pressure are shown in Figure 6.32, Figure 6.33 and Figure 6.34 at midmonth in a one-year period. The determination of tensile strength of the concrete of Rappbode Dam is presented in Appendix F. In all the figures, the regions with tensile stress exceeding tensile strength are indicated in red. Due to the linear stress analysis, it is not possible to exactly determine the cracks' profile in these regions, but the probable crack regions could be predicted when the tensile stress exceeds the tensile strength.

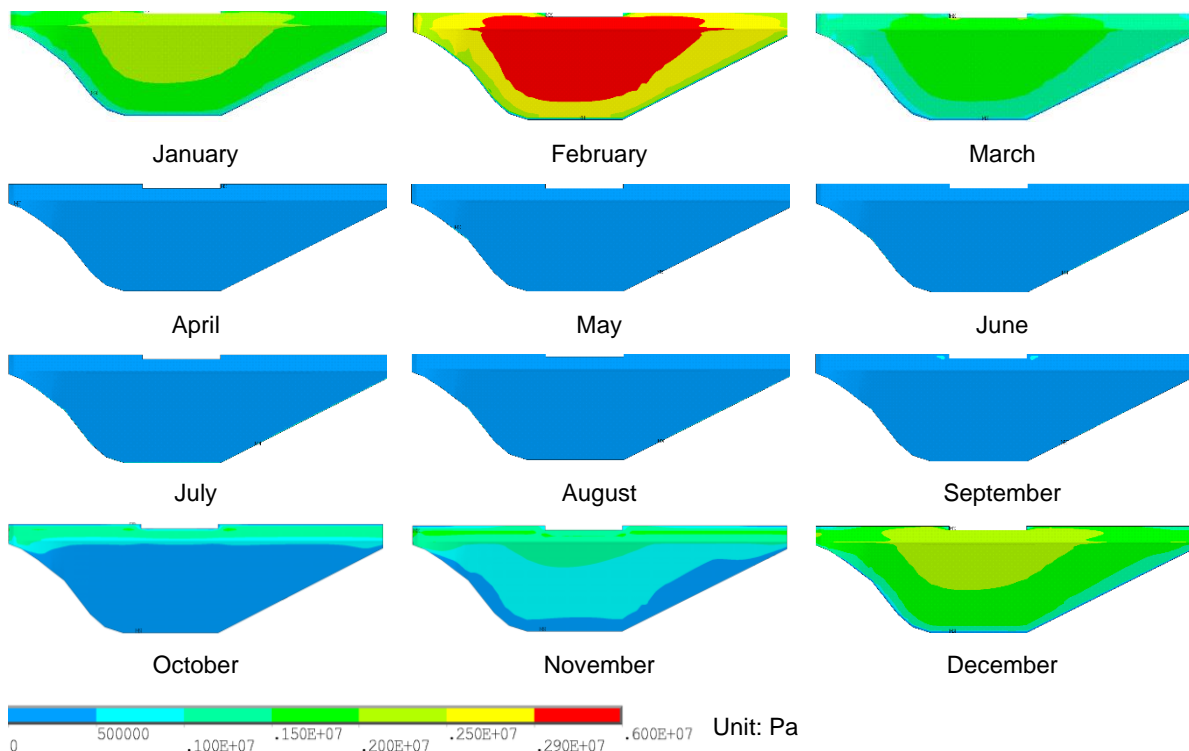


Figure 6.32: Tensile stress distribution subjected to thermal distribution, hydrostatic pressure, self-weight and uplift pressure at downstream face at midmonth

Figure 6.32 and Figure 6.33 show the tensile stress distribution for the downstream and upstream face of the dam. The red colour indicates that the tensile stress exceeds the tensile strength of 2.9 MPa (seen in Appendix F) for the face concrete. It is noticed that under this assumed unusual load case, the red colour exists in the cold month of the year in February at regions on the downstream face, where probable cracks occur at this red region. Due to the cold weather from October to March, the tensile stresses are more noticeable for both the upstream and downstream faces; while for the relative warm months from April to September, the tensile stresses on the face of the dam are negligible.

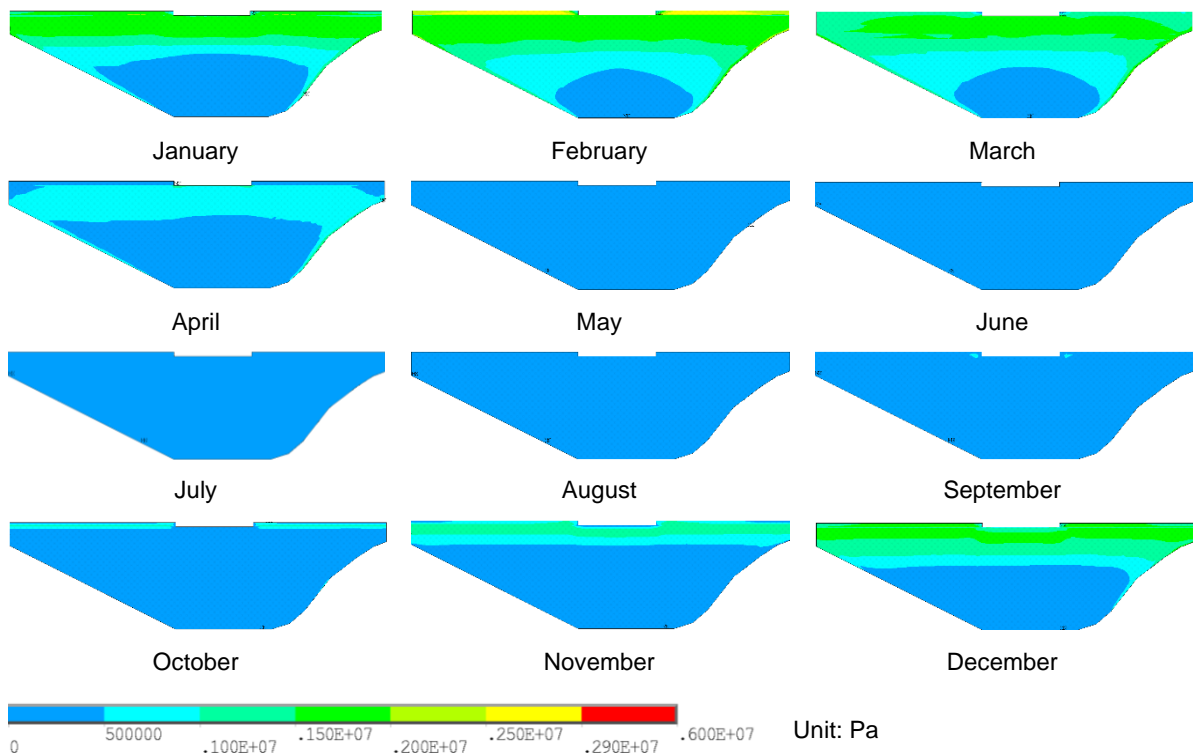


Figure 6.33: Tensile stress distribution due to thermal distribution, hydrostatic pressure, self-weight and uplift pressure at upstream face at midmonth

Figure 6.34 shows the tensile stresses at cross section of central block 14. The red region presents the region with tensile stress exceeding 1.2 MPa (tensile strength for the core concrete is shown in Appendix F). Figure 6.34 shows that this red region exists in January, February and December at the face concrete, but the tensile strength for face concrete is 2.9 MPa rather than 1.2 MPa. In the core region of the crown adjacent to the top face of the dam, the tensile stress exceeds 1.2 MPa in March and April, and thus probable cracks could occur in this region. Despite the relative greater tensile stresses for the inner upper concrete from May to September, the values here are still under 1.2 MPa.

This example of unusual load case presents an environmental condition of unusually cold wintertime and warm summertime and a switch from unusual high-water level to unusual low-water level during a one-year period. The displacements at the crown of the central block present a variation range 1.5 times greater than the range under usual loading conditions. The tensile stresses investigated on the upstream and downstream faces as well as in the cross-section of the dam provide the visualisation of where the tensile stress exceeds the tensile strength of the concrete. The simulation of unusual load cases based on the ANM provides reference values of displacements in the interpretation of monitored data and predicts the health state of the dam under previous not experienced unusual load cases.

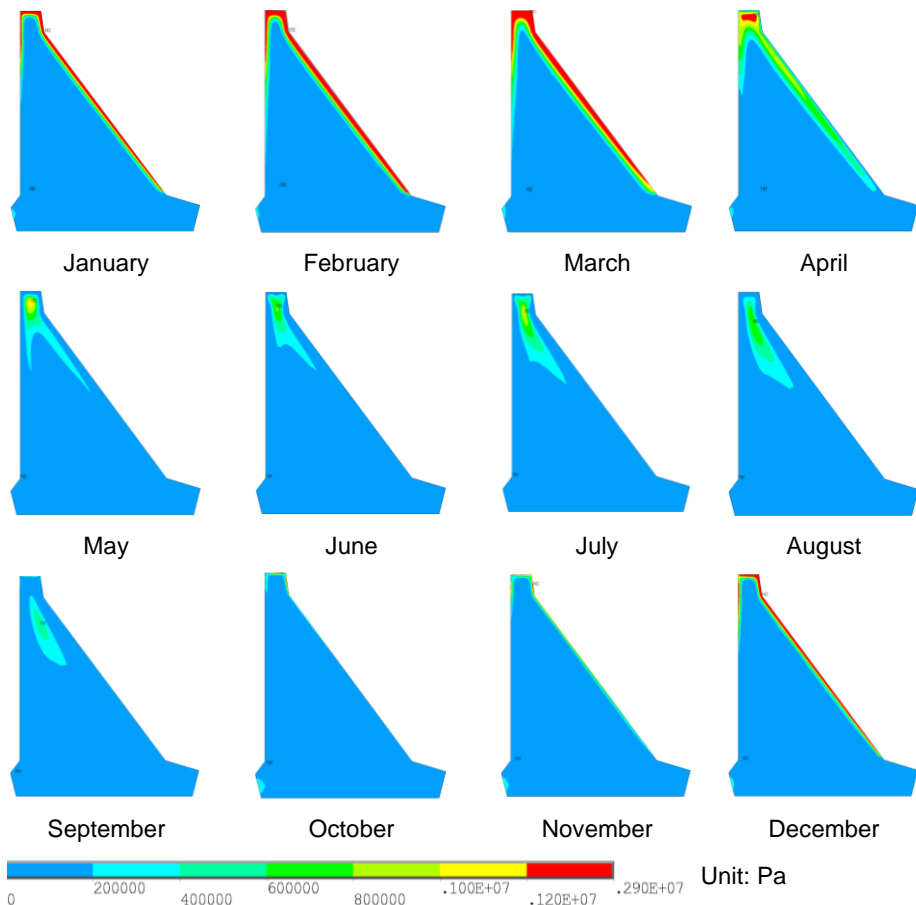


Figure 6.34: Tensile stress distribution due to thermal distribution, hydrostatic pressure, self-weight and uplift pressure for transverse section corresponding to central block at midmonth

## 6.4 Conclusions

Based on the ANM, thermal displacements due to variations in ambient temperature were investigated and showed that the dam deforms towards upstream with the increase of temperature. Despite the phase shift between temperatures at different elevations in a single block, no phase shift between the thermal response of displacements is detected at different elevations.

Structural displacements due to variation of water level were investigated by considering usual and unusual variations in water level, which showed that the dam deforms towards downstream with the increase of water level. The uplift pressure at the dam base has a minor influence on the deformation behaviour when compared with the hydrostatic pressure at upstream face of the dam. The foundation needs to be taken into consideration together with the dam body when investigating the water-level-induced deformation behaviour of the dam.

In the simultaneous simulation of water level and ambient temperature, the computed simultaneous displacements were compared with the measured displacements under current usual loading conditions, therewith the reliability of the ANM is demonstrated. An information

gap of ten days in the recorded load of ambient temperature induces inaccuracy in the computed displacement results. Significant improvement is achieved when modifying the input of air temperatures according to the recorded data during the same period of previous years. Based on correlation analysis between thermal displacements or structural displacements and simultaneous displacements, the following conclusions can be drawn: the proportion of thermal displacements is larger than that of structural displacements induced from water levels at the dam crown; for the locations at suspension A with an elevation of 390 m a.s.l., the structural displacements induced from water level are decisive. The influence of thermal displacement diminishes with the decrease of elevation. With the ANM, reference values of deformation behaviour can be obtained under any combination of thermal distribution, hydrostatic pressure and uplift pressure, and comparison of concrete's tensile stress with its tensile strength can provide insight into the health state of the dam under the assumed load case.

## 7. Conclusions and recommendations

### 7.1 Conclusions

In this thesis, investigations of the deformation behaviour of a concrete dam were described under ambient environmental conditions based on monitoring data and numerical simulation. As a case study, an ANM of Rappbode Dam was developed to model the relationships between external loads (including hydrostatic pressure, uplift pressure, ambient air temperature and water side temperature) and deformation responses by calibrating a transient heat flow model and performing back analyses of material parameters in thermal-structural coupled analysis.

Graphical visualisations of the monitoring data at dam site were presented to acquire time-varying characteristics and regular variation ranges for each monitored item. The recorded water level, air temperature, water side temperature and uplift pressure constitute the time-varying ambient loading conditions of the dam. The recorded concrete temperatures from the thermometers roughly describe the seasonal temperature distribution in the dam; and displacements recorded by the pendulum indicate the time-dependent displacements' distribution in the dam. The recorded ambient loading conditions were specified on the developed numerical model to investigate the responses. The responses of concrete temperatures and displacements from the monitoring data represent the criteria for calibrating parameters to numerically simulate the temperature distribution and deformation behaviour of the dam.

A functional FE model with appropriate mesh was generated for the dam while simultaneously considering the computing accuracy and cost. For the body of the dam, an equivalent homogenous concrete structure was adopted, and linear elastic property was assumed, and thus the material parameters of the concrete are presented as effective values. The material parameters for the foundation were specified using values from laboratory tests.

A transient heat flow model was developed to simulate the time-varying thermal distribution in the dam. By investigating the influence of different initial temperature conditions via transient thermal analyses, a rational initial temperature distribution state was obtained for the simulation of time-varying temperatures in the dam. Alignment between the computed and measured temperature distributions was achieved by adjusting the thermal conductivity and boundary specifications. The phase shifts at different locations presented by the variation of temperature in the dam can be fully considered using this calibrated transient heat flow model.

In the back analyses of parameters for the simulation of displacements due to temperature distribution and water level, the effective values of the parameters were updated to present the current deformation behaviour of the dam in operational phase. Based on the achieved effective material parameters combined with the functional FE and transient heat flow models, a physically well-founded ANM was developed to investigate the dam deformation behaviour in its current operational state.

To comprehend the current deformation behaviour of the dam, simulations of displacements were conducted based on the developed ANM. First, the individual effects of water level and ambient temperature were investigated under usual as well as unusual loading conditions. The time- and location-varying (referring to locations at different elevations and different blocks) responses were investigated to describe the displacement variation and distribution in the dam. Then, simultaneous simulations of varied water level and varied temperature were performed to present simultaneous displacements. Comparisons between computed displacements using the ANM and measured displacements under recorded usual loading conditions show good alignments. Correlation coefficient was adopted to evaluate the weightiness of single effects on the total effect. Subsequently simulation of an unusual loading condition was presented as an example to provide reference values of the responses of displacement and the health state of the dam using the developed ANM, and warnings concerning areas with probable cracks were given when the tensile stress exceeded the tensile strength.

## 7.2 Recommendations

As the focus of this investigation was the interpretation of the deformation behaviour of a concrete dam based on monitoring data and numerical simulation, the numerical model developed in this work was based on some theoretic assumptions of material properties and geometrical simplification. The following section describes questions which arose as well as recommendations for improving the interpretation of concrete dams' deformation behaviour:

Due to the uncertainties in the impounding process, the irreversible displacement of the dam occurring at the beginning of the operating phase is not possible to simulate using this numerical model. Furthermore, when computing the displacements, uncertainties exist due to wind pressure, snow load, seepage, crevice water pressure etc., which require detailed examination. The dynamic impact of urgent water flow on the upstream surface is not yet considered in the static deformation analysis of the dam. The deformation behaviour due to the dynamic impact from vehicles and pedestrians can be considered to perform more precise modelling in future research.

Shrinkage and creep behaviour of the concrete in the long term are not considered in the modelling process; however, they may influence the deformation behaviour of the dam, which



---

could provide a topic of interest for future research. Non-linear behaviour of the dam structure could be necessary to investigate the exact profile of the probable cracks.

## 8. Literature

- ACI 318. (2007). *Building Code Requirements for Structural Concrete*. Farmington Hills, USA: American Concrete Institute.
- Andersson, J., & Hagberg, L. (2018). *Stability Analysis of High Concrete Dams - Longtan dam - a case study*. Luleå University of Technology.
- ANSYS. (2004). *Modeling and meshing guide*. Canonsburg, USA: ANSYS Inc.
- ANSYS. (2005). *Coupled-field analysis guide*. Canonsburg, USA: ANSYS, Inc. and ANSYS Europe, Ltd.
- ANSYS. (2009). *Thermal analysis guide*. Canonsburg, USA: ANSYS Inc.
- ANSYS. (2013). *Mechanical APDL basic analysis guide*. Canonsburg, USA: ANSYS Inc.
- Benzley, S. E., Perry, E., Merkley, K., Clark, B., & Sjaardema, G. (1995). A Comparison of All-Hexahedral and All-Tetrahedral Finite Element Meshes for Elastic and Elasto-Plastic Analysis. *4th International Meshing Roundtable, Sandia National Laboratories*, 179–191. <https://doi.org/10.1.1.70.392>
- Bettzieche, V. (1998). Berücksichtigung von Durchsickerung und Wärmefluß beim Nachweis der Standsicherheit alter Staumauern mit der Finite-Element-Methode. In P. Wriggers (Ed.), *Finite Elemente in der Baupraxis, FEM 98*. Berlin: Ernst & Sohn.
- Bianchi, M., & Bremmen, R. (2014). Health monitoring of arch dams - recent developments. *Restoration of Buildings and Monuments*, 7(3–4), 271–284. <https://doi.org/10.1515/rbm-2001-5572>
- Boberg, B., & Holm, D. (2012). *Fem Modeling of Concrete Gravity Dams*. Master thesis. Land and Water Resources Engineering, Royal Institute of Technology (KTH).
- Brincker, R., Andersen, P., & Jacobsen, N. J. (2007). Automated frequency domain decomposition for operational modal analysis. *Conference Proceedings of the Society for Experimental Mechanics Series*. Orlando.
- Bukenya, P., Moyo, P., Beushausen, H., & Oosthuizen, C. (2014). Health monitoring of concrete dams: A literature review. *Journal of Civil Structural Health Monitoring*, 4(4), 235–244. <https://doi.org/10.1007/s13349-014-0079-2>
- Bukenya, P., Moyo, P., & Oosthuizen, C. (2012). Modal parameter estimation from ambient vibration measurements of a dam using stochastic subspace identification methods. *Proceedings of the 3rd International Conference on Concrete Repair, Rehabilitation and Retrofitting*, 653–657. Cape town, South Africa.

- Cantieni, R., Pietrzko, S., & Deger, Y. (1998). Modal investigation of an office building floor. *Proceedings of the International Modal Analysis Conference - IMAC*, 1172–1178.
- Chopra, A. K., & Chakrabarti, P. (1972). The earthquake experience at koyna dam and stresses in concrete gravity dams. *Earthquake Engineering & Structural Dynamics*, 1(2), 151–164. <https://doi.org/10.1002/eqe.4290010204>
- Chouinard, L., Larivière, R., Côté, P., & Zhao, W. (2006). Analysis of irreversible displacements in multiple arch concrete dam using principal component analysis. *Joint International Conference on Computing and Decision Making in Civil and Building Engineering, Montréal*, 2211, 208–217.
- Cifuentes, A. O., & Kalbag, A. (1992). A performance study of tetrahedral and hexahedral elements in 3-D finite element structural analysis. *Finite Elements in Analysis and Design*, 12(3–4), 313–318. [https://doi.org/10.1016/0168-874X\(92\)90040-J](https://doi.org/10.1016/0168-874X(92)90040-J)
- Cleveland, C. J., & Morris, C. (2014). *Handbook of Energy, Volume II: Chronologies, Top Ten Lists, and Word Clouds* (First Edit). Elsevier Science.
- Colombo, M., Domaneschi, M., & Ghisi, A. (2016). Existing concrete dams: loads definition and finite element models validation. *Structural Monitoring and Maintenance*, 3(2), 129–144. <https://doi.org/http://dx.doi.org/10.12989/smm.2016.3.2.129>
- DAfStb. (2010). *DAfStb-Richtlinie Massige Bauteile aus Beton*. Berlin: Deutscher Ausschuss für Stahlbeton e. V.-DAfStb.
- Daoud, M., Galanis, N., & Ballivy, G. (1997). Calculation of the periodic temperature field in a concrete dam. *Canadian Journal of Civil Engineering*, 24(5), 772–784. <https://doi.org/10.1139/I97-020>
- De Sortis, A., & Paoliani, P. (2007). Statistical analysis and structural identification in concrete dam monitoring. *Engineering Structures*, 29(1), 110–120. <https://doi.org/10.1016/j.engstruct.2006.04.022>
- Demirkaya, S., & Balcilar, M. (2012). The Contribution of Soft Computing Techniques for the Interpretation of Dam Deformation. *FIG Working Week 2012 - Knowing to Manage the Territory, Protect the Environment, Evaluate the Cultural Heritage*. Rome, Italy.
- Dibiagio, E. (2000). Monitoring of Dams and Their Foundations. *20th International Commission on Large Dams*, Q. 78,(General Report).
- DIN 19700-11. (2004). *Stauanlagen – Teil 11: Talsperren*. Berlin: DIN Deutsches Institut für Normung e. V.
- DIN EN 1992. (2010). *Eurocode 2: Bemessung und Konstruktion von Stahlbeton- und Spannbetontragwerken – Teil 1-1: Allgemeine Bemessungsregeln und Regeln für den*

- Hochbau; Deutsche Fassung EN 1992-1-1:2004 + AC:2010*. Berlin: DIN Deutsches Institut für Normung e.V .
- DIN EN 206. (2016). *Beton – Festlegung, Eigenschaften, Herstellung und Konformität; Deutsche Fassung EN 206:2013+A1:2016*. Berlin: DIN Deutsches Institut für Normung e. V.
- Fahland, S. (2004). *Verformungsverhalten einer kombinierten Bogen-Gewichtsstaumauer unter Betriebsbedingungen*. Dissertation. Fakultät für Bergbau, Hüttenwesen und Maschinenwesen, Technischen Universität Clausthal.
- Golze, A. R. (1977). *Handbook of Dam Engineering* (First Edti). Van Nostrand Reinhold Co.
- Graham, W. (1999). *A Procedure for Estimating Loss of Life Caused by Dam Failure*. United States Department of Interior Bureau of Reclamation.
- Hintner, J. (2008). *Analyse der Fundamentverschiebungen infolge vertikaler und geneigter Belastung*. Dissertation. Fakultät für Bau- und Umweltingenieurwissenschaften, Universität Stuttgart.
- Holdren, C., & Nelson, S. M. (1998). Water Supply and Water Quality in Totten Reservoir, Montezuma County, Colorado. Retrieved January 2, 2020, from Technical Service Center Environmental Applications and Research Group website: [https://web.archive.org/web/20150906184833/http://www.usbr.gov/tsc/eco\\_research/9809.html](https://web.archive.org/web/20150906184833/http://www.usbr.gov/tsc/eco_research/9809.html)
- Hoppe, S., & Ortuño, M. G. D. M. (2015). Integrating dam monitoring software. *Hydropower & Dams*, (3), 105–110.
- Huang, Z., & Wu, B. (2018). *Three Gorges Dam*. <https://doi.org/doi.org/10.1007/978-3-662-55302-2>
- ICOLD (International Commission on Large Dams). (2003). *Dam surveillance guide committee on dam surveillance -Bulletin 158*. International Commission on Large Dams.
- ICOLD (International Commission on Large Dams). (2008). *The physical properties of hardened conventional concrete in dams*. International Commission on Large Dams.
- ICOLD (International Commission on Large Dams). (2019). General Synthesis. Retrieved December 10, 2019, from International Commission on Large Dams website: [https://www.icold-cigb.org/article/GB/world\\_register/general\\_synthesis/general-synthesis](https://www.icold-cigb.org/article/GB/world_register/general_synthesis/general-synthesis)
- Kennard, M. F., Owens, C. C., & Reader, R. A. (1996). *Engineering Guide to the Safety of Concrete and Masonry Dams in the UK*. London, UK: Construction Industry Research & Information Association (CIRIA).

- Khosravi, S., & Heydari, M. mehdi. (2013). Modelling of concrete gravity dam including dam-water-foundation rock interaction. *World Applied Sciences Journal*, 22(4), 538–546. <https://doi.org/10.5829/idosi.wasj.2013.22.04.551>
- Léger, P., & Venturelli, J. (1993). Seasonal temperature and stress distributions in concrete gravity dams Part 1: Modelling. *Canadian Journal of Civil Engineering*, 20(6), 999–1017. <https://doi.org/10.1139/l93-131>
- Léger, P., Venturelli, J., & Bhattacharjee, S. S. (1993). Seasonal temperature and stress distributions in concrete gravity dams. Part 2: Behavior. *Canadian Journal of Civil Engineering*, 20(6), 1018–1029. <https://doi.org/10.1139/l93-132>
- Li, M. chao, Guo, X. yu, Shi, J., & Zhu, Z. biao. (2015). Seepage and stress analysis of anti-seepage structures constructed with different concrete materials in an RCC gravity dam. *Water Science and Engineering*, 8(4), 326–334. <https://doi.org/10.1016/j.wse.2015.10.001>
- Liu, J., Feng, X. T., & Ding, X. L. (2003). Stability assessment of the Three-Gorges Dam foundation, China, using physical and numerical modeling-Part II: Numerical modeling. *International Journal of Rock Mechanics and Mining Sciences*, 40(5), 633–652. [https://doi.org/10.1016/S1365-1609\(03\)00056-X](https://doi.org/10.1016/S1365-1609(03)00056-X)
- Liu, J., Feng, X. T., Ding, X. L., Zhang, J., & Yue, D. M. (2003). Stability assessment of the Three-Gorges Dam foundation, China, using physical and numerical modeling-Part I: Physical model tests. *International Journal of Rock Mechanics and Mining Sciences*, 40(5), 609–631. [https://doi.org/10.1016/S1365-1609\(03\)00055-8](https://doi.org/10.1016/S1365-1609(03)00055-8)
- Loh, C. H., Chen, C. H., & Hsu, T. Y. (2011). Application of advanced statistical methods for extracting long-term trends in static monitoring data from an arch dam. *Structural Health Monitoring*, 10(6), 587–601. <https://doi.org/10.1177/14759217110395807>
- Lombardi, G. (2004). Advanced Data Interpretation for Diagnosis of Concrete Dams. *Structural Safety Assessment of Dams*. Udine.
- Luino, F., & De Graff, J. V. (2012). The Stava mudflow of 19 July 1985 (Northern Italy): A disaster that effective regulation might have prevented. *Natural Hazards and Earth System Science*, 12(4), 1029–1044. <https://doi.org/10.5194/nhess-12-1029-2012>
- Maken, D. D., Léger, P., & Roth, S.-N. (2013). Seasonal Thermal Cracking of Concrete Dams in Northern Regions. *Journal of Performance of Constructed Facilities*, 28(4). [https://doi.org/10.1061/\(ASCE\)CF.1943-5509.0000483](https://doi.org/10.1061/(ASCE)CF.1943-5509.0000483)
- Mata, J., Tavares de Castro, A., & Sá da Costa, J. (2013). Time-frequency analysis for concrete dam safety control: Correlation between the daily variation of structural response

- and air temperature. *Engineering Structures*, 48, 658–665. <https://doi.org/10.1016/j.engstruct.2012.12.013>
- Mirzabozorg, H., Hariri-Ardebili, M. A., Heshmati, M., & Seyed-Kolbadi, S. M. (2014). Structural safety evaluation of Karun III Dam and calibration of its finite element model using instrumentation and site observation. *Case Studies in Structural Engineering*, 1(1), 6–12. <https://doi.org/10.1016/j.csse.2014.02.001>
- Murty, K. G. (2015). *Case Studies in Operations Research - Applications of Optimal Decision Making*. <https://doi.org/10.1007/978-1-4939-1007-6>
- Nedushan, B. A. (2002). *Multivariate statistical analysis of monitoring data for concrete dams*. Dissertation. Department of Civil Engineering and Applied Mechanics, McGill University.
- Ozisik, M. N. (1993). *Heat conduction* (2nd ed.). New York: John Wiley & Sons.
- Paschotta, R. (2017). Artikel "Wärmeleitfähigkeit" im RP-Energie-Lexikon. Retrieved from <https://www.energie-lexikon.info/waermeleitfaehigkeit.html>
- Perner, F., & Oberhuber, P. (2010). Analysis of arch dam deformations. *Frontiers of Architecture and Civil Engineering in China*, 4(1), 102–108. <https://doi.org/10.1007/s11709-010-0012-7>
- Popp, T. (2003). *Scherversuche an Bohrkernen aus dem Felsuntergrund der TS Rappbode*. Institut für Gebirgsmechanik GmbH.
- Qin, Y. (2008). *ANSYS Basic and example tutorial*. Beijing: Chemical industry press.
- Ratnayaka, D. D., Brandt, M. J., Johnson, K. M., Ratnayaka, D. D., Brandt, M. J., & Johnson, K. M. (2009). Dams, Reservoirs and River Intakes. *Water Supply*, 149–193. <https://doi.org/10.1016/B978-0-7506-6843-9.00013-5>
- Rich, T. P. (2014). Lessons in Social Responsibility from the Austin Dam Failure. *International Journal of Engineering Education*, 22(6), 1287–1296.
- Rißler, P. (1998). *Talsperren-praxis*. München: R. Oldenbourg Verlag GmbH.
- Ritter, A., & et.al. (2013). Performance evaluation of hydrological models: Statistical significance for reducing subjectivity in goodness-of-fit assessments. *Journal of Hydrology*, 480, 33–45. <https://doi.org/10.1016/j.jhydrol.2012.12.004>
- Rodgers, J. L., & Nicewander, W. A. (1988). Thirteen ways to look at the correlation coefficient. *American Statistician*, 42(1), 59–66. <https://doi.org/10.1080/00031305.1988.10475524>
- Roselend-Staudamm. (n.d.). Retrieved January 2, 2020, from <https://structurae.net/de/bauwerke/roselend-staudamm>
- Schmidt, M. (1992). *Talsperren im Harz (Ost- und Westharz)*. Clausthal-Zellerfeld:

- Papierflieger Verlag.
- Schneider. (2010). *Bautabellen für Ingenieure* (19th Editi). Bundesanzeiger.
- Sheibany, F., & Ghaemian, M. (2004). Thermal stress analysis of concrete arch dams due to enviromental action. *2004 ASME International Mechanical Engineering Congress and Exposition*, 375(1), 393–402. <https://doi.org/10.1115/IMECE2004-60242>
- Sheibany, F., & Ghaemian, M. (2006). Effects of environmental action on thermal stress analysis of Karaj concrete arch dam. *Journal of Engineering Mechanics*, 132(5), 532–544. [https://doi.org/10.1061/\(asce\)0733-9399\(2006\)132:5\(532\)](https://doi.org/10.1061/(asce)0733-9399(2006)132:5(532))
- Stansell, A. C. (2014). Memorialization and memory of southern California's St. Francis Dam disaster of 1928. *Pontificia Universidad Catolica Del Peru*, 8(33), 44.
- Stevens, E. (1988). *Hoover Dam: An American Adventure* (Revised). Denver art museum Verlag.
- Sun, P. M., Bao, T. F., Gu, C. S., Jiang, M., Wang, T., & Shi, Z. W. (2016). Parameter sensitivity and inversion analysis of a concrete faced rock-fill dam based on HS-BPNN algorithm. *Science China Technological Sciences*, 59(9), 1442–1451. <https://doi.org/10.1007/s11431-016-0213-y>
- Tatin, M., Briffaut, M., Dufour, F., Simon, A., & Fabre, J. P. (2015). Thermal displacements of concrete dams: Accounting for water temperature in statistical models. *Engineering Structures*, 91, 26–39. <https://doi.org/10.1016/j.engstruct.2015.01.047>
- Tyagunov, S., Grünthal, G., Wahlström, R., Stempniewski, L., & Zschau, J. (2006). Seismic risk mapping for Germany. *Natural Hazards and Earth System Sciences*, 6(4), 573–586. <https://doi.org/10.5194/nhess-6-573-2006>
- Varagilal, I. A. (2018). *Stability analysis of gravity dams for the maximum design earthquake*. 133.
- VEB Wasserwirtschaft Bode. (1953). *Entwurf der Sperrmauer Rappbode*. Blankenburg: Volkseigene Betrieb (VEB) Wasserwirtschaft Bode.
- Venturelli, J. (1992). *Seasonal temperature and stress distributions in concrete gravity dams*. Master thesis. Department of Civil Engineering and Applied Mechanics, McGill University.
- Verein Deutscher Zementwerke. (2002). *Zement Taschenbuch* (50 Auflage). Verlag Bau+Technik GmbH.
- Weterrückblick. (2007). Retrieved March 14, 2019, from <https://www.wetteronline.de/weterrueckblick/jahresr-uuml-ckblick-2007-2007-12-29-jh>
- Wieland, M. (2005). Tensile Stresses in Concrete Dams. *Water Power and Dam Construction*.

- Wouters, R. (2010). *Talsperren in Sachsen-Anhalt: Wasser für Mitteldeutschland*. Mitteldeutscher Verlag.
- Zhang, G., & Zhang, J. M. (2009). Numerical modeling of soil-structure interface of a concrete-faced rockfill dam. *Computers and Geotechnics*, 36(5), 762–772. <https://doi.org/10.1016/j.compgeo.2009.01.002>
- Zhang, L., Brincker, R., & Andersen, P. (2004). An overview of major developments and issues in modal identification. In *22nd IMAC Conference & Exposition 2004* (Vol. 4, pp. 2138–2145). Society for Experimental Mechanics (SEM).
- Zheng, D., Cheng, L., Bao, T., & Lv, B. (2013). Integrated parameter inversion analysis method of a CFRD based on multi-output support vector machines and the clonal selection algorithm. *Computers and Geotechnics*, 47(September), 68–77. <https://doi.org/10.1016/j.compgeo.2012.07.006>
- Zhou, W., Hua, J., Chang, X., & Zhou, C. (2011). Settlement analysis of the Shuibuya concrete-face rockfill dam. *Computers and Geotechnics*, 38(2), 269–280. <https://doi.org/10.1016/j.compgeo.2010.10.004>
- Zhu, B. (1997). Prediction of Water Temperature in Deep Reservoirs. *Dam Engineering*, 8(1), 13–25.
- Zhu, B. (2014). *Thermal stresses and temperature control of mass concrete* (First Edit). Elsevier Science.



### A. Additional ambient temperature at water side from monitoring data

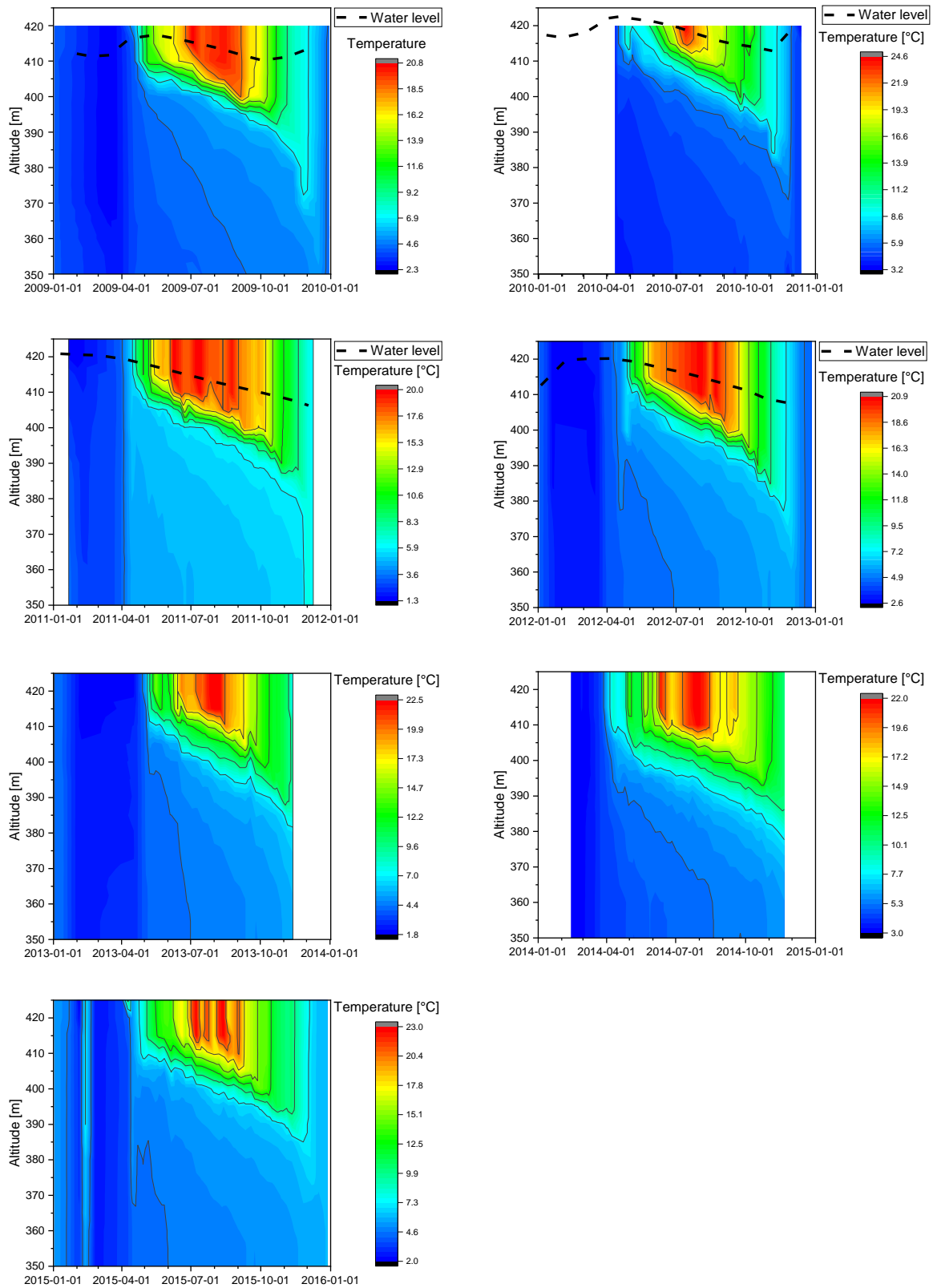


Figure A.1: Water temperature profile in reservoir in different years

## B. Approximation of air-concrete contact surface

According to the investigations from Zhu (2014), the kind of boundary condition describing the air-concrete contact surface in Equation (4.6) can be transformed into the following form:

$$-\frac{\partial T}{\partial n} = \frac{T_s - T_a}{\lambda/\beta} \quad (\text{B.1})$$

When the surface temperature  $T_s$  is changed from  $T_1$  to  $T_2$ , then the negative temperature gradient can be written as  $-\frac{\partial T_1}{\partial n} = \tan \varphi_1 = \frac{T_1 - T_a}{\lambda/\beta}$  and  $-\frac{\partial T_2}{\partial n} = \tan \varphi_2 = \frac{T_2 - T_a}{\lambda/\beta}$ .

As shown in Figure 2.3, the tangents to the temperature curves at the surface will always pass through point B and the distance between point B and the surface of concrete is

$$d = \lambda/\beta \quad (\text{B.2})$$

Where  $d$  is the virtual thickness,  $\lambda$  is the thermal conductivity for concrete and  $\beta$  is the surface conductance.

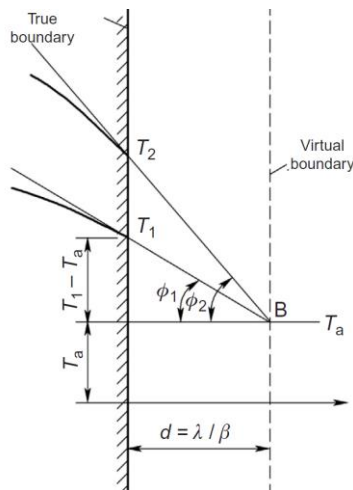


Figure B.1: The air-concrete contact surface (Zhu, 2014)

For this kind of boundary condition, if a virtual thickness  $d = \lambda/\beta$  is added to the true boundary, a virtual boundary is obtained. The temperature on the virtual boundary is equal to the air temperature  $T_a$ . It means that, the virtual boundary belongs to the first kind of boundary condition with prescribed temperature  $T_a$  shown in Equation (4.5).

For conventional concrete dam, the thermal conductivity  $\lambda$  can be in the range between 1.2 to 3.0 W/(m·K) (ICOLD, 2008), the surface conductance  $\beta$  for air-concrete contact surface can be estimated by the formula

$$\text{For rough surface} \quad \beta = 5.85 + 4.88 v_a^{0.910} \quad (\text{B.3})$$

$$\text{For smooth surface} \quad \beta = 5.13 + 4.82 v_a^{0.885} \quad (\text{B.4})$$

Where  $v_a$  is the speed of wind at the air-concrete contact surface.

For the air-concrete contact boundary, the  $\lambda/\beta = 0.1 \text{ m} \sim 0.2 \text{ m}$ . It means the virtual thickness of the air-concrete contact surface could be  $0.1 \text{ m} \sim 0.2 \text{ m}$ . Then in the following presents the influence of this virtual thickness on the relationship between surface temperature and air temperature.

For massive concrete, for the air-concrete contact boundary, firstly, the air temperature is approximately set to sinusoidal change:

$$T_a = A_m \sin\left(\frac{2\pi}{P} \tau\right) \quad (\text{B.5})$$

Where  $A_m$  is the amplitude of air temperature;  $P$  is the temperature change cycle.

Secondly, in order to check the relationship between surface temperature of concrete and air temperature, a semi-infinite one-dimensional body is assumed, the one-dimensional equation can be used to solve the heat problem (Zhu, 2014).

Heat transfer equation:

$$\left. \begin{aligned} a \frac{\partial^2 T}{\partial x^2} &= \frac{\partial T}{\partial \tau} \\ a &= \frac{\lambda}{c\rho} \end{aligned} \right\} \quad (\text{B.6})$$

Initial condition:

When  $\tau = 0$

$$T(x, 0) = 0 \quad (\text{B.7})$$

Boundary condition:

When  $x = 0, \tau > 0$

Then

$$-\lambda \frac{\partial T}{\partial x} = \beta \left( T - A_m \sin\left(\frac{2\pi}{P} \tau\right) \right) \quad (\text{B.8})$$

When  $x = \infty, \tau > 0$

Then

$$T = 0 \quad (\text{B.9})$$

Where  $\lambda$  is the thermal conductivity;  $c$  is the specific heat;  $\rho$  is density.

Solve the differential equations above, when  $\tau \rightarrow \infty$ , then the temperature inside the dam would be a quasi-stationary temperature field, the solution can be written as (Zhu, 2014):

$$T(x, \tau) = A_{m0} e^{-x\sqrt{\pi/aP}} \sin\left(\frac{2\pi}{P}\tau - \left(x\sqrt{\frac{\pi}{2P}} + M\right)\right) \quad (\text{B.10})$$

$$A_{m0} = A_m \left(1 + \frac{2\lambda}{\beta} \sqrt{\frac{\pi}{aP}} + \frac{2\pi\lambda^2}{aP\beta^2}\right)^{-1/2} \quad (\text{B.11})$$

$$M = \tan^{-1}\left(\frac{1}{1 + \sqrt{ap/\pi g\beta/\lambda}}\right) \quad (\text{B.12})$$

Where  $A_{m0}$  is the amplitude of temperature at concrete surface;  $A_m$  is the amplitude of air temperature;  $P$  is the cycle of air temperature changes;  $M$  is the phase delay of temperature at concrete surface compare to air temperature.

It can be drawn from the solution that: temperature inside the concrete changes cyclically with a cycle of  $P$ , which is the same as the temperature changes outside, but the maximal and minimum temperature values lag behind the outside temperature by  $x\sqrt{\pi/2P} + M$ .

Let  $a$  be  $0.10\text{m}^2/\text{d}$ , then the amplitude of temperature at concrete surface is calculated with equation (B.11) and Table B.1 depicts the results from taking virtual thickness in Equation (B.2) into account. It shows that, in the possible virtual thickness range, for the daily variation temperature,  $A_0$  is only about half of  $A$ , while for the annual variation of temperature,  $A_0$  is only 3% ~ 6% smaller than  $A$ .

Table B.1: The amplitude of temperature at concrete surface

$\frac{\lambda}{\beta}$	The amplitude of temperature at concrete surface $A_{m0}$	
	$P = 1$ day	$P = 365$ days
0.10 m	0.61A	0.97A
0.20 m	0.42A	0.94A

the temperature field which may be computed with the first kind of boundary condition.

Therefore, in calculating the temperature field under yearly periodic variations of temperature, the influence of virtual thickness is negligible that for the air-concrete contacted surface, it is assumed that temperature of the concrete equals to the air temperature, i.e. the air-concrete contact boundary can be computed as it is the first kind of boundary condition when the annually ambient air temperature are taken into consideration.

### C. Definition of elevation of the water temperature layers

Table C.1: The definition of water temperature layers

Name of layer	Corresponding height range of water temperature layer /m a.s.l.
wt1	336-385
wt2	385-390
wt3	390-395
wt4	395-400
wt5	400-405
wt6	405-410
wt7	410-415
wt8	415-425

#### D. Information about the locations in mesh density analysis

Table D.1: The perpendicular distance to dam surface of points for mesh density analysis under thermal load

Points	Perpendicular distance to the surface of the dam /m
1	2.7
2	11.7
3	20.2
4	4.4 (3.5m to the top)
5	4.4
6	4.4
7	4.4

## E. Information about elevations and blocks

Table E.1: The thickness of each elevation (Section 6.1)

Elevation (m a.s.l.)	name	Thickness (m)
339.5	a	64.9
354.5	b	53.8
369.5	c	42.7
384.6	d	31.6
399.5	e	20.4
414.5	f	10.6

Table E.2: The height of different blocks (Section 6.1)

Block Nr.	Mean height of the block (m)
8	69.5
11	90.0
14	103.5

## F. Tensile strength of concrete material for Rappbode Dam

For concrete dams, tensile stresses have been a major concern for a long time. With the help of FEM, it has become more accurate to obtain the stress values in dams than in the past. It is reported that tensile stresses cannot be avoided during strong earthquake ground shaking and also under unusual temperature variation (Wieland, 2005). High tensile stresses are undesirable because they cause cracks in concrete dams at locations with stress concentrations or along weak zone. Furthermore, compare to the compressive strength, the tensile strength is very small, usually less than 10% of the value of compressive strength.

Normally compression tests are carried out for the strength quality control, and then the tensile strength could be estimated based on empirical relations. Reasonable estimates of tensile strength as a function of compressive strength include:

Eurocode (DIN EN 1992, 2010):

$$f_{ctm} = 0.30 \cdot f_{ck}^{2/3} \leq C50/60 \quad (F.1)$$

$$f_{ctm} = 2.12 \cdot \ln\left(1 + \frac{f_{cm}}{10}\right) > C50/60 \quad (F.2)$$

$$f_{ck} = f_{cm} - 8 \quad (F.3)$$

Where  $f_{ctm}$  is the average value of tensile strength of concrete;

$f_{ck}$  is the Characteristic cylinder compressive strength of the concrete;

$f_{cm}$  is mean value of the cylinder compressive strength of the concrete.

The American Concrete Institute (ACI 318, 2007):

$$f_{ctm} = 0.67 \cdot \sqrt{f_{ck}} \quad (F.4)$$

The general linear empirical relation (Wieland, 2005):

$$f_{ctm} = 0.1 \cdot f_{ck} \quad (F.5)$$

For concretes with binders, it is advisable to store the specimens in water for a long period of time, especially at a selected verification age of 56 or 91 days for compressive strength (DAfStb, 2010). According to the design report (VEB Wasserwirtschaft Bode, 1953), the compressive strength of the core concrete and face concrete at the age of 90 days is on average 20.9 MPa and 37.4 Mpa respectively. Then as shown in Figure F.1, the tensile strength is estimated based on the aforesaid three different standards and the minimum value of the three is determined as tensile strength in this work to check the tensile stresses, i.e. 1.2 Mpa for the core concrete and 2.9 Mpa for the face concrete.



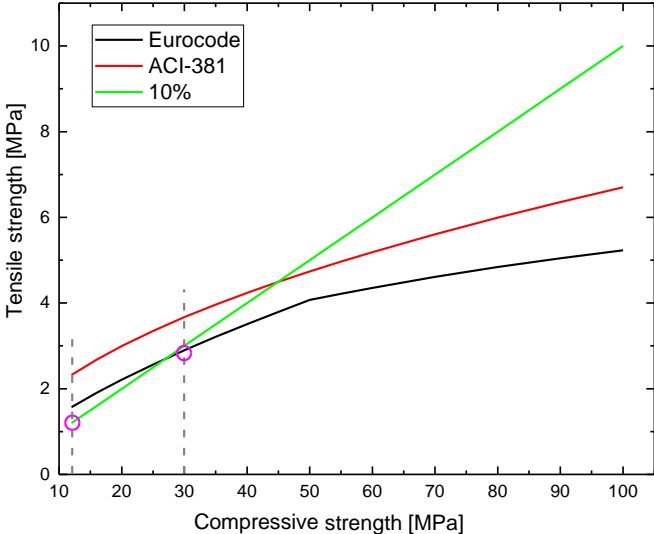


Figure F.1: Tensile strength estimation

## G. Additional information about comparisons between computed and measured displacements

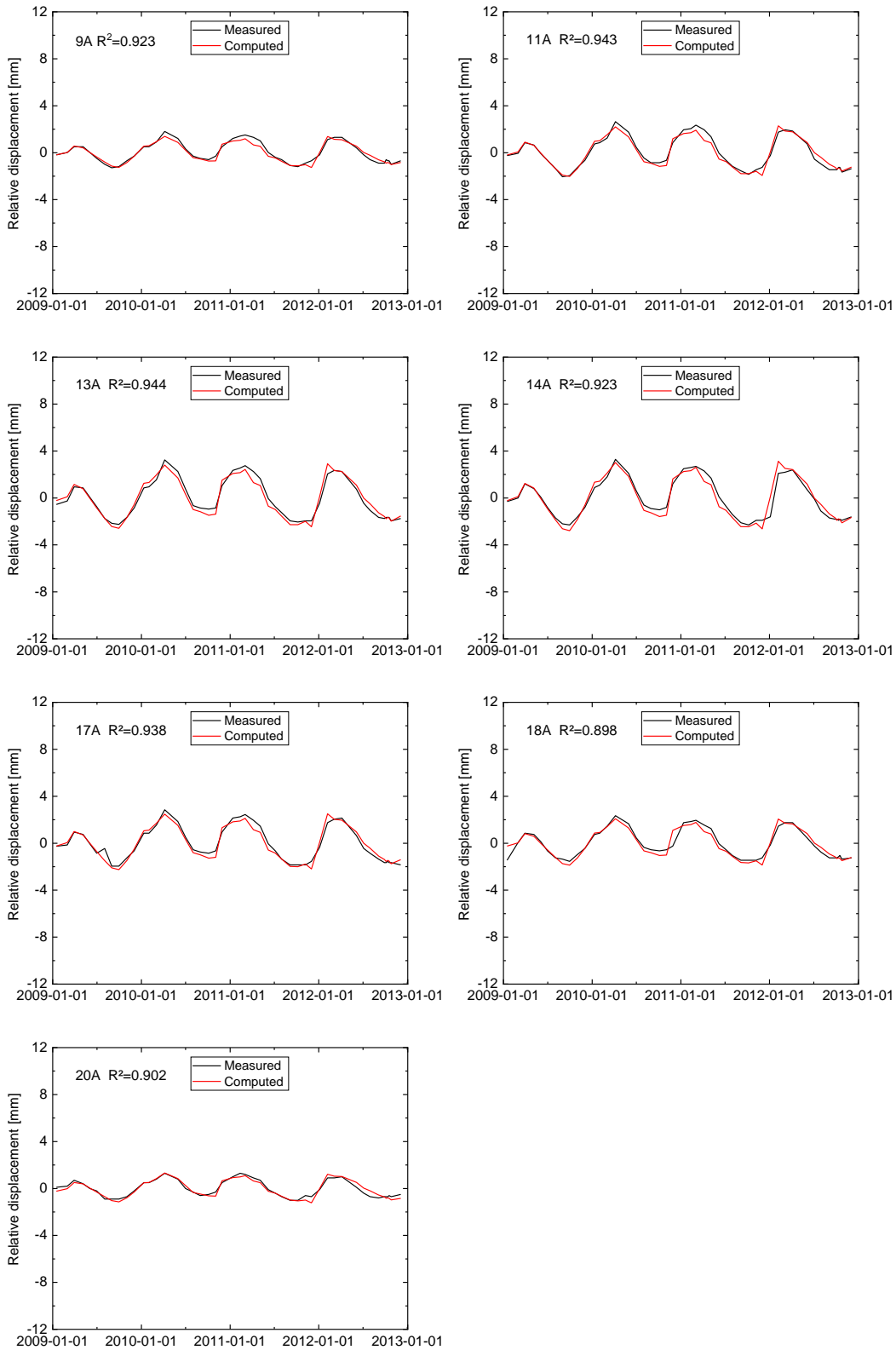
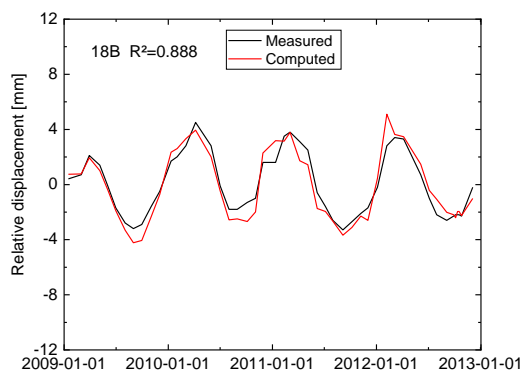
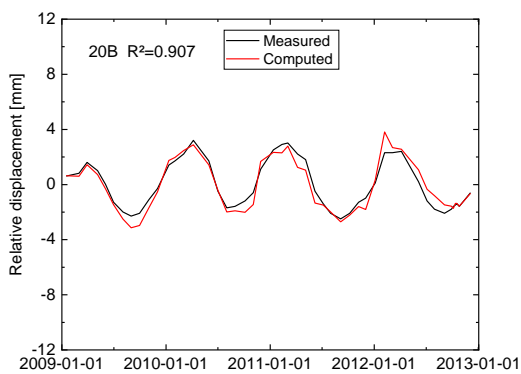
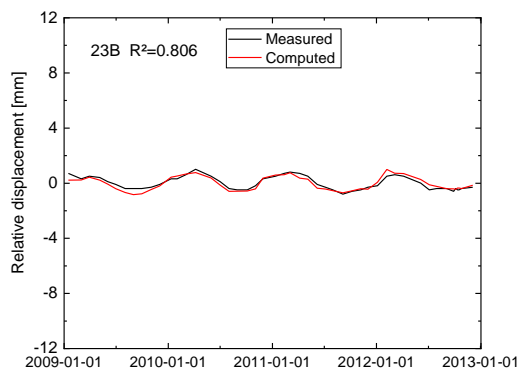
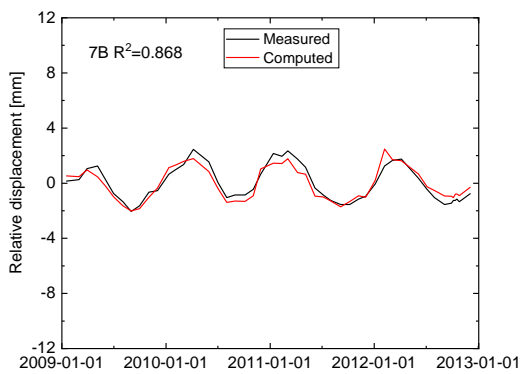
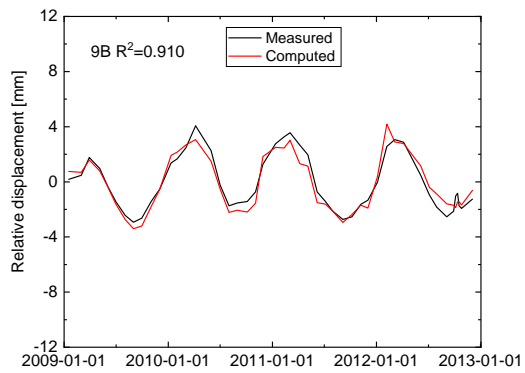
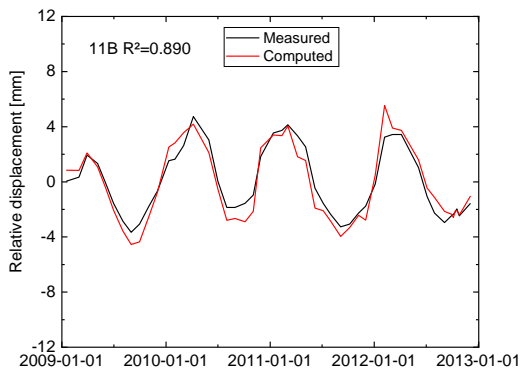
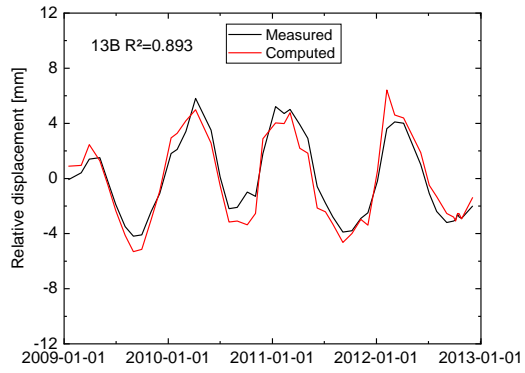
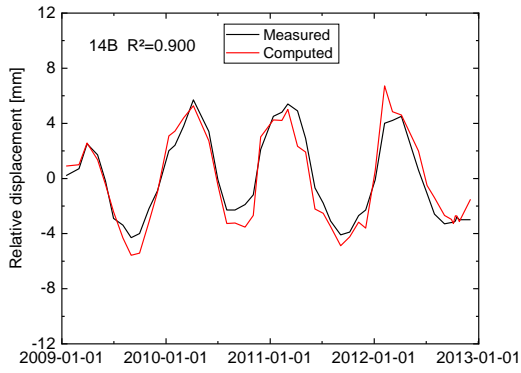


Figure G.1: Comparisons between computed and measured displacements in upstream-downstream direction at elevation A



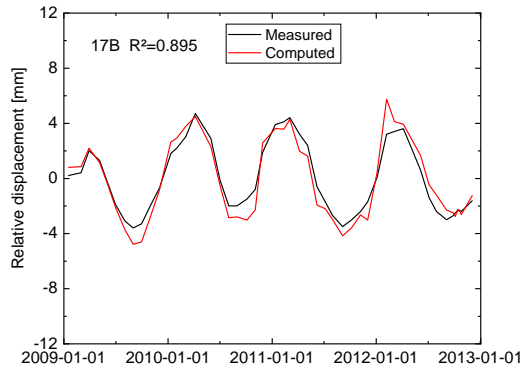


Figure G.2: Comparisons between computed and measured relative displacements in upstream-downstream direction at elevation B

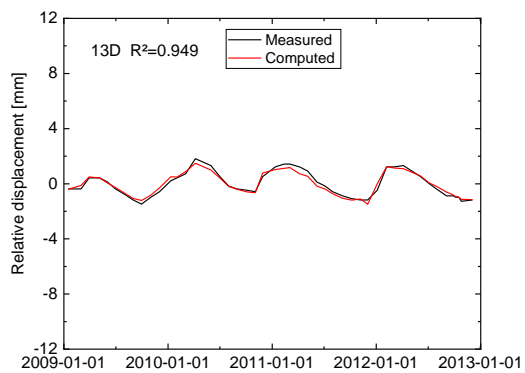


Figure G.3: Comparisons between computed and measured relative displacements in upstream-downstream direction at elevation D

## List of abbreviations and symbols

### Capital Latin letters

$A$	The suspension point of the Pendulums at elevation of 390.0 m a.s.l.
$A_m$	The amplitude of air temperature
$A_{m0}$	The amplitude of temperature at concrete surface
ANM	Advanced numerical model
$B$	The suspension point of the Pendulums at elevation of 408.5 m a.s.l.
$C$	The suspension point of the Pendulums at elevation of 426.4 m a.s.l.
$D_t$	Relative displacement induced from variation of temperature
$D_w$	Relative displacement induced from variation of water level
$D_{t+w}$	Relative displacement induced from variation of water level and temperature simultaneously
$E$	Elastic modulus
FEM	Finite element method
FE	Finite element
$G$	Gravity
LH	Linear hexahedral element
$N$	Number of measured values
No.	Number
$\bar{O}$	Mean value of measured values
$O_i$	Single measured value
$P$	Temperature change cycle
$P_i$	Single computed value
QT	Quadratic tetrahedral element
$R^2$	Determination of coefficient evaluating the goodness of fit between computed displacements and measured displacements
$T$	Temperature

$T_0$	Initial temperature
$T_a$	Ambient air temperature
$T_s$	Surface temperature

#### Lower case Latin letters

$t$	Air temperature specified on the air-concrete contact surface
$c$	Specific heat
$d$	Virtual thickness on the air-concrete contact surface
$f(\tau)$	A function of time to describe surface temperature
$f_{ck}$	The Characteristic cylinder compressive strength of the concrete
$f_{cm}$	Mean value of the cylinder compressive strength of the concrete
$f_{ctm}$	The average value of tensile strength of concrete
$g$	Acceleration of gravity
$h$	Water level in the reservoir
$k$	Diffusivity of the medium
$l$	Number of measurements or predicted values
m a.s.l.	Meters above sea level
$n$	The outward normal of the surface
$\rho$	Hydrostatic pressure
$r$	Pearson correlation coefficient
$r_t$	Pearson correlation coefficient of $D_t$ And $D_{t+w}$
$r_w$	Pearson correlation coefficient of $D_w$ And $D_{t+w}$
$v_a$	Speed of wind at air-concrete contact surface
wt	Water temperature specified on the water-concrete contact boundary
$x_i, y_i$	Individual sample points indexed with $i$ in the correlation coefficient calculation
$\bar{x}, \bar{y}$	Mean value of all the sample points
$l$	Number of pairs in the sample

## Lower case Greek letters

$\alpha$	The thermal expansion coefficient
$\beta$	Surface conductance
$\lambda$	Thermal conductivity
$\gamma_w$	Specific weight of water
$\eta$	Reduction factor for the uplift pressure at the base of dam heel
$\tau$	Variable presents time
$\rho$	Density of water

## List of Figures

Figure 2.1: Diagram of the classification of dams .....	6
Figure 2.2: Examples of dams of different types .....	7
Figure 3.1: Location of Rappbode Dam (Wouters, 2010).....	17
Figure 3.2: An overview of Rappbode Dam (Photo by Regional Association Harzer Urania e.V.) .....	17
Figure 3.3: The isometry of the dam with No. of the blocks and the inspection way system (Wouters, 2010).....	19
Figure 3.4: Upstream view of installed pendulums and floating pendulum locations .....	20
Figure 3.5: Cross section view of embodied thermometers locations for T0-T20 in block 18 21	
Figure 3.6: Top view of measuring points for uplift pressure at base of the dam.....	22
Figure 3.7: Time series (left) and boxplot (right) of water level in the reservoir .....	23
Figure 3.8: Uplift pressure profile under three different blocks on two different dates .....	24
Figure 3.9: Schematic of uplift pressure at the dam base with and without a drainage system (Rißler, 1998) .....	25
Figure 3.10: Comparison of water level and uplift pressure .....	26
Figure 3.11: Time series and box plot of ambient air temperature at the dam crown .....	27
Figure 3.12: Ambient temperature distribution at water side and water level on identical date .....	28
Figure 3.13: Ambient temperature profile at water side and water level in 2012 .....	29
Figure 3.14: Time series of ambient temperature values for lower part of upstream face .....	30
Figure 3.15: Time series of ambient temperature values for upper part of upstream face.....	30
Figure 3.16: Time series of temperatures at T0-T20.....	31
Figure 3.17: Time series of air temperature, T0 and water temperature at height of 420 m ..	32
Figure 3.18: Ranges of the recorded temperature values for T0-T20.....	33
Figure 3.19: Time series of temperature at T0, T3, T6, T9 and T12.....	34
Figure 3.20: Ranges of measured relative displacements to mean value in upstream-downstream direction .....	35
Figure 3.21: Visual view of relative displacements in upstream-downstream direction by time in 2005 .....	37
Figure 3.22: Time series of displacements in upstream-downstream direction at several comparable locations .....	38
Figure 3.23: Time series of relative displacement at bottom of block 13 from floating plumb wire in upstream-downstream direction .....	38
Figure 3.24: Ranges of measured relative displacements to mean value in longitudinal direction .....	40



Figure 3.25: Time series of relative displacements at blocks 9 and 20 in longitudinal direction .....	40
Figure 3.26: Comparison of air temperature, water level and relative displacement .....	41
Figure 4.1: Diagram of cross-section view of boundary temperature specification .....	50
Figure 4.2: The solid geometrical model of the dam-foundation system from downstream view.....	51
Figure 4.3: Upstream view of (a) applied hydrostatic pressure; (b) stress results from LH element; (c) stress results from QT element in upstream-downstream direction in ANSYS ..	55
Figure 4.4: Visualisation of the FE model of the dam with different element sizes .....	56
Figure 4.5: Number of nodes defined with different element sizes .....	56
Figure 4.6: Display of the locations of the points for mesh density analysis under hydrostatic pressures .....	57
Figure 4.7: Convergence results of hydrostatic pressure computation.....	57
Figure 4.8: Diagram of assumed boundary temperatures for mesh density analysis .....	58
Figure 4.9: View of the temperature distribution inside the dam at timepoint of 10 <sup>th</sup> day .....	58
Figure 4.10: Convergent curves of transient thermal analysis results .....	59
Figure 4.11: Display of the points for mesh accuracy analysis under thermal load .....	60
Figure 4.12: FE model of the dam (half of the dam).....	60
Figure 4.13: The FE model of dam-foundation system .....	61
Figure 5.1: The daily design temperature in a one-year period.....	63
Figure 5.2: The time series of temperature value at different locations in the dam.....	66
Figure 5.3: Cross section view for block 18 of the temperature distribution.....	68
Figure 5.4: Temperature values for elevations a, b and c in cross section of Block 18 .....	68
Figure 5.5: Comparison between calculated temperatures with different thermal conductivity values and measured data at T2 and T9 .....	69
Figure 5.6: Comparison between calculated temperatures with different thermal conductivity values and measured data at T0 .....	70
Figure 5.7: Comparison between calculated temperatures with different thermal conductivity values and measured data at T19 .....	71
Figure 5.8: Modified boundary temperature conditions .....	72
Figure 5.9: Comparison of computed values from two different calculations with measured values at T0.....	72
Figure 5.10: Comparison of computed values from two different calculations with measured values at T19.....	73
Figure 5.11: Comparison of computed values from two different calculations with measured values at T0.....	73
Figure 5.12: Comparisons of computed temperature and measured temperature at T0-T20	74

Figure 5.13: Comparison of time series of water level and air temperature.....	75
Figure 5.14: The calculating displacements with different $\alpha$ and measured displacements...	76
Figure 5.15: Comparison of water level induced displacements and reference values .....	78
Figure 6.1: Time series of temperatures and thermal displacements at 17C, 17B and 17A ..	81
Figure 6.2: Time series of mean temperature for crown zone and thermal displacement at 17C .....	82
Figure 6.3: Contours of thermal displacement in upstream-downstream direction in wintertime and summertime .....	83
Figure 6.4: Thermomechanical response in wintertime and summertime .....	84
Figure 6.5: Computed temperature for wintertime and summertime at different elevations of block 14.....	85
Figure 6.6: Computed thermal displacements of in wintertime and summertime at different elevations of block 14 .....	86
Figure 6.7: Tensile stresses in wintertime and summertime due to thermal load at different elevations of block 14.....	87
Figure 6.8: Thermal responses at elevation d in different blocks in summertime .....	88
Figure 6.9: Unusual air temperature scenarios I in a one-year period.....	89
Figure 6.10: Thermal displacement at 14C under unusual temperature I.....	90
Figure 6.11: Tensile stresses at the investigated point under unusual temperature scenario I .....	91
Figure 6.12: Air temperature for unusual temperature scenario II .....	92
Figure 6.13: Ambient temperature at water side for unusual temperature scenarios II.....	92
Figure 6.14: Thermal displacements at 14C under unusual temperature scenario II.....	93
Figure 6.15: Tensile stress at investigated point under unusual temperature scenario II .....	93
Figure 6.16: Time series of water level and relative structural displacement.....	94
Figure 6.17: Comparisons of water level induced displacements at different points of block 14 .....	95
Figure 6.18: Schematic drawing of deformation of the dam due to water load (air side view) .....	96
Figure 6.19: Water level induced displacements at crown of different blocks in 2010 .....	96
Figure 6.20: Displacements at 14C with unusual water level variation.....	97
Figure 6.21: Comparisons between computed and measured relative displacements in upstream-downstream direction at 14C, 14B and 14A.....	100
Figure 6.22: $R^2$ for points 14C, 14B and 14A.....	101
Figure 6.23: Comparisons between computed and measured relative displacements in upstream-downstream direction at dam crown .....	103
Figure 6.24: Goodness-of-fit evaluation of computed values .....	104

---

Figure 6.25: Time series of air temperature with assumed variations in the gap .....	105
Figure 6.26: Comparison of relative displacements with two different assumed temperatures in the gap .....	106
Figure 6.27: Values of correlation coefficient $r_t$ or $r_w$ .....	107
Figure 6.28: Comparisons of time series between $D_t$ , $D_w$ and $D_t + w$ .....	108
Figure 6.29: The proportion of $D_t$ , $D_w$ at locations 14C and 14A in 2009 .....	109
Figure 6.30: An unusual load case considering the critical loading conditions .....	110
Figure 6.31: Displacement at 14C in upstream-downstream under unusual temperature and water level assumption .....	110
Figure 6.32: Tensile stress distribution subjected to thermal distribution, hydrostatic pressure, self-weight and uplift pressure at downstream face at midmonth .....	111
Figure 6.33: Tensile stress distribution due to thermal distribution, hydrostatic pressure, self-weight and uplift pressure at upstream face at midmonth .....	112
Figure 6.34: Tensile stress distribution due to thermal distribution, hydrostatic pressure, self-weight and uplift pressure for transverse section corresponding to central block at midmonth .....	113
Figure A.1: Water temperature profile in reservoir in different years .....	125
Figure B.1: The air-concrete contact surface (Zhu, 2014) .....	126
Figure F.1: Tensile strength estimation .....	133
Figure G.1: Comparisons between computed and measured displacements in upstream-downstream direction at elevation A .....	134
Figure G.2: Comparisons between computed and measured relative displacements in upstream-downstream direction at elevation B .....	136
Figure G.3: Comparisons between computed and measured relative displacements in upstream-downstream direction at elevation D .....	136

## List of Tables

Table 2.1: Some typical dams and conducted numerical analysis .....	15
Table 3.1: Main characteristics of Rappbode dam (Wouters, 2010).....	18
Table 3.2: Locations of suspensions and console of pendulum in the Rappbode Dam.....	20
Table 3.3: The location of the floating pendulum .....	20
Table 3.4: Elevation of some blocks at the base.....	24
Table 3.5: Perpendicular distance to dam downstream face from T0, T3, T6, T9 and T12 ...	34
Table 4.1: Steps of a FE analysis in ANSYS .....	44
Table 4.2: System of units used in analysis.....	51
Table 4.3: Material parameters for the foundation of Rappbode Dam.....	52
Table 4.4: Material parameters of the concrete .....	53
Table 4.5: Starting values and interval values for the three critical parameters.....	53
Table 4.6: Characteristics of element SOLID185 and SOLID187.....	54
Table 5.1: The temperature field change inside the dam with different initial temperatures ..	64
Table 5.2: Effective values for the three critical parameters.....	78
Table 6.1: Criteria for goodness-of-fit evaluation .....	100
Table B.1: The amplitude of temperature at concrete surface.....	128
Table C.1: The definition of water temperature layers.....	129
Table D.1: The perpendicular distance to dam surface of points for mesh density analysis under thermal load .....	130
Table E.1: The thickness of each elevation (Section 6.1) .....	131
Table E.2: The height of different blocks (Section 6.1) .....	131